The role of macaque V1 neurons in spatiochromatic processing and behavior

Abhishek De

A dissertation

submitted in partial fulfillment of the

requirements for the degree for

Doctor of Philosophy

University of Washington

2020

Reading Committee:

Dr. Gregory D. Horwitz, Chair

Dr. Frederick M. Rieke

Dr. John C. Tuthill

Program Authorized to Offer Degree:

Neuroscience

University of Washington

ABSTRACT

Abhishek De

Chair of the Supervisory Committee:

Greg Horwitz

Department of Physiology and Biophysics

Vision is critical for survival. We can easily identify objects, guide actions, and avoid collisions if our eyes are open but these abilities are severely impaired if our eyes are closed. This tremendous feat of vision appears simplistic but is implemented by complex biological processes performed by the eye and brain. Therefore, a central goal in visual neuroscience is to understand how neurons in the brain represent scenes, and how the neural activity in turn helps guide behavior.

Scenes are composed of spatial and chromatic variations, herein referred to as spatiochromatic variations. In the primary visual cortex (V1) of macaque monkeys, some neurons jointly analyze edges and color, making them an ideal substrate for understanding human spatiochromatic vision. Double-opponent (DO) cells in V1 respond strongly to adjacently placed lights of opposite color and weakly to spatially uniform light of one color. These properties make them well suited for processing of color across space. However, we do not know precisely what information DO cells represent and how. Understanding how DO cells function will advance the field of visual neuroscience in three ways. First, it will help us understand how DO cells are connected to other neurons, thereby shedding light on the organization of cells in V1. Second, it

will help link the neuronal responses to behavioral phenomena in color vision. Third, it will advance mathematical models of visual processing that will guide research in other fields.

How information about scenes is used for behavior is incomplete without understanding the link between neural activity and behavior. A mechanistic understanding of how V1 neural activity impacts visual perception will be important for understanding the role of V1 in diseases and designing brain-machine interfaces.

Using a combination of electrophysiological measurements, monkey behavior and state-of-the-art techniques, I investigated the role of V1 DO cells in the spatiochromatic processing of light, and the role of V1 neural activity in visual perception. I compared my findings about DO cells to simple cells—the best understood functional cell type in V1 that represent oriented luminance edges in scenes, and integrate signals across space roughly linearly. I pursued my research in the form of three different projects, and I report the key findings from each of the projects below.

In project 1, I investigated the representation of edges by DO cells. I found that DO cells represent chromatic edges the same way as simple cells represent luminance edges. In project 2, I investigated how DO cells integrate color signals across space. I found that DO cells integrate spatial signals as linearly as simple cells meaning that both these classes of neurons simply weigh and sum the incoming light to generate a spiking response. In interpreting this result, it is important to realize that linearity is not the default mode of visual neurons but rather implies a specialized wiring. My results

suggest that the specialized wiring creates linear luminance edge detectors and chromatic edge detectors in V1. Together, the results from project 1 and project 2 suggest that DO cells are similar to simple cells in many ways, and these classes of neurons have a similar mechanism of processing edges than previously thought. This property has major implications in understanding the neural circuitry of these cell classes and their contributions to image processing, which I discuss in Chapters 2 & 3.

In project 3, I investigated the impact of silencing neural activity on behavior by pioneering a fast and powerful neural inactivation technique in monkey cortex. The advantage of this technique is that the neural inactivation can be reversed on a trial-by-trial basis, which was difficult to achieve previously. Inactivation of V1 led to reduced sensitivity for visual detection by monkeys suggesting that V1 neural activity impacts visual perception. This result opens doors for possible therapeutic treatments of visual impairments and investigations of many outstanding questions in the domain of perception, action and cognition, which I discuss in Chapter 4.

Collectively, my research has made important strides in the field of visual neuroscience by advancing our understanding of spatiochromatic processing by DO cells, and the impact of V1 neural activity on visual perception.

Dedicated to my family for their continual support:

“Dreams are not those that you see while sleeping,

But those that don’t let you sleep.”

TABLE OF CONTENTS

ACKNOWLEDGEMENTS

I would like to start this section by acknowledging all the unsung heroes of my PhD: the monkeys, the Neuroscience program administrative staff, PBIO office staff and the WaNPRC staff. Without their support and hard work, I would not be in a position to write this thesis.

I arrived in the "Land of Opportunity" on Feb 3rd, 2014. It was crystal clear at the end of my interview that it is at University of Washington that I want to pursue my PhD in Neuroscience. Two things that appealed to me were the systems neuroscience community, and the magical view of Mount Rainier floating above the mystical clouds.

Among all the interviewers, one person stood out. It was Greg Horwitz, whom I knew the least about and, who ultimately went onto become my PhD advisor. Over the last five years, I have been rigorously trained to be a critical thinker and a strong scientist and, Greg is the mastermind of that training. Greg has equipped me with numerous scientific skills—data interpretation and analysis, technical writing, public speaking, designing and performing experiments etc., all of which I am grateful for. Of those, the most I cherish is "accepting biology"—a key quality which I didn't value as much as I should have, when I started my PhD. I am grateful to Greg for teaching me his two core principles—urgency and importance, which have and will continue to be the pillars of my time management skills and efficiency. Above all, I am thankful to Greg for generosity with his time throughout my PhD.

I will always remember how influential Yasmine El-Shamayleh's contribution was to my growth as a scientist, and most importantly as an intellectual person. When I look back at myself, I realize how young, arrogant and dumb I was and, I would still be that person if Yasmine hadn't devoted time to show me the right path. Yasmine's mentorship skills are off the charts and I am grateful to be one of her many proteges. I look forward to advancing science with her one day.

I am grateful to my committee for guiding me through the scientific journey. I would like to thank Fred and John for being extremely participative in the committee meetings and providing excellent feedbacks. I am thankful to Adrienne for her support and funding at various stages of my career. I am thankful to Fred, John, Adrienne and Scott for teaching me to think about the big picture.

My years at UW would be insane without the emotional and scientific support of my cohort—Kali, Rachel, Jane, Jesse, Dean and Chris. I am thankful to them for accepting me and hearing all of my winnings. I am thankful to other members of the scientific community at UW—Dina Popovkina, J. Patrick Weller, Zack Lindbloom-Brown, Seth Konig, Ali Weber, Rich Pang, Max Turner, Yoni Browning, Clare Gamlin, Su-Yee Lee, Kameron Harris, Sufia Ahmed, Albert Ng, Bethany Kondiles, Sweta Agarwal, Tony Azevedo, Woon Joo, Gabriel Obregon-Henao, Shane Gibson, Lisa McConnell, Mike Jutras and Megan Jutras. I would like to extend a special thanks to Evanthia Nanou—a go-getter scientist, brimming with abundant energy to overcome any hurdle. There were times when I completely gave up on my projects and if Evanthia hadn't advised me, the projects would have never seen the light at the end of the tunnel.

I am blessed with an amazing set of friends outside my neuroscience community—Nihit, Ankit, Chandran, Amy, Emily, Harrison, Cathy, Alex, Saurabh, SRK, Rishabh, Debosmit, Jagori, Gourab. Of those, I am immensely thankful to Nihit, Jagori and Gourab for their unconditional support and love. They have been my family outside India.

I am immensely thankful for the love and support of my family—Ma, Baba, Ria, Mamu, Dida and Dadu. They have sacrificed a lot to make me reach where I am today. I love them very much, will always be present whenever they need me and keep fighting for them.

1. INTRODUCTION

The ability to sense, perceive and act on objects by humans is unparalleled by any existing machine. A natural question from a neurophysiological standpoint is that how is the brain able to achieve these goals. The luxury of vision as a modality and macaque as a model system has allowed experimenters to probe this question at a microscopic detail for decades. Vision serves as a premier modality for investigating this question because of 1) high spatial and temporal control of light by modern displays, 2) easy accessibility of visual system at a single neuron level and, 3) dependence of many behaviors on visual system. Macaques serve as a premier model for human action, perception and cognition because of their 1) trichromacy and, 2) vast similarity in brain anatomy, physiology and behavior with humans (DeValois, 1990).

Perception is a complex process that involves analysis of various aspects of scenes. Analysis of edges is one such aspect that is well suited to contribute to perception. Edges are either purely luminance or purely chromatic or a combination of both. The importance of edges to infer scenes is better understood psychophysically than neurophysiologically (Cavanagh, 1991; Johnson, 2016). V1 serves as an ideal candidate for such a neurophysiological investigation because it is the first stage of the visual system where neurons selectively respond to oriented edges (Hubel, 1962; Hubel and Wiesel, 1968). Some neurons are tuned to luminance edges, some are tuned to chromatic edges, and some are tuned to a combination of luminance and chromatic edges (Leventhal, 1995; Friedman, 2003; Garg, 2019). Decades of research using rigorous experiments and quantitative modeling has improved our understanding of how luminance edges are encoded by V1 neurons (Movshon et al., 1978a, b; Schumer,

1984; DeAngelis, 1993; Carandini et al., 1997; DeAngelis, 2004; Rust et al., 2005). Such a level of understanding about the encoding of chromatic edges is far behind. Knowing the spatial representation of color will be important for understanding how form and color are jointly processed, and advancing models of visual processing (Shapley, 2011; Rentzeperis, 2014; Johnson, 2016).

How information about scenes is used for behavior is incomplete without understanding the link between neural activity and behavior. Key insights into the contribution of neural activity to behavior have been derived from causal manipulation techniques (Salzman et al., 1990; DeAngelis et al., 1998; Gold, 2000; Tehovnik et al., 2004; Afraz et al., 2006; Ni, 2010; Schmid et al., 2010; Katz, 2016; Kinoshita, 2019). Techniques for neural activation in macaques are fast and powerful whereas for neural inactivation are not, thus prohibiting reversible manipulation on a trial-by-trial basis (Wurtz, 2015). A fast and powerful neural inactivation is the need of the hour. Inactivation via optogenetic technique is a promising solution (Boyden et al., 2005). V1 serves as an ideal candidate for testing such a technique because neural inactivation leads to interpretable behavioral deficits (Gross, 1999).

In this dissertation, I combined neurophysiological, behavioral and computational approaches to investigate the role of V1 neurons in spatial and chromatic processing, and the relationship between V1 neural activity and behavior. The current chapter provides an introduction to our understanding of V1 neurophysiology and its relationship to behavior. The current chapter is divided into four main sections: “From Retina to V1”, “Functional cell types in V1”, “Local circuits in V1”, and “Link between V1 neural activity

and behavior". Throughout the four sections, I restrict the description to spectral and spatial response properties of cells and, review the work done in various species (mice, cats, tree shrews, marmosets, monkeys and humans). There are certainly important species-specific differences but for the sake of simplicity, I have combined them to provide a holistic view. I conclude this section by stating my three research aims.

1.1 FROM RETINA TO V1

The primate vision at moderate or high light level begins with the conversion of photon catches into voltage signals by three classes of cone photoreceptors—long- (L), medium- (M) and short-wavelength (S) sensitive cones. The signals from the cone photoreceptors are transmitted to the retinal ganglion cells (RGCs) via bipolar cells. The signals along the way are shaped by the inhibitory interneurons in the circuit. It is at the RGC stage where communication happens via spiking activity.

The receptive fields (RFs) of RGCs have a spatially antagonistic center-surround structure that is well suited for detecting edges (Kuffler, 1953). There are at least 20 different kinds of RGCs (Masland, 2001; Rhoades, 2019). Of those, the physiology of midget, parasol and small-bistratified cells are well understood. Together, they comprise ~70% of the RGCs in the primate retina and, combine cone signals to transmit luminance, red-green, and blue-yellow light information separately (Dacey, 2000).

Midget RGCs are dominant in the central retina and, have small receptive fields. These cells compare the photon catches in the L- or M-cone center to the photon catch in the surrounding L/M-cones (red-green). Because midget RGCs compare cone signals

across spatial locations and spectral sensitivities, they are thought to contribute to both color and spatial vision. Parasol RGCs compare the summed activity of L- and M-cones (luminance) in the center to summed activity of L- and M-cones in the surround (Field et al., 2010). These cells are color blind, have larger RFs than midget RGCs, and are thought to participate in depth and motion processing. Bistratified RGCs, compare the photon catches in the S-cone center to the photon catches in the surrounding L- and M-cones (Dacey and Lee, 1994). These cells are thought to be the conduit of blue light information. At least, some OFF-midget cells signal decrements in S-cone activity and are thought to be the conduit of the yellow light information (Field et al., 2010; Wool, 2019) .

Axons from the RGCs travel to a part of visual thalamus known as the lateral geniculate nucleus (LGN). Parasol RGCs project to the magnocellular layers of the LGN (layers 1 & 2). Midget RGCs project to the parvocellular layers of the LGN (layers 3–6). Small bistratified RGCs project to koniocellular layers—the intercalated regions between the layers (Casagrande, 1994). The RF structures and the response properties of parvocellular and magnocellular LGN cells are mostly similar to their input RGCs (Derrington et al., 1984; Derrington and Lennie, 1984; Reid, 1992; Tailby et al., 2008). The properties of koniocellular cells are the least well understood as they represent a heterogeneous population (Sincich et al., 2004; Tailby et al., 2008; Klein, 2016).

Majority of LGN signals are transmitted to area V1. Parvocellular neurons project to layer 4Cβ, magnocellular neurons project to layer layer 4Cα and, koniocellular neurons project to layers 4A, 3 and 1 (Chatterjee and Callaway, 2003; Casagrande, 2004). It is in

V1 where a major spatial transformation of LGN signals takes place (Hubel and Wiesel, 1962).

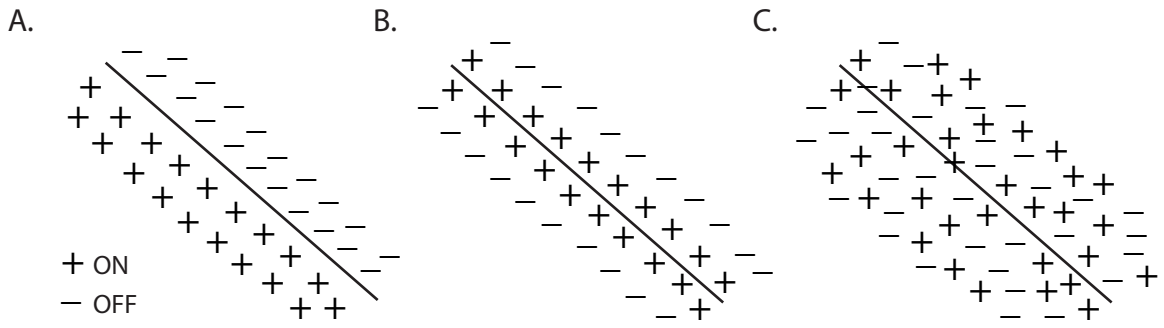

Figure 1.1 Original receptive field (RF) description of simple and complex cells by Hubel and Wiesel. **A.** A diagram of an odd-symmetric simple cell RF that has non-overlapping ON (+) and OFF (-) subregions. Such an arrangement of ON and OFF subregions makes simple cells sensitive to the orientation of edges. **B.** An even-symmetric simple cell RF that has an ON subregion flanked by two OFF subregions. **C.** A diagram of a complex cell RF that has overlapping ON and OFF subregions.

1.2 FUNCTIONAL CELL TYPES IN V1

In 1960's, Hubel and Wiesel provided the first description of response properties of V1 neurons; first, in cats and later, in macaque monkeys (Hubel, 1959; Hubel and Wiesel, 1962, 1968). Using a simple set of visual stimuli and classification criteria, they divided the cells into two major types: simple and complex. Simple cells have non-overlapping ON and OFF subregions within their RFs that responded to luminance increments and decrements, respectively (**Figure 1.1A–B**). However, the ON and OFF subregions did not have a concentric center-surround geometry. Rather, they were adjacently placed to each other. Such a RF geometry could explain the orientation-selective responses of simple cells to elongated bars of light. Complex cells, like simple cells, displayed orientation selectivity but responded to bars of luminance increments and decrements within the same part of their RFs i.e. the ON and OFF subregions were superimposed

(**Figure 1.1C**). Based on these response properties, Hubel and Wiesel proposed a wiring diagram of simple and complex cell RFs. Simple cells receive direct inputs from LGN cells; ON subregion receives inputs from ON-center LGN cells and OFF subregion receives inputs from OFF-center LGN cells. Complex cells received inputs from multiple simple cells with same orientation selectivity but different arrangements of ON and OFF subregions. These connectivities were later confirmed in cat V1 (Reid and Alonso, 1995; Alonso, 1998).

From these investigations, it was clear that simple and complex cells responded to luminance contrast and orientation of edges but it was not clear how these cells contributed to spatial vision. Quantitative understanding of the spatial RF structure and spatial integration mechanisms was imperative. Rigorous investigations over the next few decades formalized the spatial RF and spatial integration mechanisms of simple and complex cells (Movshon et al., 1978b, a; Jones, 1987; DeAngelis, 1993; Carandini et al., 1997; Ringach, 2002a; Rust et al., 2005). A simple cell was modeled as a linear spatial filter that computed the weighted sums on an image, with weights defined by the RF profile and the output of this filtering was half-rectified; only the output that exceeds a threshold results in a response (Movshon et al., 1978a; DeAngelis, 1993; Carandini et al., 1997).

Although conceptually straightforward, the spatial linearity of simple cells was not explained by the original wiring diagram. Intracellular measurements from cat V1 refined the wiring diagram and proposed a push-pull or excitation-inhibition model to explain linearity (Ferster, 1988; Tolhurst, 1990; Hirsch, 1998; Ferster, 2000). Under this model,

simple cells displayed antagonism (in addition to spatial antagonism) within individual subregions; for example, ON subregions were excited (push) by ON-center LGN cells and inhibited (pull) by OFF-center LGN cells and hence the name “push-pull”. The spatial RF structure was modeled as a two-dimensional Gabor function (Jones, 1987; Ringach, 2002a).

A complex cell was modeled as integrating the output of multiple simple cells (linear filters) with overlapping RFs but different arrangements of ON and OFF regions (Movshon et al., 1978b; Rust et al., 2005). This model captured the non-linear spatial integration and thus explained the phase-invariant responses to edges. Together, these quantitive studies provided an implementation, algorithmic and computational view of simple and complex cells (Marr, 1976; Carandini, 2006).

Neurophysiological investigations of spatial vision have traditionally used stimuli that are modulated in luminance (achromatic) contrast. However, spatial vision relies on color contrast as well (Johnson, 2016). Some studies have indeed proposed that the encoding of form based on color contrast occurs in a manner that is similar to the encoding of form based on luminance contrast (Cavanagh, 1991).

Many cells in monkey V1 are color-responsive (Hubel and Wiesel, 1968; Dow and Gouras, 1973; Livingstone and Hubel, 1984; Lennie et al., 1990; Leventhal, 1995; Friedman, 2003). Some V1 cells are only chromatically opponent—“single-opponent”, responding to large, uniform areas of color (Shapley, 2011). Some are chromatically and spatially opponent—double-opponent (DO), responding strongly to colored edges and weakly to full field stimuli (Hubel and Wiesel, 1968). Yet others respond to both

chromatic and luminance edges and could be the neural correlates of cue-invariant edge detection (Gouras, 1979).

Of those, DO cells are well suited to contribute to the spatial processing of color. Indeed, DO cells have been hailed as a key contributor to perceptual phenomena that heavily rely on spatial processing of color: color constancy and simultaneous color contrast (Gegenfurtner, 2003; Conway and Livingstone, 2006). Ironically, it is not clear how do they analyze color spatially. The spatial RFs of DO cells are contentious and how they integrate visual signals across their spatial RFs is unknown. Early qualitative investigations advocated for the idea that DO cells had center-surround RFs and were therefore orientation-untuned (Hubel and Wiesel, 1968; Livingstone and Hubel, 1984). Some quantitative studies supported this result (Conway, 2001; Conway and Livingstone, 2006). Other studies refuted it, and provided evidence that DO RFs are Gabor-like (Johnson et al., 2004, 2008). The differences in results could be attributed to the use of different stimuli and classification criteria.

At least some DO cells display “push-pull” responses suggesting that the spatial integration could be linear (Conway and Livingstone, 2006). Yet there are others that appear to be non-linear (Horwitz et al., 2005; Conway and Livingstone, 2006). Direct measurements of spatial integration of visual signals is lacking. As a result, it is not clear how DO cells combine signals across their spatial RFs. Revealing the spatial RF structure and spatial integration of visual signals will be a step towards understanding the role of DO cells in image processing and their underlying circuitry.

1.3 LOCAL CIRCUITS IN V1

Neurons do not operate in isolation, but rather represent one component of a larger circuitry. Understanding neural coding involves knowledge of inputs, the way a neuron integrates those inputs, and its interaction with other neurons in a network. So far, I have treated neurons operating as independent entities. In this section, I provide a brief overview of the flow of information and organization of local circuits in V1.

The simplest model of information flow can be described as a two-step process (Callaway, 2004). The first step is from the LGN to layer 4 and the second step is from the layer 4 to superficial layers (layers 2 & 3). Simple cells are most likely to be present in the deeper layers (layers 4 & 6) whereas complex cells are most likely to be present in the superficial layers (layers 2 & 3) (Ringach, 2002b) but see (Mooser, 2004). The projections from LGN to layer 4, and layer 4 to layer 2/3 connect strongly to both excitatory and inhibitory neurons (Agmon, 1992; Gibson, 1999; Dantzker, 2000). The feedforward processing steps are modulated by signals from local connections within the same layer, deeper layers of V1 and feedback from higher order cortical areas (to layer 1). Almost half of the signals from the superficial layers are transmitted to higher order visual cortical areas (Callaway, 1996). The rest is sent to deeper layers (layers 5 & 6) within V1. As simple as this description may seem, the information flow is far more complicated. Next, I expand on the this simplistic description.

V1 receives input from LGN cells in a layer-specific manner (Chatterjee and Callaway, 2003; Callaway, 2004). Layers 4 and 6 are the primary recipients. Inputs to layer 4 are monocular and alternate spatially between ipsilateral and contralateral eyes (Hubel,

1969). Layer 4Cβ neurons receive parvocellular inputs and are thought to carry form and color information (Hubel, 1972; Chatterjee and Callaway, 2003). The majority of parvocellular recipient neurons project to blobs and inter-blobs in layers 2 and 3 in an unbiased manner. Neurons in the blobs are mostly sensitive to color, and are orientation untuned whereas neurons in the inter-blobs are sensitive to either color or luminance or both depending on the convergence of parvocellullar recipient neurons, and are orientation tuned (Garg, 2019) but see (Economides, 2011). The neurons in the blobs project to V2 thin cytochrome oxidase (CO) stripes whereas the neurons in the inter-blobs project to pale CO stripes.

Layer 4Cα neurons receive magnocellular input and are thought to carry motion information (Hubel, 1972; Chatterjee and Callaway, 2003). The magnocellular recipients in the upper part of layer 4Cα project to layer 4B. The layer 4B neurons that exclusively receive input from magnocellular recipients are the excitatory spiny stellate cells. These spiny stellate cells project to area MT which specializes in the analysis of motion (Yabuta, 2001). Thus, the layer 4B neurons to certain extent preserve the stream specific information from their inputs in a cell-type specific manner.

Some parvocellular recipient neurons project to layer 4B. The projections to layer 4B are restricted to the excitatory pyramidal cells (Yabuta, 2001). These pyramidal neurons are also driven by magnocellular recipients and project to area V2, perhaps to the thick CO stripes which is selective for motion and binocular processing (Yarch, 2017).

Projections from koniocellular cells are found in layers 4A, 3 and 1 (Hendry, 1994; Chatterjee and Callaway, 2003). Projections to layer 3 are within the CO blobs. The LGN afferents in layer 4A and blobs show blue-yellow color opponency, with the blob being 'Blue-ON' and layer 4A being 'Blue-OFF'. It is likely that the blue-yellow input to layers 3 and 4A mixes directly with the parvocellular input relayed from layer 4Cβ (Sawatari, 2000). This mixing could presumably result in diverse color tuning (Lennie et al., 1990; Johnson et al., 2004; Horwitz et al., 2005, 2007; Horwitz and Hass, 2012) .

Most output from V1 to extrastriate cortices is through layer 2 & 3 neurons. Neurons in this layer are mostly binocular, sensitive to color and/or the orientation of visual stimulus and, arranged in a columnar manner (Hubel, 1969). The layer 2 & 3 pyramidal neurons and the fast-spiking (basket cells) interneurons have similar stimulus preferences, perhaps as a consequence of the same feedforward sources of input (Hirsch, 2003). These fast-spiking interneurons connect strongly to the somata of their neighboring pyramidal cells allowing them to control pyramidal neurons' spiking responses (Moore, 2010).

Connections between the deeper and the superficial layers appear to be canonical. Layer 6 pyramidal neurons receive input from LGN collaterals, collect input from a broad range of local sources and project to V1 layer 4C neurons without any specificity (Freund, 1989; Callaway, 2004). Similarly, layer 5 pyramidal neurons receive input from layer 4C collaterals, collect input from a broad range of local sources and project to V1 layer 2 & 3 neurons without any specificity to blobs or inter-blobs. Both layers 5 and 6 appear to provide direct disynaptic feedback to superficial layers; layer 6 to layer 4C

and layer 5 to layers 2 & 3. Layer 6 neurons project back to LGN and appear to sharpen the temporal and spatial resolution of visual signals (Hasse, 2017). Layer 5 neurons project to pulvinar and superior colliculus, and appear to provide a swift communication between the sensory and motor system (Guillery, 2002).

1.4 LINK BETWEEN V1 NEURAL ACTIVITY AND BEHAVIOR

A central goal of systems neuroscience is to understand the moment-by-moment relationship between the signals carried by sensory neurons and behavior. One approach is to measure the neural activity and correlate it with the subject's response in a well-controlled behavioral task. A powerful approach is to perturb neural responses, and understand how it impacts behavior. Next, I discuss each of these approaches in detail.

There is a long history of studies comparing the sensitivity of single cortical neurons to the behavioral sensitivity of humans and nonhuman primates in detection and discrimination tasks (Parker and Newsome, 1998). One of the earliest studies to develop a framework for analyzing the link between neural activity and behavior used signal detection theory (Green and Swets, 1966; Tolhurst et al., 1983). Under this framework, a "neurometric function" is created (using receiver operating characteristic analysis) that describes the ability of an ideal observer to detect/discriminate stimuli based on neural activity. In the particular work, the authors obtained the single-unit spiking responses from cat and monkey V1 in response to drifting sinusoidal gratings at different contrasts, and compared the neurometric functions to the psychometric functions of humans who performed a contrast detection task. This way of linking neural

activity and behavior was innovative but there were two major caveats. First, the neural and behavioral data were collected from different species. Second, the study was based on measurements of neural and behavioral responses that were acquired separately using non-identical stimuli.

One of the earliest attempts to collect simultaneous neural and behavioral response from the same specie (macaque monkey) was performed by Newsome, Movshon and colleagues in late 1980s and early 1990s (Newsome, 1989; Britten, 1992). These studies focused on the role of area MT in a coarse direction discrimination task in which awake-behaving monkeys discriminated the direction of motion in a dynamic random-dot stimulus. By comparing the neurometric and psychometric functions, the authors found that the sensitivity of the average MT neuron was comparable to the sensitivity of the monkey. The authors made further advancement by defining a metric that quantified the trial-by-trial covariation of neural and behavioral response. This metric was called the “choice probability”, which lies between a value of 0.5 and 1, and tends to be higher for sensitive neurons (Shadlen et al., 1996). Since then, numerous studies in many cortical areas including V1, have used choice probability as a metric for quantifying the link between cortical neural activity and behavior (Cook, 2002; Uka, 2004; Purushothaman, 2005; Nienborg and Cumming, 2006; Palmer et al., 2007; Law, 2008; Nienborg and Cumming, 2009; Hass and Horwitz, 2013; Nienborg and Cumming, 2014).

The use of choice probability has met with two important criticisms that complicate interpretation. First, the choice probability has at least some feedback contributions;

meaning, that the variation in neural activity is a consequence of the decision made by the subject (post-decisional and not pre-decisional) (Nienborg and Cumming, 2009). Second, a simulation study has shown that a neuron can be correlated to behavioral judgement without actually contributing to the behavioral task (Cohen and Newsome, 2008). Given these evidences, choice probability is not ideal for understanding how trial-by-trial variations in neural activity is linked to behavior.

A powerful approach is to perturb neural activity and understand its impact on behavior. Microstimulation is one such tool for neural activation in primates (Salzman et al., 1990; DeAngelis et al., 1998; Seidemann, 1998; Gold, 2000; Afraz et al., 2006). It is powerful, and has high temporal and spatial precision. Microsimulation of macaque V1 has been shown to influence behavior in a manner that is consistent with phosphene induction (Tehovnik et al., 2003; Ni, 2010). Microstimulation causes monkeys to routinely make saccades into the RF locations of stimulated V1 neurons. Therefore, the effect of microstimulation is equivalent to adding spikes to neural response.

Microstimulation cannot be used for deleting spikes. This is because microstimulation injects currents into both excitatory and inhibitory cells causing a net increase in the number of spikes, and thus increasing variability in V1 activity. As a result, microsimulation cannot be used for dissecting the relative contribution of variability that is present in V1 neural activity (“upto V1”) versus variability downstream of V1 (“post-V1”) to monkey’s choices.

Neural inactivation is well suited for dissecting the contribution of variability before and after V1. Current neural inactivation techniques in primates are powerful but slow and

therefore, prohibit perturbation on a trial-by-trial basis (Wurtz, 2015). The modern technique of optogenetics, which is faster, has only produced weak effects so far (Afraz et al., 2015; Acker et al., 2016; Fetsch et al., 2018). Therefore, a fast, reversible and powerful neural inactivation tool is needed that can allow us to understand the link between variability in V1 responses and behavior.

1.5 RESEARCH AIMS

Based on the introduction, I define my three research aims.

Aim 1: To determine whether individual DO neurons encode chromatic edges the same way as simple cells encode luminance edges. Chapter 2 is devoted to this aim.

Aim 2: To determine whether DO neurons combine signals across their spatial RF the same way as simple cells do. Chapter 3 is devoted to this aim.

Aim 3: To determine whether fast, powerful and reversible neural inactivation of macaque cortex is achievable. Chapter 4 is devoted to this aim.

2. SPATIAL RECEPTIVE FIELD STRUCTURE OF DOUBLE-OPPONENT AND SIMPLE CELLS IN MACAQUE PRIMARY VISUAL CORTEX

2.1 ABSTRACT

Double-opponent (DO) cells are well-suited to contribute to the spatial processing of color due to their spatially opponent and cone-opponent receptive fields (RFs). However, the representation of visual images by DO cells in monkey primary visual cortex is unclear because the spatial RF structure of DO cells has not been fully characterized. Early reports suggested that DO cells have center-surround RFs, but more recent studies have shown that some DO cells are orientation-tuned. To characterize the RFs of DO cells, we mapped them in awake fixating macaques, fit them with parametric models, and compared them to the benchmark of orientation-tuned simple cells. Neurons were stimulated with colorful, dynamic white noise patterns. Spike-triggered averaging was used to classify each neuron as simple, DO, or neither and to measure its spatial RF. The spatial RF of each neuron was fitted with a Gabor model and a Difference of Gaussians (DoG) model. The Gabor model provided the more accurate description for most DO cells, a result that is incompatible with a center-surround RF organization. The superiority of the Gabor fits was slightly more decisive for simple than for DO cells. A modified (non-concentric) DoG model performed nearly as well as the Gabor model for DO cells.

2.2 INTRODUCTION

Double-opponent (DO) cells encode colored edges. They are cone-opponent and thus sensitive to stimulus chromaticity, and they have opposite chromatic preferences in different parts of their receptive field (RF), rendering them sensitive to spatial contrast. These defining characteristics are undisputed, but the spatial structure of DO cells' RFs is controversial.

DO cells in primate primary visual cortex (V1) were originally reported to have a center-surround RF organization, suggesting that they are orientation-untuned (Hubel and Wiesel, 1968; Poggio, 1975; Michael, 1978; Livingstone and Hubel, 1984). On the other hand, more recent experiments have shown that most DO cells are orientation-tuned (Johnson et al., 2001, 2008) but see (Conway, 2001; Conway and Livingstone, 2006). Several factors likely contribute to the difference in findings. For example, one factor is the use of different stimuli that led to different conclusions. Another factor is that most descriptions of DO cell RFs have been either 2-dimensional (2-D) and qualitative, or 1-D and quantitative (e.g. orientation tuning). A complete, quantitative description of DO cell spatial RF structure is not yet available.

Knowing the spatial structure of DO cell RFs is important for understanding their role in image processing. For example, unoriented RFs could contribute to simultaneous color contrast and could be responsible for the well-documented deficiencies in form vision at isoluminance (Gregory, 1977; Livingstone, 1987; Mullen, 2002). Oriented RFs could contribute to shape-from-shading—the ability to estimate the 3-D shapes of objects from shading cues (Kingdom, 2003; Kunsberg, 2018).

We stimulated every neuron that we isolated with the same white noise stimulus to maintain a constant adaptation state across experiments. We analyzed the data by spike-triggered averaging to identify DO cells and to measure their spatial RFs. We fit each spatial RF with two models. The first, the difference of Gaussians (DoG) model, assumes that DO cell RFs are orientation-untuned (Rodieck, 1965). The second, the Gabor model, assumes that they are orientation-tuned (Jones, 1987; Ringach, 2002a). Both models provide a concise description of RF organization that is useful for image analysis, summarizing data, and making quantitative comparisons between neurons. We compared model fits between DO cells and simple cells—a benchmark cell type that is orientation-tuned (Hubel and Wiesel, 1968; Jones, 1987; Ringach, 2002a, b; Moore IV, 2012).

The Gabor model outperformed the DoG model for most of the simple cells studied, which was expected from previous studies (Jones, 1987; Ringach, 2002a; Moore IV, 2012). Most DO cells were also more accurately described by the Gabor model, which is a novel result. The goodness-of-fit of the Gabor model was similar for simple and DO cells. Some DO cell RFs consisted of a circular center and a crescent-shaped surround, as has been reported previously (Conway, 2001; Conway and Livingstone, 2006). A slight modification of the DoG model captured such RFs and performed nearly as well as the Gabor model for DO cells but poorly for simple cells. Together, these results show that simple and DO RFs are both well-described by the Gabor model, they are poorly described by the DoG model, but the center-crescent surround model is a reasonable description for many DO cells.

2.3 METHODS

2.3.1 General

All protocols conformed to the guidelines provided by the US National Institutes of Health and the University of Washington Animal Care and Use Committee. Data were collected from two male and two female rhesus macaques (Macaca mulatta) weighing 7–13 kg. Each monkey was surgically implanted with a titanium headpost and a recording chamber (Crist Instruments) over area V1. Eye position was continuously monitored using either an implanted monocular scleral search coil or an optical eye-tracking system (SMI iView X Hi-Speed Primate, SensoMotoric Instruments).

2.3.2 Monitor calibration

Stimuli were presented on a cathode-ray tube (CRT) monitor (Dell Trinitron Ultrascan P991) with a refresh rate of 75 Hz and background color as uniform gray (x = 0.3, y = 0.3, Y = 43–83 cd/m^2). Monitor calibration routines were adapted from those included in the Matlab Psychophysics toolbox (Brainard, 1997). Emission and voltage-intensity relationships of each monitor phosphor were calibrated using a spectroradiometer (PR650, PhotoResearch). The color resolution of each channel was increased from 8 to 14 bits using a Bits++ video signal processor (Cambridge Research) at the expense of spatial resolution; each pixel was twice as wide as it was tall.

2.3.3 Task

The monkeys sat in a primate chair 0.7–1.0 m from a CRT monitor in a dark room during the experiments. The monkeys were trained to fixate a centrally located dot measuring 0.2 x 0.2° and maintain their gaze within a square 1.0–2.0° fixation window. Successful fixation was rewarded, and fixation breaks aborted trials.

2.3.4 Electrophysiological recordings

We recorded spike waveforms from well-isolated V1 neurons using extracellular tungsten microelectrodes (Frederick Haer, Inc.) that were lowered through dura mater by a hydraulic microdrive (Narishige Inc. or Stoelting Co.). Electrical signals were amplified and digitized at 40 kHz online (Plexon Inc.) and stored in a PC.

After isolating a waveform, we mapped the RF boundaries with oriented bars of different colors based on the modulation of the spiking activity.

2.3.5 Visual stimuli and experimental protocol

Each neuron was stimulated with white noise chromatic checkerboards (Horwitz et al., 2005, 2007). Each stimulus frame was a grid of 10 x 10 pixels, with each pixel subtending 0.2 x 0.2°. The stimulus changed on every screen refresh. The intensity of each phosphor was modulated independently according to a Gaussian distribution with a standard deviation of 5–15% of the physically achievable range. The space-time averaged intensity of each phosphor was equal to its contribution to the background. Neuronal responses to the white noise stimuli were analyzed using spike triggered averaging (**Figure 2.1A**). We intentionally screened for neurons with clear spike-triggered averages (STAs) in these experiments. Many neurons that were recorded did

not have clear STAs online and were passed over for data collection.

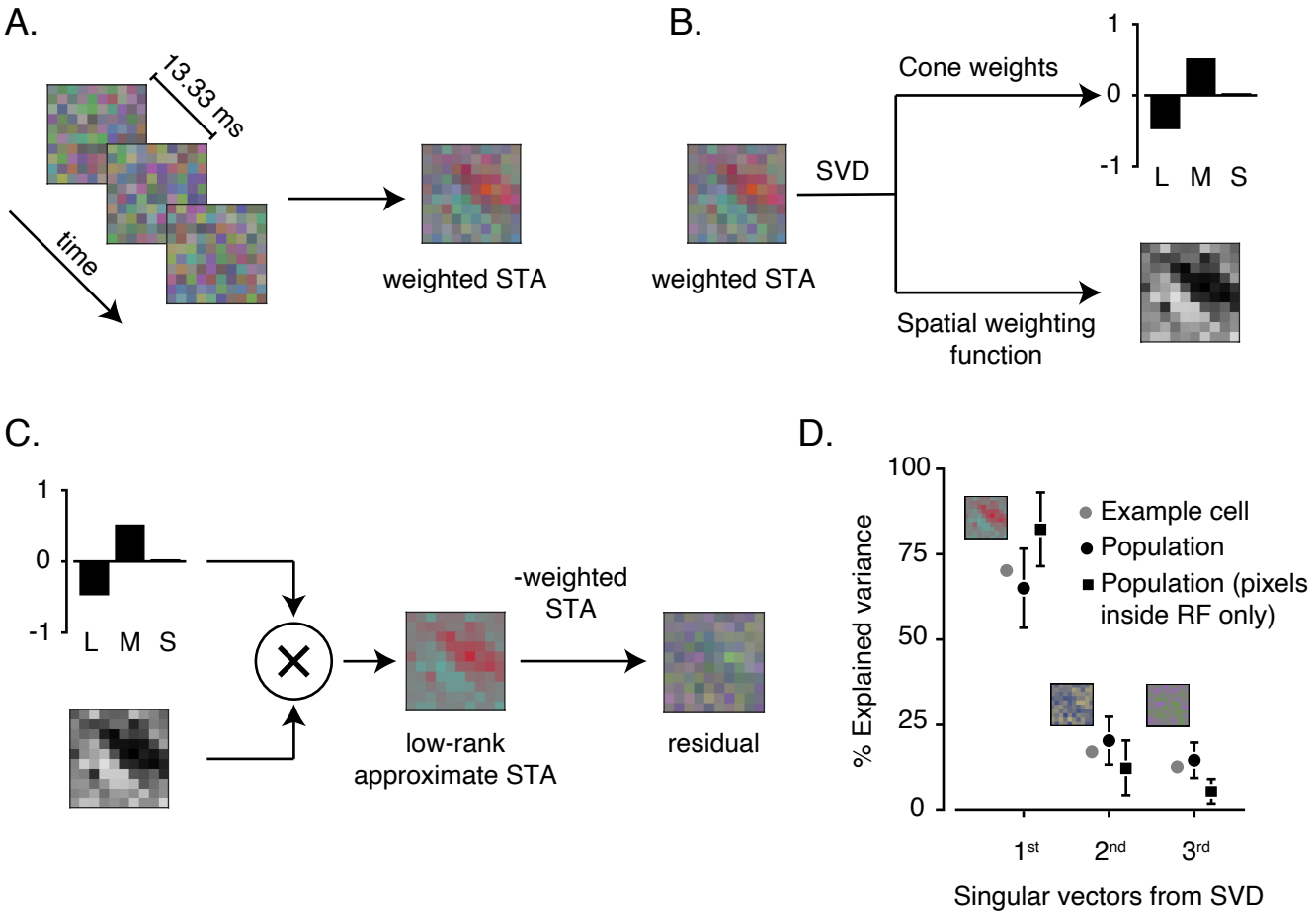

Figure 2.1. Derivation of cone weights and spatial weighting function **A.** Computing the weighted STA (the weighted sum of the peak STA frame and two flanking frames)(right) from spike triggered white noise stimuli (left). **B.** Singular value decomposition (SVD) of the weighted STA reveals cone weights and spatial weighting function. **C.** Reconstructing a low-rank approximation of the weighted STA by multiplying cone weights and spatial weighting function. Subtracting the weighted STA from the the low-rank approximation yields the residual, which has little structure. **D.** Percent explained variance plotted against the three sets of singular vectors for the example cell and the population (mean ± SD). Cone weights and the spatial weighting function constitute the 1st singular vectors. Percent explained variance was derived from the singular values using SVD over entire 10 pixels x 10 pixels of spatial weighting function (filled black circles) or omitting pixels outside of the RF (filled black squares).

2.3.6 Cone weights and spatial RF

For each cell, we identified the frame from the spike-triggered averaged stimulus (STA) that differed most from the background, based on the sum of squared red, green, and blue pixel intensities (negative intensities were defined as those below the contribution to the background). We then took the weighted average of the peak and the two flanking frames (10 pixels x 10 pixels x 3 color channels), reshaped it into a 100 x 3 matrix, and used a singular value decomposition (SVD) to separate this weighted STA into a color weighting function and a spatial weighting function, defined as the first row and column singular vectors, respectively (**Figure 2.1B**) (Horwitz and Albright, 2005). The color weighting function and the spatial weighting function together captured nearly 65% of the variance in the weighted STA (**Figure 2.1C–D**). This fraction is biased downward by pixels outside of the RF. Restricting analysis to pixels inside the RF increased the explained variance to 82%.

The color weighting function, which quantifies neuronal sensitivity to modulations of the red, green, and blue phosphors of the display, was converted to cone weights that are assumed to act on cone contrast signals (Weller, 2018). Cone weights were normalized such that the sum of their absolute values was 1 (Derrington et al., 1984; Johnson et al., 2004; Horwitz and Albright, 2005). We analyzed only those cells that were spatially opponent (**see Cell Screening**). As a result, each cell had cone weights with different signs in different parts of the RF. There is no principled way of describing such a cell as having cone weights of one sign or the other. Therefore for convenience, we constrained the M-cone weights of all the cells to be positive, and we classified cells as

cone-opponent or cone non-opponent by evaluating the signs of L- and S-cone weights relative to the M-cone weight.

2.3.7 Cell screening

We recorded from 393 V1 neurons and omitted 189 from the analyses on the basis of four criteria. Every neuron was required to have an STA with (1) high signal-to-noise ratio (SNR), (2) interpretable structure, (3) spatial opponency, and (4) cone weights that were either clearly opponent or clearly non-opponent. Below, we explain the rationale for each criterion and how they were implemented.

We excluded cells with low signal-to-noise ratio (SNR) because noisy STAs could lead to inaccurate estimates of color and spatial weighting functions. SNR was computed by comparing the peak STA frame to first STA frame and was defined as follows:

$$SNR = \sum_{i=1}^{N} \left(\frac{I_i}{\sigma} \right)^2$$

where N is the total number of elements within a frame: 10 pixels x 10 pixels x 3 color channels = 300 elements, I is the pixel intensity of each element relative to background in the peak STA frame and σ is the standard deviation of the 300 elements (pixel intensities relative to the background) in the first STA frame. Pixel intensity of each element was divided by this standard deviation to obtain z-scores so that each element had (approximately) a standard normal distribution under the null hypothesis of no signal. We summed the squared z-scores of the peak STA frame and omitted from

analysis the 60 cells for which this sum failed to reach a statistical threshold ($p < 0.0001$ χ^2 test, df=300).

We excluded cells that combine cone inputs non-linearly because their STAs do not reflect their stimulus tuning accurately (Horwitz et al., 2005). We identified nonlinear neurons using a non-linearity index (NLI) (Horwitz et al., 2007). The NLI uses the STA and the spike-triggered covariance to find the maximally informative stimulus dimension under a multivariate Gaussian assumption (Pillow, 2006). For each cell, we projected the stimuli shown in the experiment onto the maximally informative dimension and binned the projections, excluding the upper and lower 5% to avoid the influence of outliers. We calculated the average firing rate across the stimuli within each bin. The relationship between firing rate and stimulus projection was fit with three regression equations.

$$y_{linear} = b_0 + b_1 x$$

$$y_{quadratic} = b_0 + b_1 x^2$$

$$y_{full} = b_0 + b_1 x + b_2 x^2$$

The goodness-of-fit of each regression was quantified with an R^2 statistic. The NLI is defined as

$$NLI = \frac{R^2_{quadratic} - R^2_{linear}}{R^2_{full}}$$

The NLI attains its theoretical maximal value of 1 when the inclusion of a linear term does not improve the regression fit. This would be the case, for example, for a V1

complex cell whose response is invariant to contrast polarity. NLI attains its theoretical minimum value of –1 when the inclusion of a quadratic term does not improve the regression fit as would be the case for a purely linear cell. Twenty-six cells were excluded on the basis that their NLI was > 0.

We excluded cells that were spatially non-opponent because these cells cannot be DO or simple. We identified spatially non-opponent cells by analyzing the power spectrum of their spatial weighting functions. Spatially non-opponent cells, by definition, had maximal power in the lowest spatial frequency bin. This criterion excluded 54 cells.

We segregated simple cells from DO cells based on cone weights, and we excluded neurons outside of these categories. Cells were classified as simple if their L- and M-cone weights had the same sign, accounted for 80% of the total cone weight, and individually accounted for at least 10%. Cells were classified as DO if they had large magnitude cone weights of different sign. $DO_{LM\text{-}opponent}$ cells were defined as those that had L- and M-cone weights of opposite sign, that together accounted for 80% and individually accounted for at least 30% of the total cone weight. $DO_{S\text{-}cone\ sensitive}$ cells were cone-opponent and had an S-cone weight that accounted for at least 20% of the total. Forty-nine cells that were not categorized as simple, $DO_{LM\text{-}opponent}$, or $DO_{S\text{-}cone\ sensitive}$ were omitted from the analyses.

A total of 204 neurons contributed to the final pool (monkey 1: 42 simple, 57 $DO_{LM\text{-}opponent}$, 37 $DO_{S\text{-}cone\ sensitive}$; monkey 2: 11 simple, 11 $DO_{LM\text{-}opponent}$, 1 $DO_{S\text{-}cone\ sensitive}$; monkey 3: 18 simple, 14 $DO_{LM\text{-}opponent}$, 6 $DO_{S\text{-}cone\ sensitive}$; monkey 4: 1 simple, 4 $DO_{LM\text{-}opponent}$, 2 $DO_{S\text{-}cone\ sensitive}$).

2.3.8 Model fitting of the spatial weighting function

We fit the spatial weighting function of each neuron with three models. Fitting was performed using the inbuilt MATLAB *fmincon* function to minimize the sum of squared errors between the spatial weighting function and the model fit. We describe each of the models below.

2.3.9 Gabor model

The Gabor model was defined as:

$$f(x',y') = Ae^{-\frac{\left(x'^2+\gamma^2 y'^2\right)}{2\sigma^2}} cos\left(\left(2\pi y'/\lambda\right)-\phi\right)$$

where (x',y') is obtained by translating the original coordinate frame to the RF center, (x_c,y_c), and rotating it by an angle θ.

$$x' = (x-x_c)\ cos(\theta) + (y-y_c)\ sin(\theta)$$

$$y' = -(x-x_c)\ sin(\theta) + (y-y_c)\ cos(\theta)$$

λ is the spatial period of the cosine component in °/cycle, and ϕ is the spatial phase. A spatial phase of ϕ = 0° gives an even-symmetric RF whereas spatial phase of ϕ = 90° gives an odd-symmetric RF. The two axes of the Gaussian envelope align with the x' and the y' axes. The parameter A is the amplitude, γ is the aspect ratio, and σ is the standard deviation of the Gaussian envelope along the x' axis.

2.3.10 Difference of Gaussians (DoG) model

The Difference of Gaussians (DoG) model can be written as:

$$f(x,y) = \frac{A_c}{\sqrt{2\pi\sigma_c^2}} exp(-((x-x_c)^2+(y-y_c)^2)/\sigma_c^2) - \frac{A_s}{\sqrt{2\pi\sigma_s^2}} exp(-((x-x_c)^2+(y-y_c)^2))/\sigma_s^2)$$

where A_c and A_s are the amplitudes of the center and surround. σ_c and σ_s are the standard deviations of the center and surround.

2.3.11 Non-concentric DoG model

$$f(x,y) = \frac{A_c}{\sqrt{2\pi\sigma_c^2}} exp(-((x-x_c)^2+(y-y_c)^2)/\sigma_c^2) - \frac{A_s}{\sqrt{2\pi\sigma_s^2}} exp(-((x-x_s)^2+(y-y_s)^2))/\sigma_s^2)$$

This non-concentric DoG model is identical to the DoG model but has 2 additional parameters (x_s,y_s) that allow the surround to be offset from the center.

2.3.12 Evaluating goodness of model fit

We evaluated the quality of model fits by calculating Pearson's correlation coefficient (R) between the data and the model predictions. To avoid overfitting, we used 5-fold cross validation, fitting the model with 80% of the data and testing the model on the remaining 20%. We report the averaged R across the 5 folds.

2.3.13 Quantifying R as a function of SNR

We used a logistic function to describe R as a function of SNR. The logistic function was defined as:

$$R = \frac{A}{1+e^{-b(SNR-c)}}$$

where A is the maximum value, b is the steepness constant and c is the SNR value at which logistic function is half the maximum value. The fit was determined by maximizing likelihood assuming binomial error.

2.3.14 Evaluating goodness of model fit: Bayesian information criterion

Model fits were further quantified using the Bayesian information criterion (BIC). Assuming that the model errors are independent and identically distributed according to a normal distribution, the BIC can be written as:

$$BIC = n \log(RSS/n) + k \log(n)$$

where n is the number of data points (n = 100), RSS is the residual sum of squared errors and k is the number of model parameters.

2.3.15 Evaluating goodness of model fit: sum of squared errors

Model fits were further compared by calculating the sum of squared errors between the data and the fitted model. We used 5-fold cross-validation and report the averaged sum of squared errors across the 5 folds.

2.3.16 Evaluating goodness of model fit: Prediction of spike-triggering stimuli

Model fits were further compared by calculating the ability of the models to predict spiking responses to white noise stimuli. Using 5-fold cross validation, the model was fit to 80% of the data and tested on the remaining 20%. Within the testing data, some white noise stimulus frames evoked a spike and most did not. We assessed the ability of the fitted model to classify frames that evoked a spike versus those that did not by projecting individual stimulus frames onto the fitted RF. To compute classification performance, we compiled a receiver operating characteristic (ROC) from the spike and non-spike distributions of projections (Green and Swets, 1966). The area under the

curve of the ROC was defined as the probability of predicted spikes. We report the averaged probability across the 5 folds.

2.3.17 Spatial opponency index

We defined a spatial opponency index (SOI) that quantifies the degree of antagonism across the RF as:

$$SOI = 1 - \left| \frac{P - N}{P + N} \right|$$

P was defined as the sum of positive values in either the spatial weighting function or the best fitting Gabor function. N was defined similarly but was the sum of negative values. If the sum of positive and negative values were matched, then P and N would be equal, and SOI would be equal to 1. On the contrary, if the RF consisted of a single subregion, then either P or N would be equal to 0, and so would be the SOI.

2.4 RESULTS

We analyzed the responses of 204 V1 neurons from 4 macaque monkeys that met our inclusion criteria (**see METHODS**). RFs of neurons ranged in eccentricity from 1.7° to 8.42° (median = 4.7°). The number of spikes recorded ranged from 209 to 48106 (median = 2215).

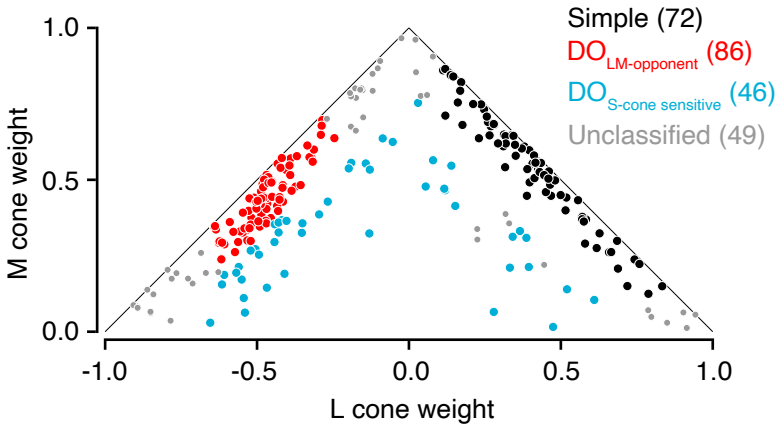

Figure 2.2. Normalized cone weights of simple (black), $DO_{LM\text{-}opponent}$ (red), $DO_{S\text{-}cone\ sensitive}$ (blue) and unclassified (gray) cells. The 49 "unclassified" cells survived all of the inclusion criteria except for the requirement of clear cone-opponency or non-opponency. M-cone weights were constrained to be positive. Points closer to the origin have larger S-cone weights than those far from the origin.

2.4.1 Cone weights

We classified neurons that met our inclusion criteria as simple cells or DO cells based on cone weights (**Figure 2.2**). Simple cells had large magnitude, non-opponent L- and M-cone weights that, together, accounted for 80% of the total cone weight (n=72). DO cells were defined as being cone-opponent and were further classified as LM-opponent (n=86) or S-cone sensitive (n=46) based on cone weight magnitudes and signs. Of the 46 $DO_{S\text{-}cone\ sensitive}$ neurons recorded, 16 were S-(L+M), 26 were (S+M)-L, and 4 were (S+L)-M.

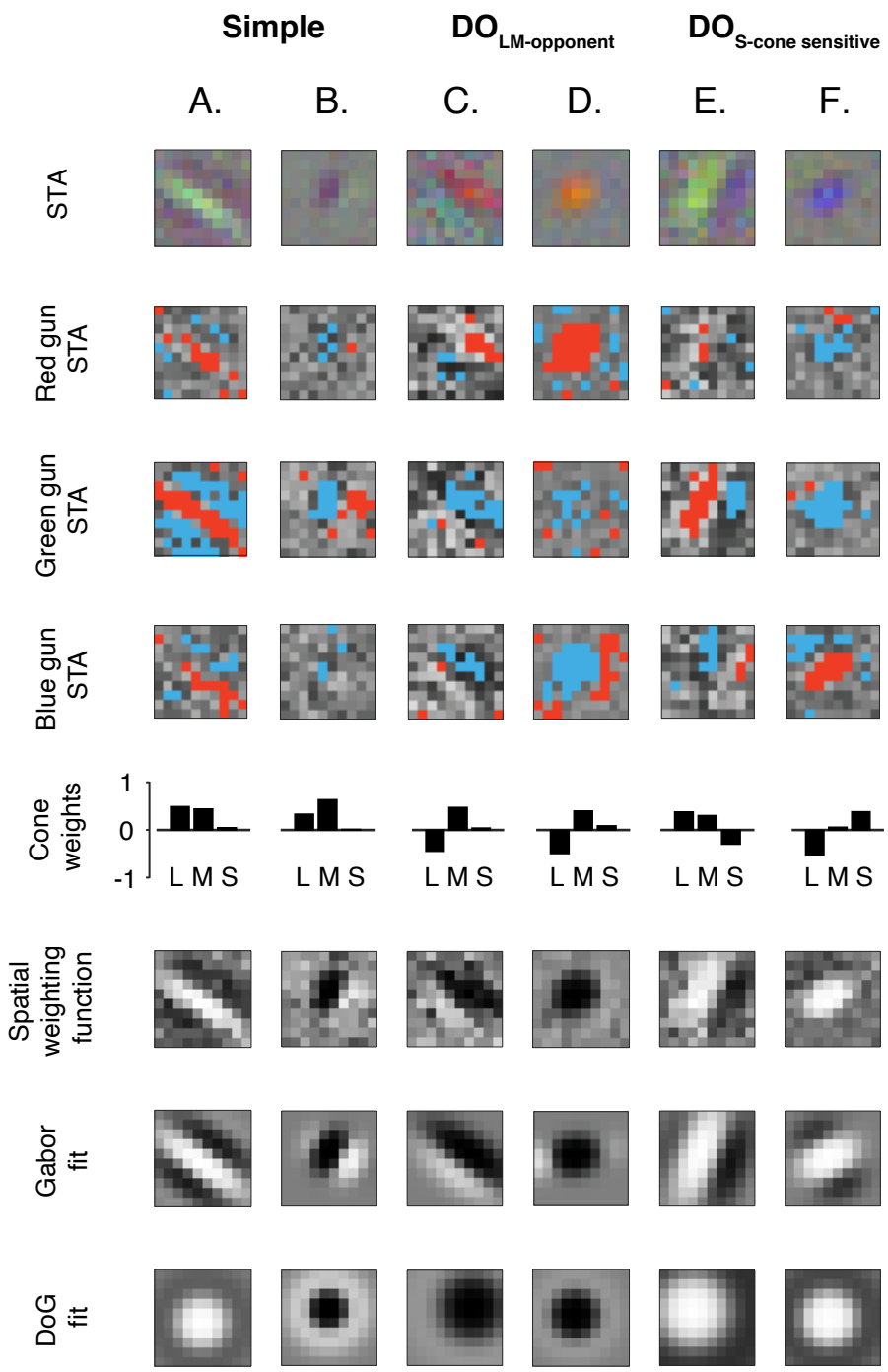

Figure 2.3. Gabor and Difference of Gaussians (DoG) model fits to spatial weighting functions of six example cells. Each spike-triggered average (top row) has been decomposed into red, green, and blue channel components. Significant pixels (z-test, $p < 0.05$) have been colored on the basis of their sign (red = positive, blue = negative). The quality of each model fit was quantified using cross-validated R. **A.** A simple cell with $R_{Gabor} = 0.77$ and $R_{DoG} = 0.45$ **B.** A simple cell with $R_{Gabor} = 0.67$ and $R_{DoG} = 0.59$ **C.** A $DO_{LM\text{-}opponent}$ cell with $R_{Gabor} = 0.45$ and $R_{DoG} = 0.30$ **D.** A $DO_{LM\text{-}opponent}$ cell with $R_{Gabor} = 0.90$ and $R_{DoG} = 0.91$ **E.** A $DO_{S\text{-}cone\ sensitive}$ cell with $R_{Gabor} = 0.68$ and $R_{DoG} = 0.44$ **F.** A $DO_{S\text{-}cone\ sensitive}$ cell with $R_{Gabor} = 0.78$ and $R_{DoG} = 0.75$.

2.4.2 Model comparison: Gabor vs. DoG

STAs of six example neurons illustrate patterns that we observed in the data (**Figure 2.3, 1st–4th rows**). Each cell was classified according to its cone weights (**Figure 2.3, 5th row**). Simple cell RFs consisted of adjacent ON and OFF regions (**Figure 2.3A & 2.3B**). Most simple cell RFs were elongated and clearly oriented (**Figure 2.3A**), but others were nearly circular and less clearly oriented (**Figure 2.3B**). RFs of DO cells displayed similar features: some were clearly oriented (**Figures 2.3C & 2.3E**) whereas others had nearly circular RF centers and diffuse surrounds (**Figures 2.3D & 2.3F**).

To compare the spatial RF organization of simple and DO cells quantitatively, we extracted from each STA the spatial weighting function (**Figure 2.3, 6th row**) and fit it with a Gabor model (**Figure 2.3, 7th row**) and a DoG model (**Figure 2.3, 8th row**). Goodness-of-fit was quantified with cross-validated R between the data and the model predictions (**see METHODS**). Elongated RFs were better fit by the Gabor model than the DoG model because the DoG model fit is constrained to be radially symmetric. The example neurons whose RFs were better fit by the DoG model than the Gabor model had a spatial weighting function that was the most nearly radially symmetric by eye (**Figure 2.3D & 2.3F**).

The Gabor model outperformed the DoG model for most of the cells tested (139/204, $R_{Gabor} > R_{DoG}$). The superiority of the Gabor model was consistent within each subgroup of cells: simple ($p<0.001$; Wilcoxon signed rank test; **Figure 2.4A**), $DO_{LM\text{-}opponent}$ ($p=0.07$; **Figure 2.4B**) and $DO_{S\text{-}cone\ sensitive}$ ($p=0.006$; **Figure 2.4C**). This result

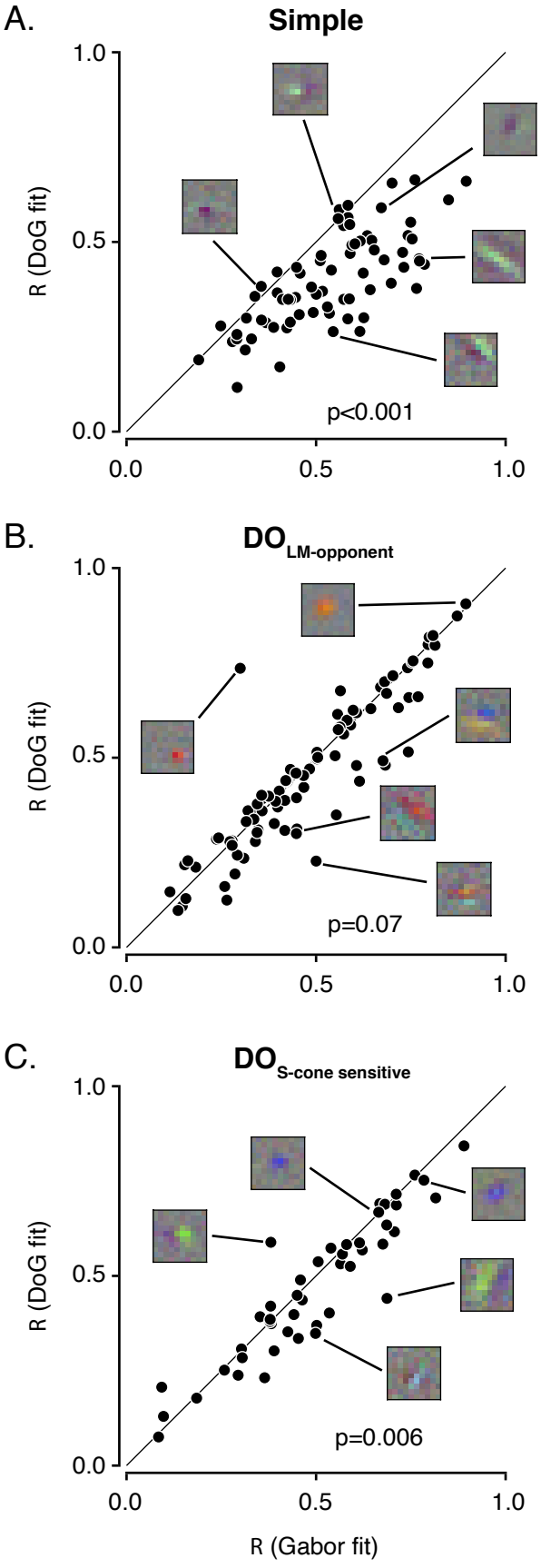

Figure 2.4. Comparison of Gabor and DoG model fits. Cross-validated R is plotted from Gabor fits and from DoG fits for simple (**A**), $DO_{LM\text{-}opponent}$ (**B**), and $DO_{S\text{-}cone\ sensitive}$ cells (**C**). Five example STAs are shown in each panel to illustrate the diversity of RF structures observed and their relationship to R.

shows that DO cells, like simple cells, have RFs that are more accurately described as Gabor functions than as DoG functions. However, the spatial RFs of simple and DO cells were not identical. The difference between R_{Gabor} and R_{DoG} was larger for simple cells than for $DO_{LM\text{-}opponent}$ or $DO_{S\text{-}cone\ sensitive}$ cells ($p<0.001$ for each comparison; simple vs. $DO_{LM\text{-}opponent}$; simple vs. $DO_{S\text{-}cone\ sensitive}$ cells; Mann-Whitney U tests). The difference between R_{Gabor} and R_{DoG} was similar for $DO_{LM\text{-}opponent}$ and $DO_{S\text{-}cone\ sensitive}$ cells ($p=0.25$; Mann-Whitney U test).

We considered the possibility that this difference between simple and DO cells was due to single-opponent cells having been misclassified as DO cells. Single-opponent cells have approximately circularly-symmetric RF that are fit well by a DoG model as long as the surround is weak. We therefore repeated the analysis with a stricter criterion for spatial opponency, requiring DO cells to have at least 1.2 times more power in their peak spatial frequency bin of the power spectrum than in the lowest one (**see METHODS**). Even with this stricter criterion, the difference between R_{Gabor} and R_{DoG} was greater for simple cells than for $DO_{LM\text{-}opponent}$ or $DO_{S\text{-}cone\ sensitive}$ cells ($p<0.001$ for each comparison; simple vs. $DO_{LM\text{-}opponent}$; simple vs. $DO_{S\text{-}cone\ sensitive}$; Mann-Whitney U tests), and the difference between R_{Gabor} and R_{DoG} was similar for $DO_{LM\text{-}opponent}$ and $DO_{S\text{-}cone\ sensitive}$ cells ($p=0.28$; Mann-Whitney U test). These results suggest that single-opponent cells are not the source of the small but real differences between the spatial weighting functions of cells we classified as DO and simple cells. As shown in *Analysis of spatial opponency*, below, DO cells tend to be less spatially opponent than simple cells.

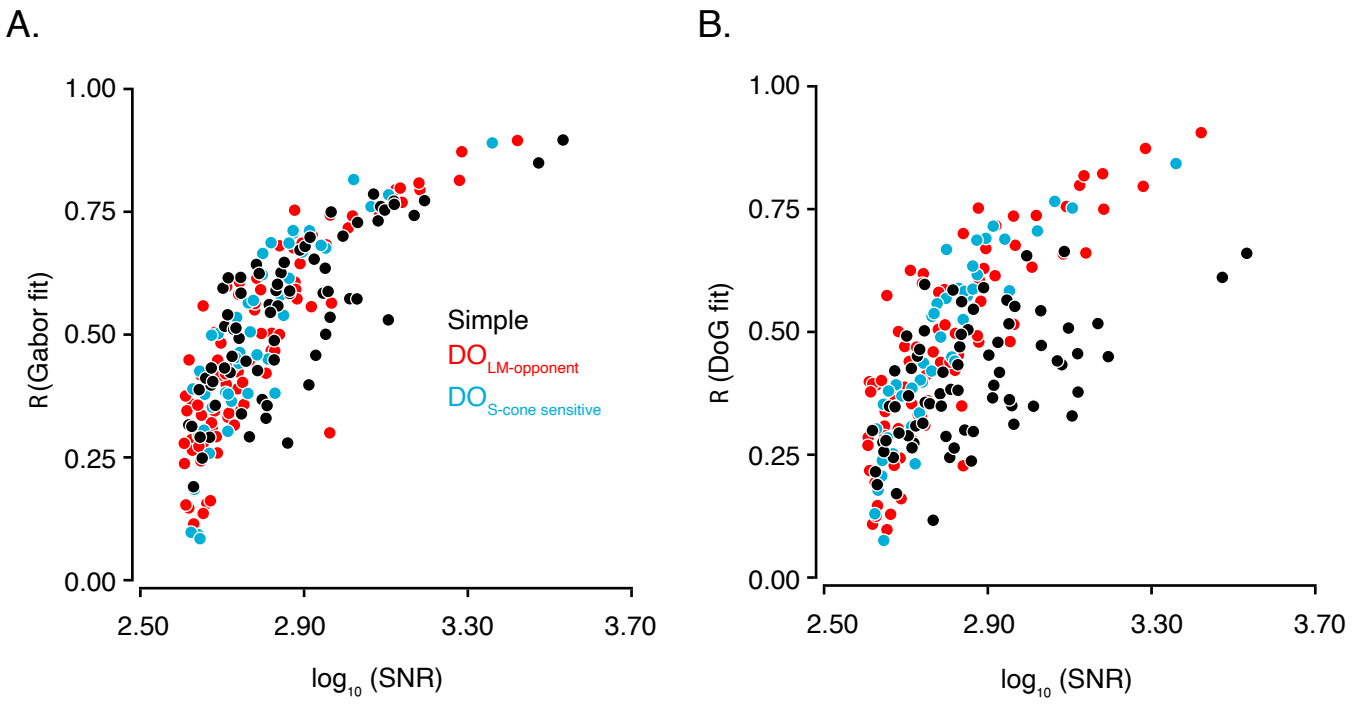

Figure 2.5. Analyses of Gabor and DoG model fits **A.** Scatterplot of cross-validated R of Gabor fits vs. signal-to-noise ratios (SNR) of peak STA frames for simple cells (black), $DO_{LM\text{-}opponent}$ cells (red) and $DO_{S\text{-}cone\ sensitive}$ cells (blue). **B.** Identical to **A** but plotted for DoG fits.

We considered the possibility that the DoG model fit the DO cell data relatively well due to systematic differences in SNR between DO cell STAs and simple cell STAs. For example, a spatial weighting function with low SNR would be fit equally well by a Gabor function as a DoG function even if the true RF organization was a Gabor function. We therefore investigated the relationship between R and the SNR of the peak STA frame for each category of neurons (**see METHODS** *for the definition of SNR*). As SNR increased, so did the goodness-of-fit of the Gabor model, which was similar across the three cell types (p=0.14, Kruskal-Wallis test; **Figure 2.5A**). This result shows that much of the error in the model fits is due to noise in the STAs and not to systematic errors in the Gabor model fits. Extrapolation with a logistic fit predicts that R_{Gabor} would be 0.85

in the limit of infinite SNR. The Gabor model is therefore not simply a better description than the DoG model; it provides accurate response predictions in absolute terms.

A different result was obtained when SNR was compared to the goodness-of-fit of the DoG model. R_{DoG} was lower for simple cells than for DO cells (**Figure 2.5B,** median for simple cells 0.38 vs. median for $DO_{\text{LM-opponent}}$ 0.44 vs. median for $DO_{\text{S-cone sensitive}}$ cells 0.44, p=0.07; Kruskal-Wallis test). This difference is clearest for cells with high SNR ($p<0.0001$, Kruskal-Wallis test on R_{DoG} values for cells with SNRs above the median).

To dissect the differences between simple cell and DO cell RFs more finely, we asked whether simple cell RFs are more frequently odd-symmetric or more elongated than those of DO cells. Either of these properties could degrade the quality of the DoG model fits relative to Gabor fits, because DoG fits are constrained to be even-symmetric and radially symmetric. First, we analyzed the spatial phase of the best-fitting Gabor function, which makes the RF odd-symmetric, even-symmetric, or intermediate (ϕ, **see Methods**). Most simple cells (mean = 57.2°; **Figure 2.6A**) were odd-symmetric, as were most $DO_{\text{LM-opponent}}$ (mean = 52.0°; **Figure 2.6B**) and $DO_{\text{S-cone sensitive}}$ cells (mean = 52.0°; **Figure 2.6C**). The difference in spatial phase did not reach statistical significance, but is in the correct direction to account for the poor DoG model fits to simple cell RFs than DO cell RFs (p=0.35, Kruskal-Wallis test).

Secondly, we analyzed the aspect ratio, which determines how elongated an RF is (γ, **see METHODS**). Aspect ratios were larger for simple cells (median = 1.33; **Figure 2.6D**) than $DO_{\text{LM-opponent}}$ (median = 1.09; **Figure 2.6E**) and $DO_{\text{S-cone sensitive}}$ cells (median

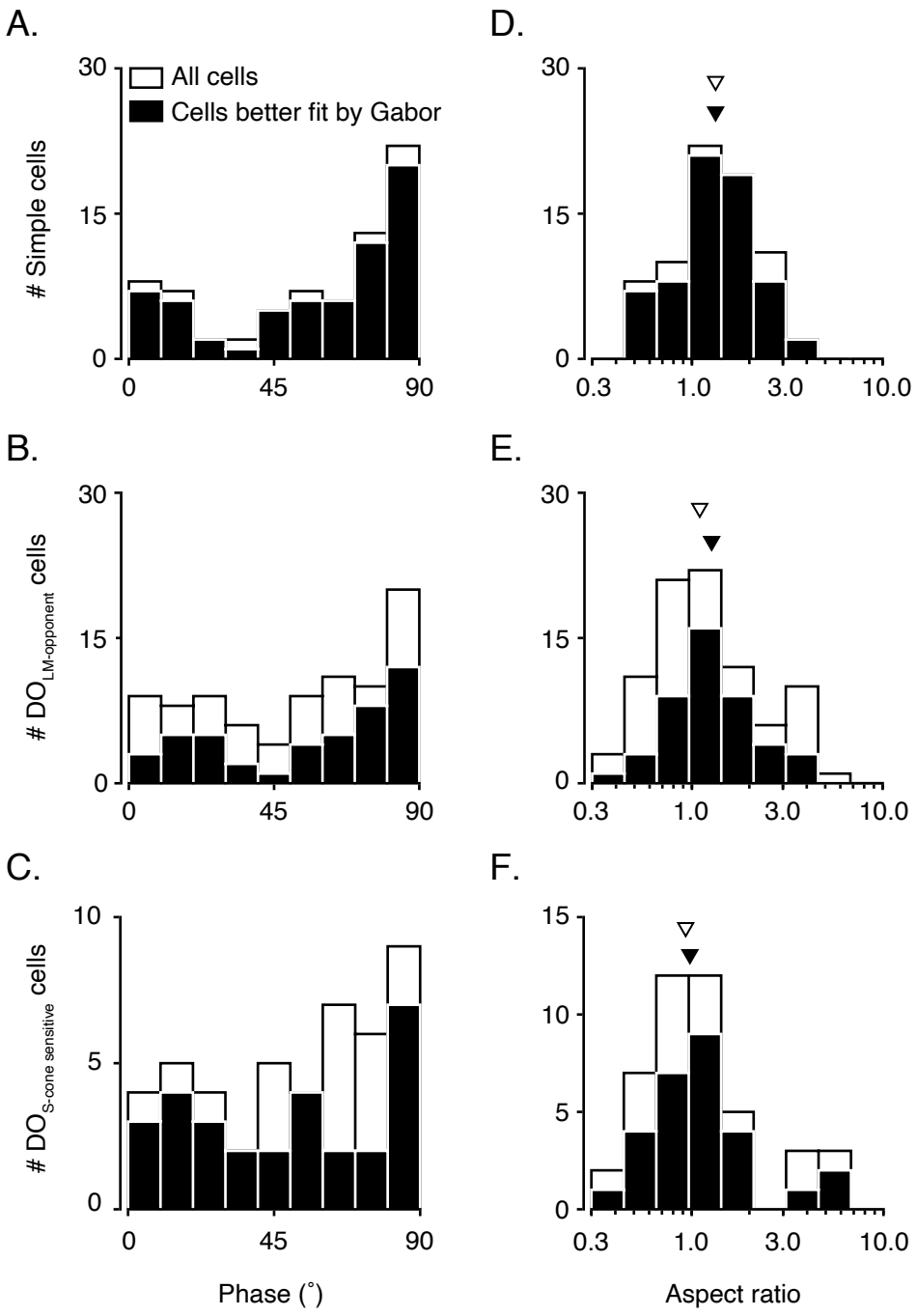

Figure 2.6. Analyses of Gabor model parameters for all cells (white) and cells that are better fit by the Gabor model than the DoG model (black). **A.** Best fitting phase (ϕ) of Gabor fits to simple cell spatial weighting functions. **B & C** Identical to **A** but for $DO_{LM\text{- opponent}}$ cells and $DO_{S\text{-cone sensitive}}$ cells, respectively. **D.** Best fitting aspect ratio (γ) of Gabor fits to simple cell spatial weighting functions. The median is plotted for all simple cell RFs (open triangle) and also for those that were better fit by the Gabor model (closed triangle). **E & F.** Identical to **D** but for $DO_{LM\text{-opponent}}$ cells and $DO_{S\text{-cone sensitive}}$ cells, respectively.

= 0.93; **Figure 2.6F**). The difference in aspect ratio was statistically significant when all cells were considered (p=0.05, Kruskal-Wallis test). Restricting our analyses to cells that

were better fit by a Gabor model ($R_{Gabor} > R_{DoG}$) agreed qualitatively with the above results (**Figure 2.6A–F, black histograms**).

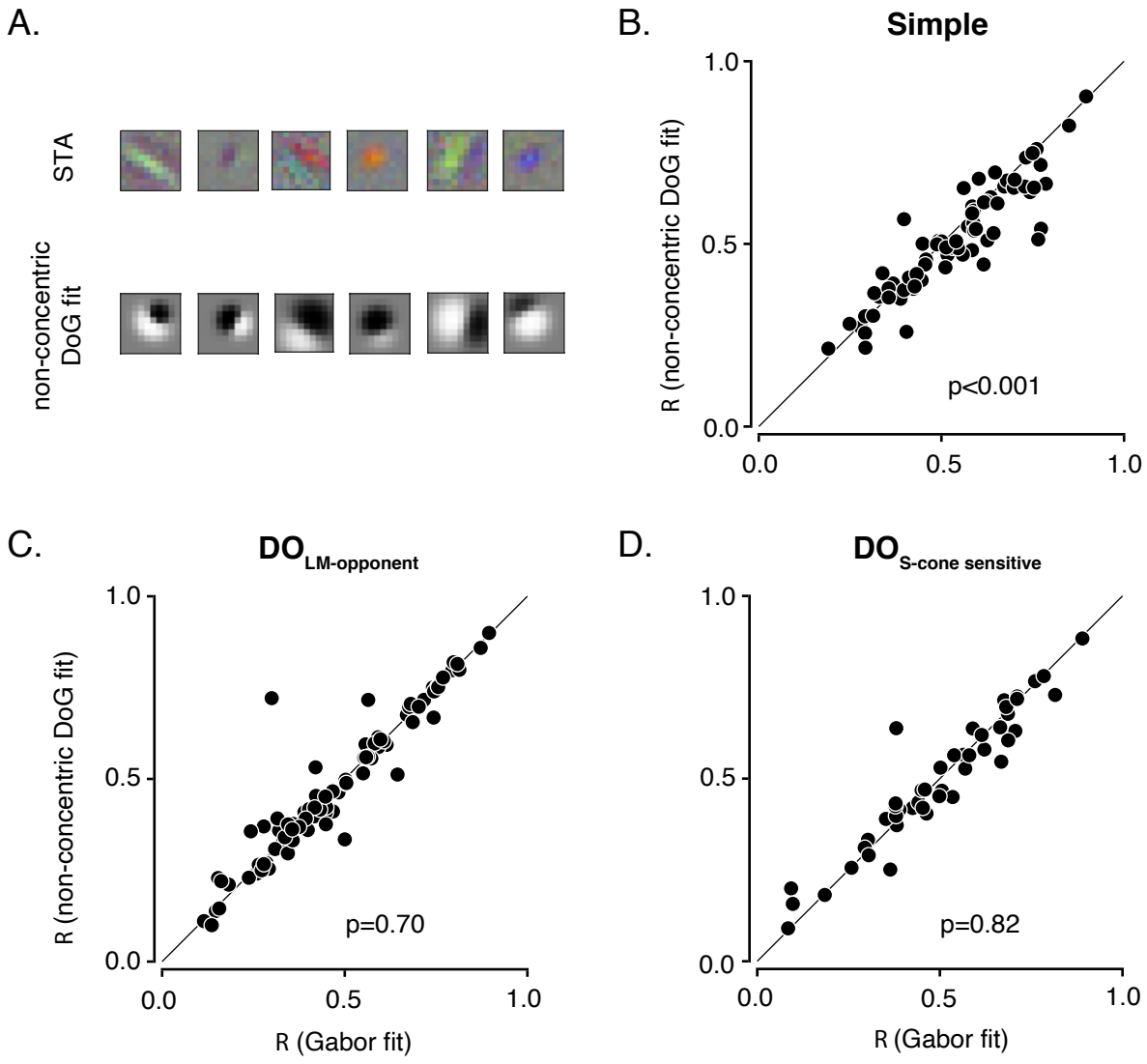

Figure 2.7. Comparison of non-concentric DoG and Gabor model fits **A.** Non-concentric DoG fits to data from the six example cells in **Fig 3.** $R_{\text{non-concentric DoG}}$ = 0.54, 0.66, 0.41, 0.90, 0.60 and 0.78 from left to right. R from Gabor fits are plotted against R from non-concentric DoG fits for simple (**B**), $DO_{\text{LM-opponent}}$ cells (**C**), and $DO_{\text{S-cone sensitive}}$ cells (**D**).

2.4.3 The non-concentric DoG model

The Gabor and DoG models are classic descriptions of DO RFs, but recently a third model was proposed: the center, crescent-shaped surround model (Conway, 2001; Conway and Livingstone, 2006). We formalized this idea by modifying the DoG model to allow the center and surround Gaussians to be non-concentric (Dawis, 1984). This model captures many of the diverse RF structures we observed in our data (**Figure 2.7A**).

We compared the quality of Gabor and non-concentric DoG fits for each cell. Simple cell RFs were better fit by the Gabor model ($p<0.001$; Wilcoxon signed rank test; **Figure 2.7B**) but $DO_{LM\text{-}opponent}$ and $DO_{S\text{-}cone\ sensitive}$ cell RFs were fit similarly by both the models ($p > 0.5$; Wilcoxon signed rank tests; **Figure 2.7B and 2.7D**). These results suggest that the non-concentric DoG model performed similarly to the Gabor model for DO cell RFs but poorly for simple cell RFs.

2.4.4 Analysis of spatial opponency

We considered the possibility that the differences observed between simple and DO cells were caused by weakly DO cells that might not have been classified as DO in other studies or by single-opponent cells that were mis-classified as DO. To address this issue, we computed for each cell a spatial opponency index (SOI) that equals 0 if the RF has a single subregion and 1 if the RF has perfectly balanced subregions. SOIs were greater for simple cells (**Figure 2.8A**; median=0.91) than for $DO_{LM\text{-}opponent}$ cells (**Figure 2.8B**; median=0.72) or $DO_{S\text{-}cone\ sensitive}$ (**Figure 2.8C;** median=0.78) cells

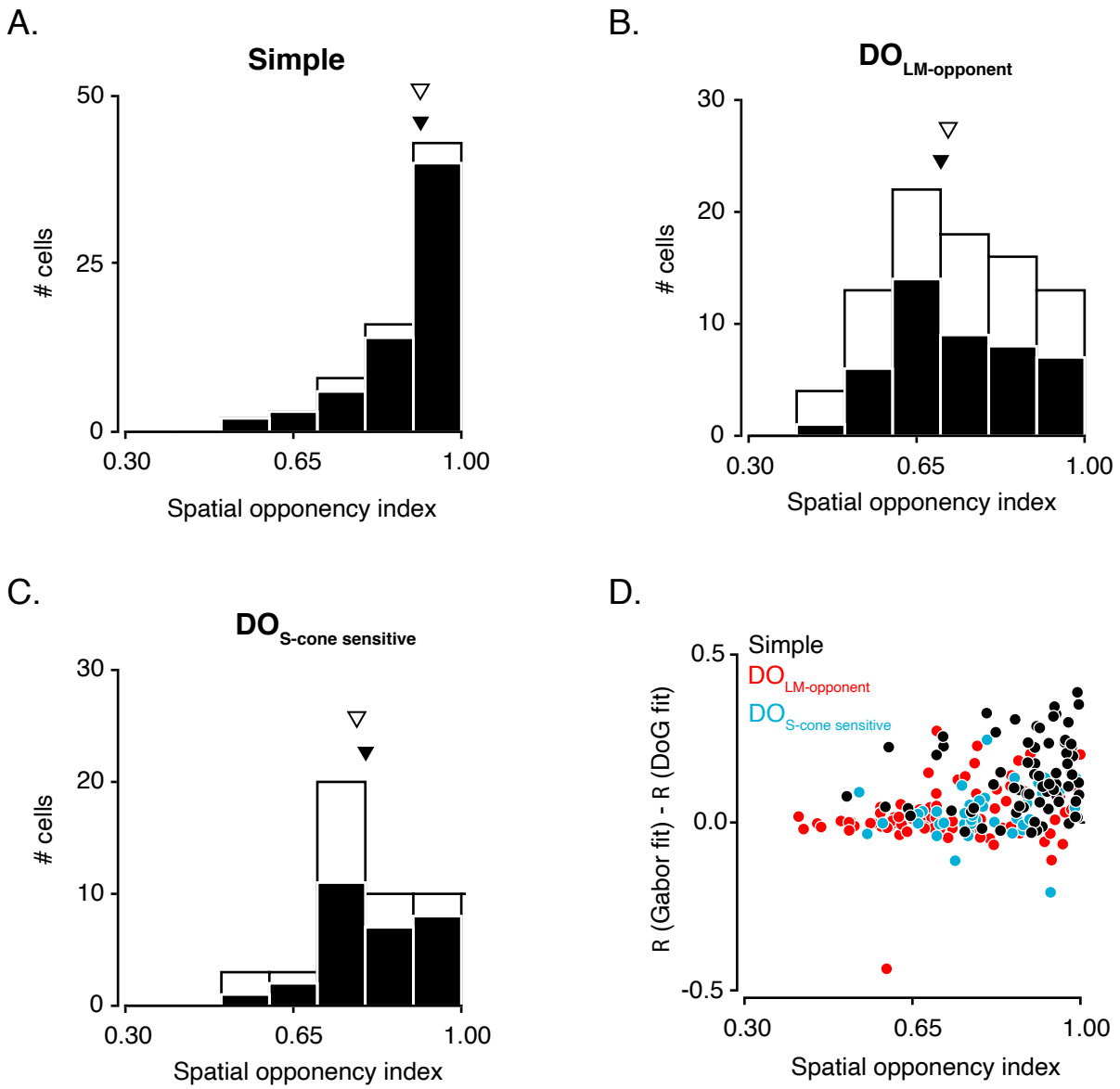

Figure 2.8. Analysis of spatial opponency. **A.** Histogram of spatial opponency indices (SOI) for simple cells. The median SOI is plotted for all simple cell RFs (open triangle) and also of those that were better fit by the Gabor model (filled triangle). **B & C.** Identical to **A** but for $DO_{LM\text{-}opponent}$ cells and $DO_{S\text{-}cone\ sensitive}$ cells, respectively. **D.** Difference in R between Gabor and DoG fits is plotted against the SOI for simple (black), $DO_{LM\text{-}opponent}$ (red) and

(p<0.001, Kruskal-Wallis test). As expected, the SOIs of single-opponent cells were substantially lower than those of DO cells (p<0.001, Mann-Whitney U test; **Figure S2.1**). SOIs of DO cells showed no signs of being a mixture of two discrete types (e.g. single-opponent and true DO cells). We conclude that the RF subregions of DO cells are less well balanced than those of simple cells. Restricting our analyses to cells that were

better fit by a Gabor model (R_{Gabor} > R_{DoG}), or calculating the SOI from the Gabor model fits instead of spatial weighting functions, produced similar results (**Figure S2.2**).

As the SOI increased, so did the difference in goodness-of-fit of the Gabor model and the DoG model (r=0.39, p<0.001, Spearman's correlation between R_{Gabor} - R_{DoG} and SOI; **Figure 2.8D**). This trend was not due to an increase in SNR (r=-0.08, p=0.25, Spearman's correlation between SNR and SOI). The difference between R_{Gabor} and R_{DoG} was larger for simple cells than for DO cells even when analysis was restricted to the subset of cells with strong spatial opponency (p<0.001, Kruskal-Wallis test on R_{Gabor} - R_{DoG} values for cells with SOIs above the median). These results suggest that the superiority of the Gabor fits to simple cell RFs is not simply a consequence of their greater spatial opponency relative to DO cells.

2.5 DISCUSSION

We analyzed the spatial RFs of macaque V1 DO and simple cells with white noise RF mapping, model fitting, and statistical comparisons. To the best of our knowledge, this is the first study to compare DO and simple cell RFs using the same stimulus set. We report four new results. First, the RFs of DO and simple cells were more accurately described by a Gabor model than a DoG model. Second, DO cells tend to have odd-symmetric RFs, similarly to simple cells. Third, the non-concentric DoG model provides a reasonable description of DO cell RFs. Fourth, DO cells have weaker spatial opponency than simple cells. Together, our results show that most DO cells lack a center-surround RF organization, the spatial RFs of simple and DO cells are broadly similar, and a center-crescent surround model describes DO cell RFs nearly as accurately as a Gabor model.

Below, we compare our results to those of previous studies. We then discuss the robustness of our results to the criteria used to categorize cells and the use of R as a measure of goodness-of-fit. Finally, we discuss the potential roles of DO cells in image processing and how our findings have constrained these roles.

2.5.1 Comparison with previous work

Different studies have reached different conclusions about the spatial structure of DO RFs in monkey V1 (Hubel and Wiesel, 1968; Poggio, 1975; Michael, 1978; Livingstone and Hubel, 1984; Conway, 2001; Johnson et al., 2001, 2004; Conway and Livingstone, 2006; Johnson et al., 2008). Early investigations, mostly using circular spots of light were entirely qualitative and reported DO cells to have a concentric center-surround RF

organization (Hubel and Wiesel, 1968; Poggio, 1975; Michael, 1978; Livingstone and Hubel, 1984). Later investigations using sparse noise stimuli measured 2-D RF structure and proposed that DO cell RFs have circular centers and crescent-shaped surrounds (Conway, 2001; Conway and Livingstone, 2006). Parallel investigations using drifting and rapidly flashed sinusoidal gratings concluded that DO cells have Gabor-like RFs largely on the basis of 1-dimensional measurements (orientation-tuning curves) (Johnson et al., 2001, 2004, 2008).

The lack of consensus about DO cell RF structure may reflect biases produced by different stimulus sets and incomplete RF descriptions. Sparse noise stimuli have the advantage of stimulating different parts of the RF independently and thus make no assumptions about the spatial structure of the RF (Conway, 2001; Conway and Livingstone, 2006). However, spiking nonlinearities can prevent simultaneous cone-isolating increments and decrements from cancelling, even outside of the RF, potentially producing an appearance of spatial opponency where none exists (Ben Lankow and Mark Goldman, personal communication).

Sinusoidal gratings are powerful tools for identifying the RF structure of neurons that are well described by a linear model (Movshon et al., 1978a; DeAngelis, 1993; Shapley, 2009). However, many V1 neurons are nonlinear, for example, complex cells. Some studies included complex cells in the population of DO cells (Johnson et al., 2001, 2004, 2008). Complex cells are poorly described by a linear model and do not abide by the definition of double-opponency because they do not have opposite color preferences in different parts of their RFs (Daw, 1968; Livingstone and Hubel, 1984).

We examined the RFs of simple cells and DO cells with the same stimuli and data analyses. We used a stimulus that provides unbiased STA measurements, and we excluded complex cells from our analyses (Chichilnisky, 2001). We found that simple cell RFs are better fit by the Gabor model than by the DoG model or the non-concentric DoG model, consistent with previous studies (Ringach, 2002b). Most simple cells had odd-symmetric RFs, a result that is also consistent with a previous report (Ringach, 2002a). A novel contribution of the current study is the extension of this result to DO cells. The results of the current study are consistent with the existence of odd-symmetric, chromatic edge detectors in the primate visual system that was predicted on the basis of psychophysical experiments (Bradley, 1988; Girard, 1995; McIlhagga, 2018).

2.5.2 Effects of cell categorization criteria

We distinguished simple cells from DO cells based on cone weights. We applied a stricter criterion to L- and M-cone weights to categorize a cell as simple than as $DO_{LM\text{-}opponent}$—a fact that is visible from the greater spread of L- and M-cone weights for simple cells than $DO_{LM\text{-}opponent}$ cells (**Figure 2.2**). The rationale for this decision is the greater variability in estimated cone weights for non-opponent cells (Horwitz et al., 2007). Nevertheless, our results are robust to this decision. We recategorized the cells into $DO_{LM\text{-}opponent}$ and simple categories with reversed criteria (**see Methods** for the original criteria) and obtained similar results to those shown in the main text (**Figure S2.3–2.4**).

2.5.3 Alternative metrics for model comparison

We compared models using cross-validated correlation between data and model fits, but our results are robust to this choice. We repeated the model comparisons using the Bayesian Information Criterion, cross-validated sum of squared errors and cross-validated prediction of spike-triggering stimuli. The results from these analyses agreed qualitatively with our main conclusions; RFs of DO and simple cells were more accurately described by a Gabor model than a DoG model (**Figure S2.5**), and the non-concentric DoG model provided a reasonable description of DO cell RFs but not simple cell RFs (**Figure S2.6**).

2.5.4 Role of DO cells in image processing

At least some DO cells carry information about the phase and orientation of local chromatic variations. This information may be useful for at least two visual computations. First, DO cells might aid in shape-from-shading. Extraction of chromatic orientation flows in 2-D images is critical for accurate perception of 3-D shapes (Kingdom, 2003; Zaidi, 2006; Kunsberg, 2018). In some displays, alignment of chromatic and luminance edges suppresses the percept of 3-D form whereas misalignment enhances the 3-D percept (Kingdom, 2003). Signals from DO cells may therefore be integrated with those from simple cells to infer 3-D structure from 2-D retinal images. Second, DO cells might aid in inferring whether an edge in a visual scene is caused by the same material under different lighting conditions or by two different materials under the same lighting condition. An edge between two pieces of a single material under direct illumination and in shadow creates a nearly pure intensity difference. On the contrary, an edge between two different materials under the same

illumination creates spatially coincident intensity and spectral variations. The presence or absence of a spectral variation could serve as an important cue to the visual system for disambiguating material edges from illumination edges (Cavanagh, 1991; Fine, 2003; Tappen, 2003; Olmos, 2004). The similarity of RF structure between simple cells and DO cells might facilitate downstream integration of their responses.

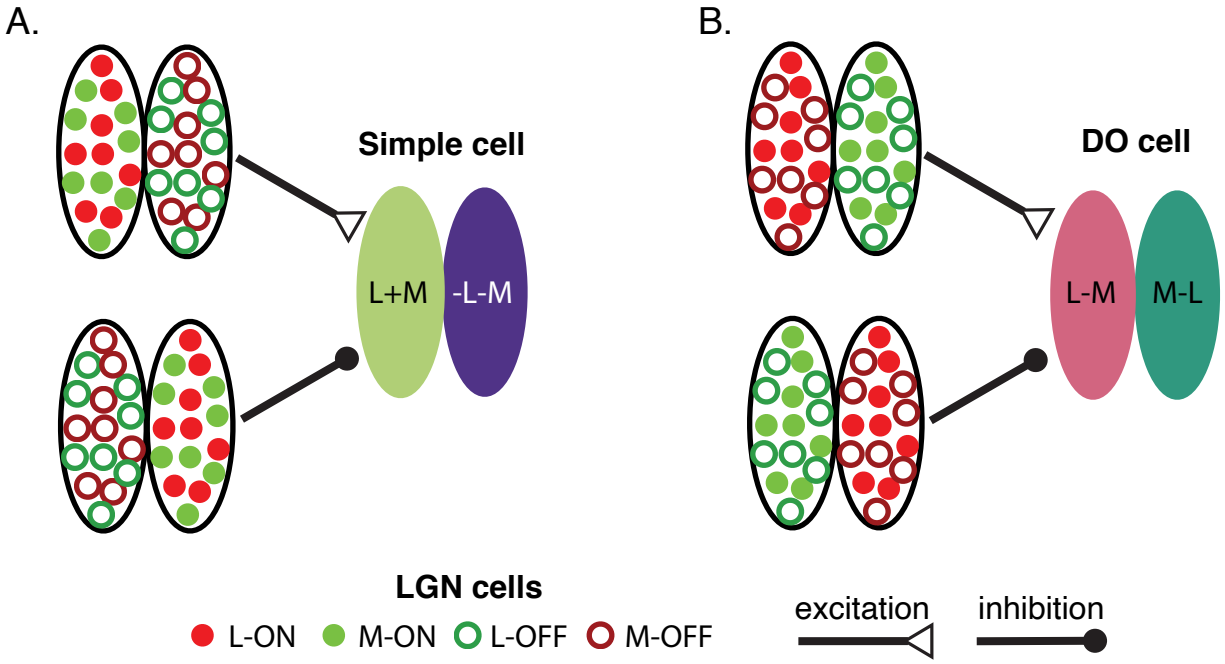

Figure 2.9. Schematic diagram of the circuitry proposed to underlie simple cell and DO cell RFs. **A.** A simple cell RF constructed from parvocellular LGN afferents. The ON subregion (L+M) is excited by L-ON and M-ON LGN cells and is inhibited by L-OFF and M-OFF LGN cells. Similarly, the OFF subregion (-L-M) is excited by L-OFF and M-OFF LGN cells and is inhibited by L-ON and M-ON LGN cells. **B.** Construction of a DO cell RF using the same set of parvocellular LGN cells that provide input to a simple cell. The L-M subregion is excited by L-ON and M-OFF LGN cells and is inhibited by L-OFF and M-ON LGN cells whereas the M-L subregion is excited by L-OFF and M-ON LGN cells and is inhibited by L-ON and M-OFF LGN cells.

2.5.5 Are DO cells cone-opponent simple cells?

DO and simple cell RFs differ in detail but are similar in many ways. This similarity motivates the hypothesis that the primary difference between these two cell types is the

sign of input they receive (indirectly) from the three cone photoreceptor classes. Indeed, the models proposed to underlie simple cell RFs can also be applied to DO cells with only a minor change in the wiring (**Figure 2.9**).

A hallmark of simple cells is spatial linearity, a property mediated in part by push-pull excitation and inhibition (Ferster, 1988; Tolhurst, 1990; Hirsch, 1998; Ferster, 2000). Some DO cells exhibit push-pull responses, consistent with the proposed similarly between them and simple cells (Conway 2006). However, whether the departures from linearity observed in some DO cells exceeds expectations provided by the benchmark of simple cells is unclear. To answer this question, a useful next step would be to compare quantitatively the degree of spatial linearity between DO and simple cells.

2.6 SUPPLEMENTARY FIGURES

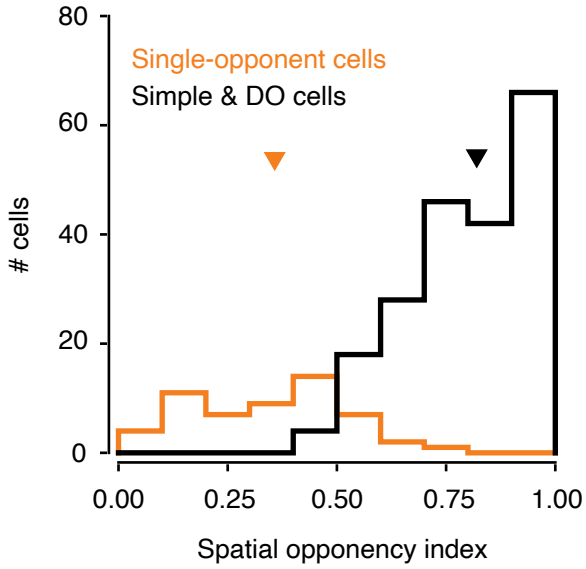

Figure S2.1. Comparison of spatial opponency indices (SOIs) between single-opponent cells (orange) and pooled simple and DO cells (black). The median SOI of simple and DO cells combined is 0.82 (black triangle) and that of single-opponent cells is 0.36 (orange triangle).

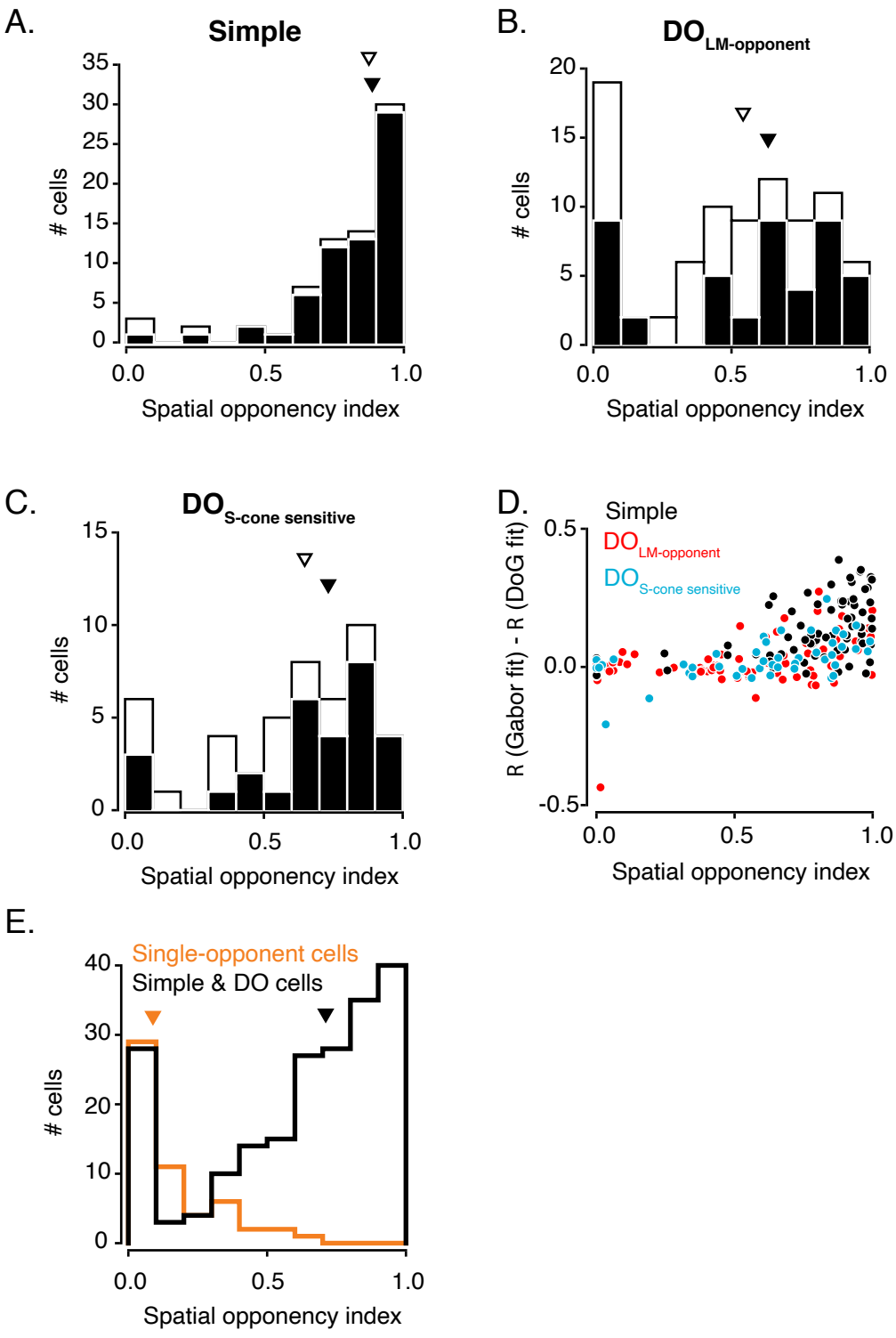

Figure S2.2. Analysis of spatial opponency indices (SOIs) calculated from the best fitting Gabor functions. **A.** Histogram of SOIs for simple cells. The median SOI is plotted for all Gabor fits (open triangle) and also for cells better fit by the Gabor model (filled triangle). **B & C.** Identical to **A** but for $DO_{LM\text{-}opponent}$ cells and $DO_{S\text{-}cone\ sensitive}$ cells, respectively. **D.** Difference in R between Gabor and DoG fits is plotted against the SOI for simple (black), $DO_{LM\text{-}opponent}$ (red) and $DO_{S\text{-}cone\ sensitive}$ (blue) cells. **E.** Comparison of SOIs from simple and DO cells, pooled (black),

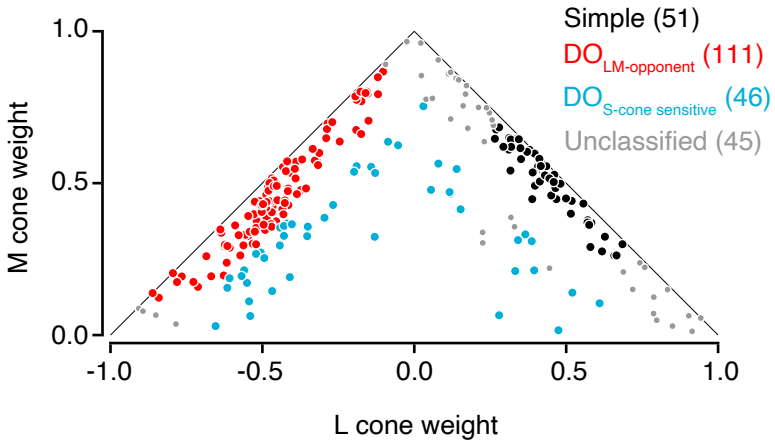

Figure S2.3. Reclassification of cells with reversed cone weight criteria. Shown are the normalized cone weights of simple (black), $DO_{LM\text{-}opponent}$ (red), $DO_{S\text{-}cone\ sensitive}$ (blue) and unclassified (gray) cells. Under these criteria, cells were classified as simple if the L- and M-cone weights had the same sign, that together, accounted for 80% of the total cone weight and individually accounted for at least 30%. Cells were labeled as $DO_{LM\text{-}\ opponent}$ if the L- and M-cone weights had opposite sign, together accounted for 80% and individually accounted for at least 10% of the total cone weight. Classification of $DO_{S\text{-}\ cone\ sensitive}$ cells was unchanged from the description in the Methods.

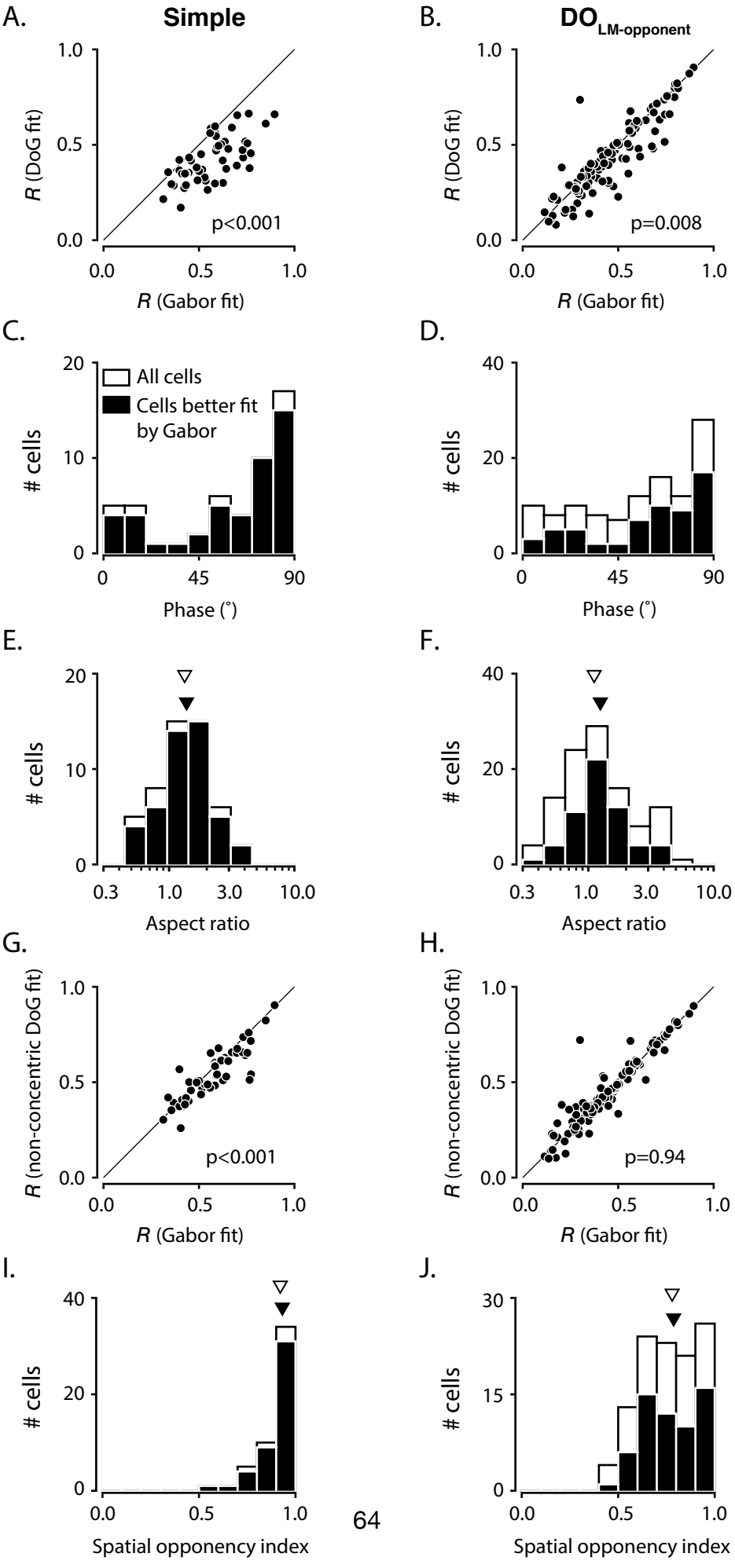
A.
Simple
B.
DO LM-opponent
R (DoG fit)
R (Gabor fit)
p<0.001
p=0.008
C.
D.
All cells
Cells better fit by Gabor
cells
Phase (°)
E.
F.
Aspect ratio
G.
H.
R (non-concentric DoG fit)
p<0.001
p=0.94
I.
J.
Spatial opponency index

Figure S2.4. Model comparisons and spatial opponency analyses after reclassification of cells. **A.** Cross-validated R is plotted from Gabor fits and from DoG fits for simple cells. **B.** Identical to **A** but for $DO_{LM\text{-}opponent}$ cells. **C.** Analyses of best fitting phase (ϕ) of Gabor fits to all simple RFs (white) and those that are better fit by the Gabor model than the DoG model (black). **D.** Identical to **C** but for $DO_{LM\text{-}opponent}$ RFs. **E.** Analysis of best fitting aspect ratio (γ) of Gabor fits to all simple RFs (white) and those that are better fit by the Gabor model than the DoG model (black). The median γ is plotted for all simple cell RFs (open triangle) and also for cells better fit by Gabor model (closed triangle). **F.** Identical to **E** but for DO RFs. **G.** Cross-validated R is plotted from Gabor fits and from non-concentric DoG fits for simple cells. **H.** Identical to **G** but for $DO_{LM\text{-}opponent}$ cells. **I.** Histogram of spatial opponency indices (SOIs) for simple cells based on spatial weighting functions. **J.** Identical to **I** but for $DO_{LM\text{-}opponent}$ cells.

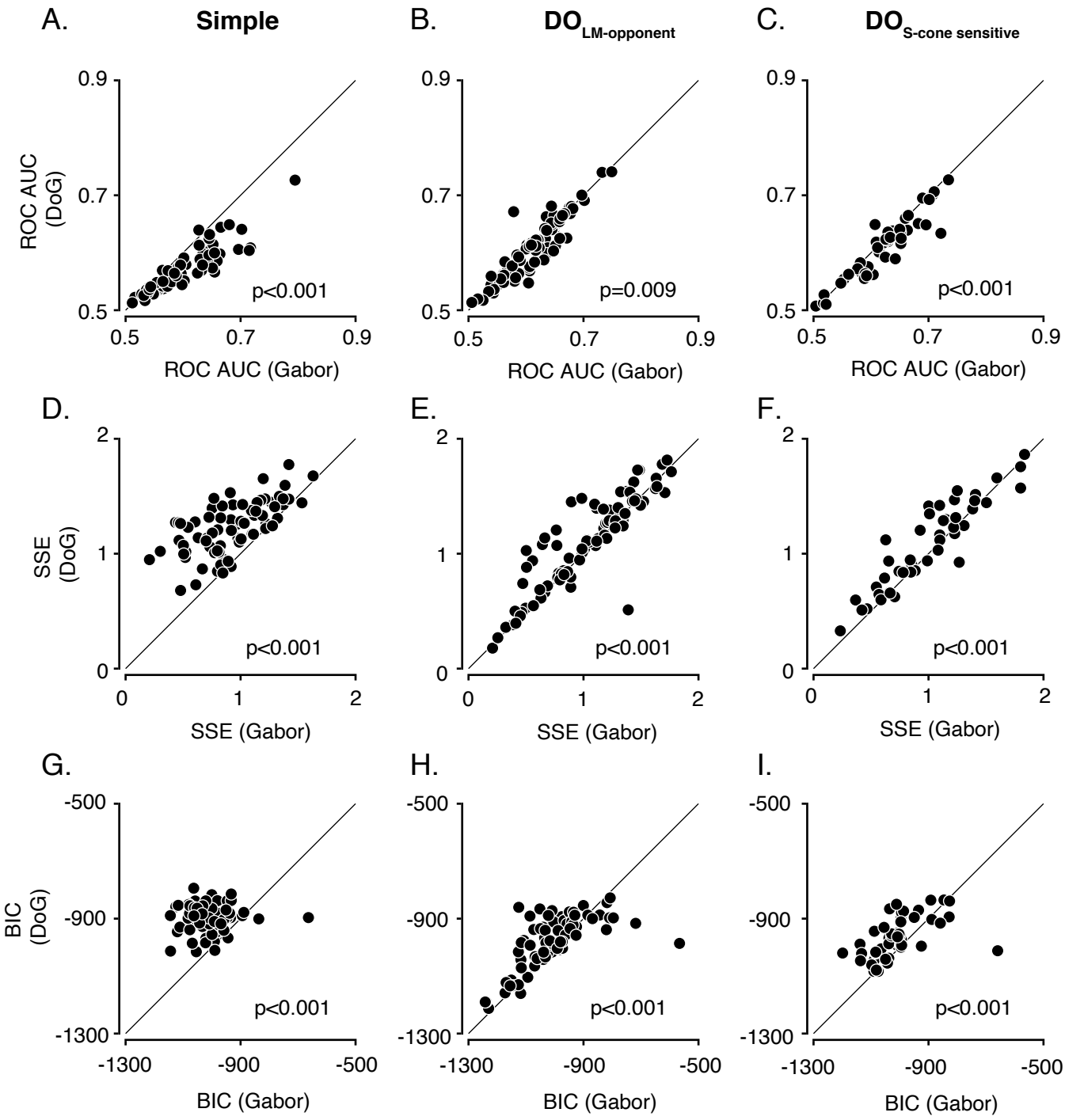

Figure S2.5. Comparison of Gabor and DoG model fits using three different analyses. **A.** Cross-validated prediction of spike-triggered stimuli using the area under receiver operating characteristics (ROC AUC) is plotted from Gabor fits and from DoG fits for simple cells. **B.** Identical to **A.** but for $DO_{LM\text{-}opponent}$ cells **C.** Identical to **A.** but for $DO_{S\text{-}cone\ sensitive}$ cells. **D.** Cross-validated sum of squared errors (SSE) is plotted from Gabor fits and from DoG fits for simple cells. **E.** Identical to **D.** but for $DO_{LM\text{-}opponent}$ cells. **F.** Identical to **D.** but for $DO_{S\text{-}cone\ sensitive}$ cells. **G.** Bayesian Information Criterion (BIC) is plotted from Gabor fits and from DoG fits for simple cells. A better model fit yields a lower BIC. **H.** Identical to **G.** but for $DO_{LM\text{-}opponent}$ cells. **I.** Identical to **G.** but for $DO_{S\text{-}cone\ sensitive}$ cells.

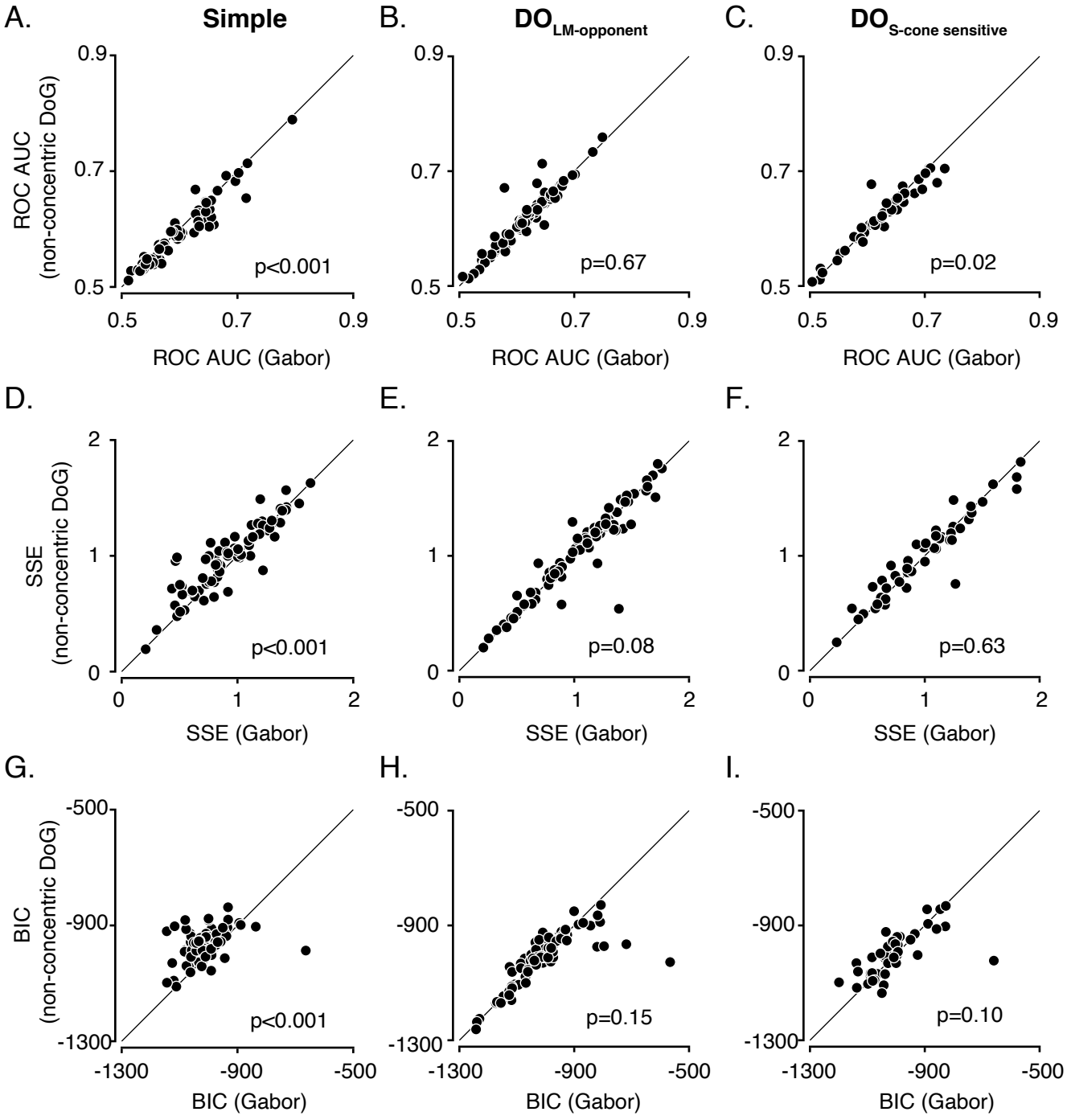

Figure S2.6. Comparison of Gabor and non-concentric DoG model fits using three different analyses. **A.** Cross-validated prediction of spike triggered stimuli using the area under receiver operating characteristics (ROC AUC) is plotted from Gabor fits and from non-concentric DoG fits for simple cells. **B.** Identical to **A.** but for $DO_{LM\text{-}opponent}$ cells. **C.** Identical to **A.** but for $DO_{S\text{-}cone\ sensitive}$ cells. **D.** Cross-validated sum of squared errors (SSE) is plotted from Gabor fits and from non-concentric DoG fits for simple cells. **E.** Identical to **D.** but for $DO_{LM\text{-}opponent}$ cells. **F.** Identical to **D.** but for $DO_{S\text{-}cone\ sensitive}$ cells. **G.** Bayesian Information Criterion (BIC) is plotted from Gabor fits and from non-concentric DoG fits for simple cells. A better model fit yields a lower BIC. **H.** Identical to **G.** but for $DO_{LM\text{-}opponent}$ cells. **I.** Identical to **G.** but for $DO_{S\text{-}cone\ sensitive}$ cells.

3. SPATIAL INTEGRATION BY DOUBLE-OPPONENT AND SIMPLE CELLS IN MACAQUE PRIMARY VISUAL CORTEX

3.1 ABSTRACT

Luminance and chromatic edges in visual scenes contain information about the locations and shapes of objects. These edges are extracted in area V1 of the primate cortex by simple and double-opponent (DO) cells. Simple cells integrate ON and OFF luminance signals roughly linearly across their spatial receptive fields (RF). DO cells are spatially opponent, like simple cells are, but are also cone-opponent. Previously, we showed that simple cells and DO cells have similar spatial RF structures. Here, we ask whether they integrate information across their spatial RFs similarly. To determine whether or not this is true, we used a combination of white noise and closed-loop stimulus generation techniques to identify edges that drove identical spike count responses from individual DO cells but varied in color. We found that many DO cells responded to chromatic contrast across an edge linearly, similar to how simple cells respond to luminance contrast. The spatial linearity of both simple and DO cells is explained by a push-pull (excitation-inhibition) model in which the same set of LGN afferents but with different wirings drive these cell types. We propose that DO cells could be the cone-opponent homologues of simple cells. Nonlinear spatial integration was prevalent among cells that were neither simple nor DO. Further analysis revealed that the signal integration was more nonlinear within individual parts of the RF of these other neurons than the DO and simple cells, thus rejecting a broad class of models

under which other V1 neurons nonlinearly combine inputs from two linear non-overlapping RF subregions.

3.2 INTRODUCTION

Edges are informative about the identity and location of objects in natural scenes. The simple and double-opponent (DO) cells in the primary visual cortex (V1) of macaque monkeys are well suited for extracting edges because of their Gabor-like RF structure (Ringach, 2002a; Johnson et al., 2008; De, 2020). Simple cells respond strongly to oriented luminance edges. They integrate ON and OFF luminance signals roughly linearly across their receptive fields (RF) and are thought to contribute to the phase-invariant representation of orientation established by complex cells (Movshon et al., 1978b, a; DeAngelis, 2004). DO cells are spatially opponent, like simple cells are, but are also cone-opponent and, therefore strongly respond to oriented chromatic edges. How DO cells integrate signals across their RFs is not well understood.

The spatial integration of DO cells has been inferred indirectly from the push-pull responses—indicative of linear integration (Ferster, 1988; Hirsch, 1998; Ferster, 2000). A cell is said to display a push-pull response if it evokes an ON response to light of one chromaticity and an OFF response to a light of opposite chromaticity in the same part of the RF (Hirsch, 1998). At least some DO cells displayed push-pull responses (Conway and Livingstone, 2006). The push-pull responses were assessed by plotting the degree of excitation versus suppression to ON and OFF cone-isolating punctate flashes onto individual parts of the RF. Because the suppression of spiking activity is difficult to observe with extracellular recordings when the baseline firing rate is low, the study assumed that the rebound response immediately after the stimulus offset was equivalent to the OFF response during the stimulus presentation period. Such an

assumption may be confounded by the spiking non-linearity that might dominate the stimulus-response relationship and complicate the interpretation of data. A conclusive report of the spatial integration by DO cells is not yet available.

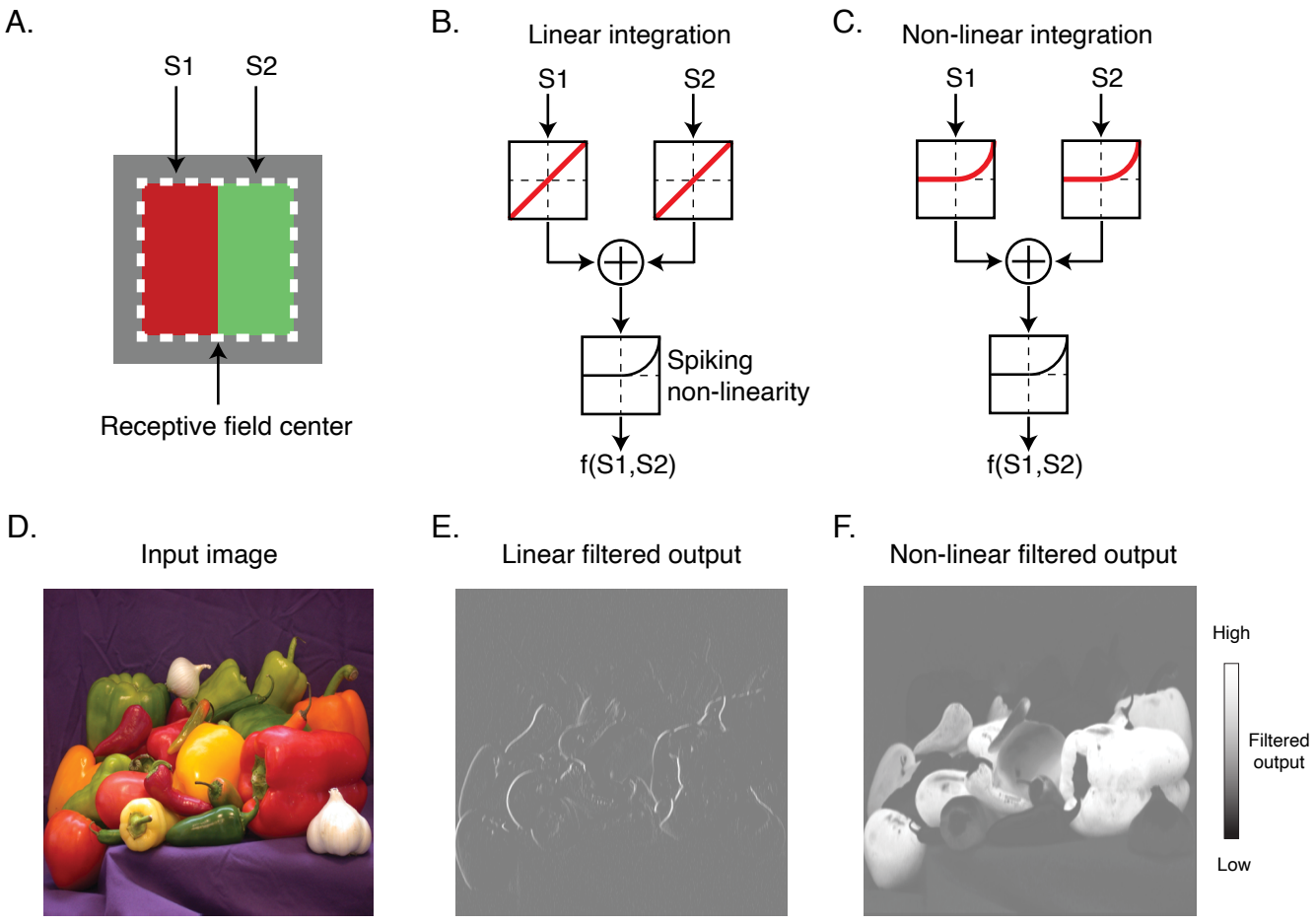

Figure 3.1. Impact of linear and non-linear spatial filtering on image processing. **A.** Receptive field structure of a hypothetical V1 DO cell with an ON (increment in red and decrement in green) and an OFF (decrement in red and increment in green) subunit. The input S1 and S2 correspond to stimulus contrast on the two sides of a vertical edge. **B.** A linear spatial filter that sums the input to each of the subunits and generates a response f(S1,S2) via a rectified spiking non-linearity. Note that the drive from each of the subunits are combined linearly before being transformed by the spiking non-linearity. **C.** A non-linear spatial filter that transforms each subunit input using a threshold quadratic non-linearity. Note that the signals have already been transformed non-linearly prior to the spiking non-linearity. **D.** An example natural image. **E.** Output of the linear spatial filter of the input image. **F.** Same as **(E)** but for the non-linear spatial filter.

Knowing how DO cells integrate signals across their RFs has important implications for understanding the role these cells play in image processing (**Figure 3.1)**. For example, consider a hypothetical V1 cell that is sensitive to a chromatic edge (**Figure 3.1A**). If this cell integrates signals across space linearly, then it is well suited for extracting vertical chromatic edges from scenes (**Figure 3.1B,C,E**). Such a computation could be useful for maintaining a constant representation of edges regardless of relative changes in the position of the light source and the observer (Gegenfurtner, 2003; Gao et al., 2013; Johnson, 2016). Now, consider a specific example of a non-linear integration in which a cell sums the rectified-squared signals across the two linear spatial regions. This non-linear filtering is well suited for extracting both edges and surfaces (**Figure 3.1C,F**). Such a non-linear computation could be useful for processing textures or jointly processing first- and second-order forms (Koenderink, 2003; Landy, 2004; El-Shamayleh and Movshon, 2011; Hallum, 2014; Zhang, 2017). Note that such a non-linear filtering could be achieved by recruiting multiple spatial linear filters that are sensitive to a variety of spatial frequencies as well, but not by a single linear filter alone.

Motivated to understand the role of DO cells in image processing, we investigated how DO cells integrate chromatic signals across space. We stimulated every neuron we studied with the same white noise stimulus to maintain a state of constant adaptation across experiments. Using spike triggered averaging, we determined whether the cells were DO, simple or neither, and identified their spatial RF structure. We then presented a battery of edges to each cell that matched the spatial structure of its RF. Using a closed-loop staircase technique, we identified edges that drove identical spike count

responses but varied in color. We analyzed the collection of edges and assessed the linearity of spatial integration using quantitive model comparisons.

We found that many DO cells responded to the arithmetic differences in color, across an edge, similar to how simple cells respond to luminance edges. This similarity of spatial integration is explained by a push-pull (excitation-inhibition) model in which the RFs of simple cells and DO cells can be constructed from the same set of LGN afferents but with a minor change to the wiring. We propose that DO cells are cone-opponent homologues of simple cells, and they could be the basis of chromatic sensitivity of the downstream color-sensitive V1 complex cells (Gouras, 1979; Shapley, 2011; Rentzeperis, 2014).

We also studied neurons that were neither DO nor simple, and found that they integrated signals across space mostly non-linearly. We hypothesized that these neurons integrate signals non-linearly across their linear RF subregions. Analysis of signal integration within individual non-overlapping RF subregions revealed that the signals were integrated more non-linearly in these other neurons than DO and simple cells. This result thus rejects a broad class of models under which other V1 neurons nonlinearly combine inputs from their linear RF subregions.

3.3 METHODS

3.3.1 General

All the protocols conformed to the guidelines provided by the US National Institutes of Health and the University of Washington Animal Care and Use Committee. Data were collected and analyzed for two adult male rhesus macaques (Macaca mulatta). Each monkey was surgically implanted with a titanium headpost and a recording chamber (Crist Instruments) over area V1. Eye position was continuously monitored using either an implanted monocular scleral search coil or a digital eye-tracking system (SMI iView X Hi-Speed Primate, SensoMotoric Instruments).

3.3.2 Task

The monkeys sat in a primate chair 1 m from a cathode ray tube (CRT) monitor in a dark room during the experiments. In a subset of sessions, the distance was reduced to 0.7 m and the pixel size was changed accordingly to preserve the subtended DVA. During the white noise presentation, the monkeys were trained to fixate a centrally located dot measuring 0.2 x 0.2° and maintain their gaze within a 1.6 x 1.6° fixation window. During the closed-loop isoresponse measurements, the monkeys had to maintain their gaze within a 0.8 x 0.8° window. Successful fixation was rewarded with apple juice and any fixation breaks resulted in the stimulus to disappear, reward to stop and trial to abort.

3.3.3 Monitor calibration

Monitor calibration routines were adapted from those included in Matlab Psychophysics toolbox. Emission and voltage-intensity relationships of each monitor phosphor were calibrated using a spectroradiometer (PR650, PhotoResearch). The color resolution of each channel was increased from 8 to 14 bits using a Bits++ video signal processor (Cambridge Research) at the expense of decrement of spatial resolution; each pixel was twice as wide as it was tall. The monitor refresh rate was fixed to 75 Hz and background color was set to uniform gray (x = 0.3, y = 0.3, Y = 43–83 cd/m^2).

3.3.4 Electrophysiological recordings

We recorded from well isolated V1 neurons using an extracellular tungsten microelectrode (Frederick Haer, Brunswick, ME) that was lowered through dura mater via a hydraulic microdrive (Steolting Co.). Electrical signals were amplified and digitized at 40 kHz online (Plexon) and stored in a PC. Electrode impedances were at 1–4 MΩ at 1 kHz.

After isolating a spike waveform, we mapped the RF boundaries with oriented bars and roughly estimated the location of neuronal RF.

3.3.5 Experimental Protocol

We rigorously characterized the spatial and chromatic sensitivity of the RF, and measured integration of signals across two non-overlapping regions of RF that had different chromatic preferences. We divided our experiment into three sequential

phases, the first two, to characterize the RF, and the third, to measure the interaction of signals across non-overlapping parts of the RF.

During the first phase, we estimated the spatiochromatic RF by presenting white noise stimuli to the RF and performing spike-triggered averaging. During the second phase, we refined our characterization of the spatiochromatic RF by customizing a stimulus that provided greater effective contrast and better estimated the chromaticity of the preferred light in different parts of the RF. These two phases of experiments, together accurately characterized the spatiochromatic RF. During the third phase, we measured the interaction of the preferred light signals across neighboring RF regions that were sensitive to lights of different chromaticities. We describe each of these phases in detail below.

Phase 1: Checkerboard white noise

We presented a randomly flickering chromatic checkerboard stimuli (**Figure 3.2A**) onto the estimated neuronal RF (Horwitz et al., 2005, 2007). Each stimulus frame was a grid of 10 x 10 pixels, with each pixel subtending 0.2 x 0.2°. The stimulus changed every 13.33 ms. The color of each pixel was determined by the red, green and blue phosphor gun intensities. The intensity of each phosphor gun was modulated independently according to a Gaussian distribution with a standard deviation of 15% of the physically achievable range. The space-time averaged intensity of each phosphor was equal to its contribution to the background.

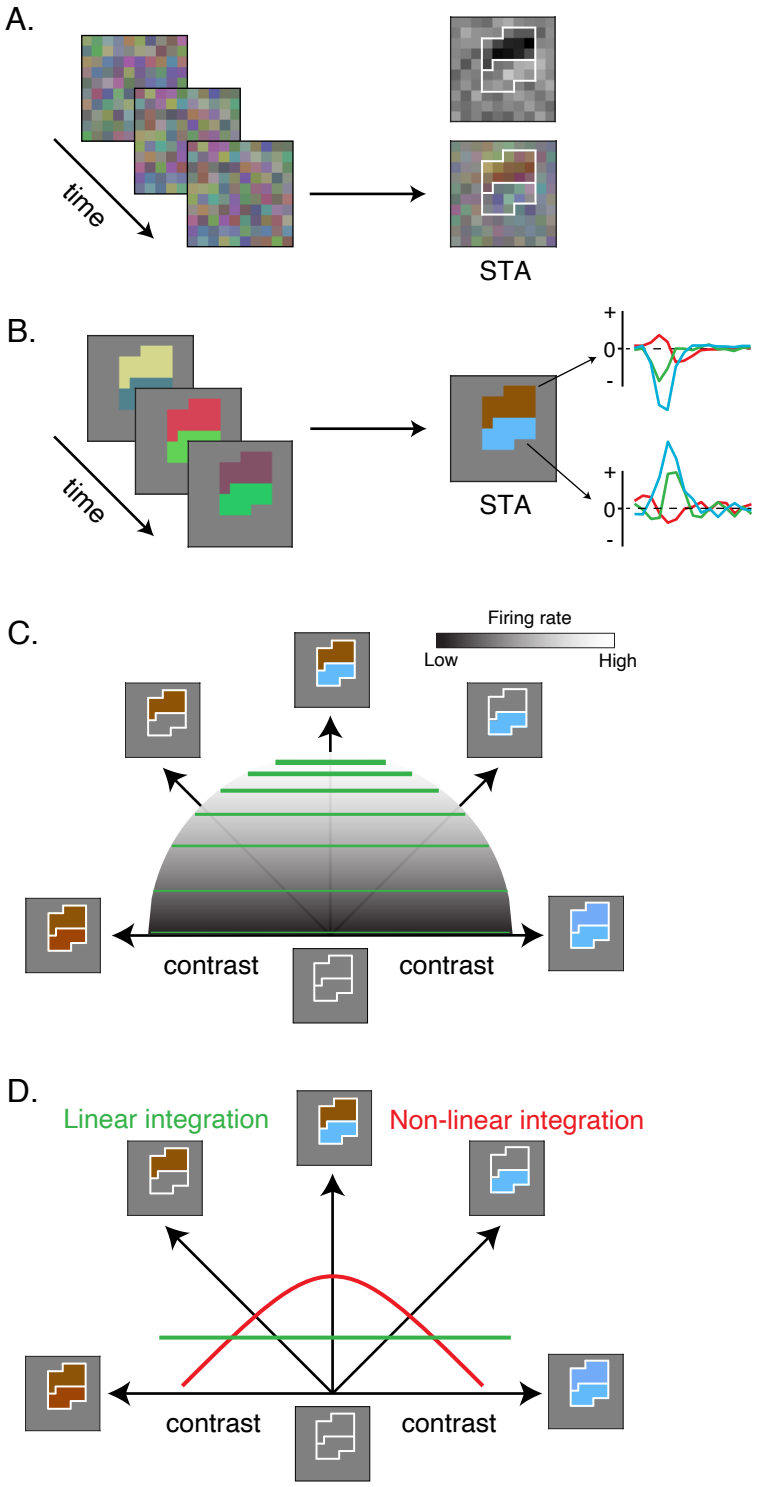

Figure 3.2. Experimental protocol **A.** Visual stimulus during phase 1 of the experiment. The visual stimulus was 10x10 grid of 0.2x0.2˚ squares, the colors of which randomly changed every 13.33 ms. Spike trigerred averaging (STA) reveals the average preferred stimulus by the neuron. The grayscale spatial RF reveals two neighboring sets of pixels with similar chromatic content. Each set of pixels was yoked to create a custom white noise stimulus. **B.** The customized whitenoise stimulus that modulated non-overlapping regions of the RF independently. The RF regions have opposite chromatic preferences as revealed by the 15 (frames) x 3 (color) temporal-chromatic STA. **C.** Neuronal responses from a hypothetical neuron that integrates signals between the two non-overlapping regions linearly. The spiking non-linearity affects the spacing between the lines, but does not bend them. The stimulus contrast space was created by linearly combining the preferred colors within the non-overlapping regions in different proportions. Stimulus contrast increases radially. **D.** A closed-loop staircase procedure identified points that lie on or near an isoresponse curve. Shown are the isoreponse predictions for a linear (green) and a non-linear (red) spatial integration.

Neuronal responses to the white noise stimuli were analyzed using spike triggered averaging (STA) (**Figure 3.2A**) (Horwitz et al., 2005). In this analysis, a set of 10 frames preceding every spike was collected and averaged. This analysis revealed the average preferred light by the neuron within the RF at every time frame.

We selected the STA frame that differed most from the background, based on the sum of squared red, green, and blue pixel intensities (negative intensities were defined as those below the contribution to the background), and identified pixels within the STA frame that had high signal than noise, computed separately for each phosphor gun ($p<0.05$, z-test). This approach identified pixel locations that were strongly modulated by individual phosphors, and provided a rough map of the spatial RF by revealing non-overlapping subregions with similar chromatic preferences among the pixels enclosed by each subregion (**Figure 3.2A**). We refer to each of these distinct non-overlapping RF subregions as “subunits” throughout the manuscript.

Some STAs have little spatial structure in the sense that all pixels inside the RF reveal the same average preferred chromaticity. Other STAs have more elaborate spatial structure, for example, being composed of a set of cyan pixels and a separate set of red pixels (**Figure 3.2A**). We assume that these pixels are part of a single, homogeneous RF subunit.

The spatial structure and chromaticity of individual pixels within a subunit may appear noisy because of the lower effective contrast provided by the white noise checkerboard stimulus (**Figure S3.1A–B**). Because the phosphor intensities of two neighboring pixels are uncorrelated, the effective contrast is lower if a neuron were to integrate signals

across pixels. This problem can be solved, at least in part, by stimulating all the pixels within each subunit with the same light. Such an approach will be useful for driving the cells strongly and obtaining a more precise estimate of chromaticity of the preferred light.

Phase 2: Tailored subunit white noise

We created a custom white noise stimuli by yoking the pixels within each subunit and stimulating them together (**Figure 3.2B**). The spatial structure of this white noise stimulus was frozen and only the phosphor gun intensities within each subunit was modulated rapidly and independently according to a Gaussian distribution as used in *Phase 1*. We refer to this custom white noise stimuli as “subunit white noise”. Spike triggered averaging of the subunit white noise revealed preferred lights in the two independently stimulated subunits.

The advantage of this approach over the checkerboard white noise was two-fold. First, as emphasized before, the subunit stimulus provided a higher effective contrast and hence a larger drive than the checkerboard stimuli (**Figure S3.1A,C**). Second, the dimensionality of the subunit white noise stimuli was much lower than the checkerboard white noise stimuli. Each frame in the new stimulus has 6 dimensions (2 subunits x 3 independently modulated lights within each subunit) whereas each frame in the checkerboard stimulus has 300 dimensions (10 pixels x 10 pixels x 3 phosphors). The reduction in stimulus dimensionality facilitated a faster estimation of the chromaticity of preferred lights.

After recovering the STA, we predicted the spatial integration across the two subunits by computing a firing rate map—an offline approach that has been used for studying the interaction of signals between multiple spatial filters of V1 complex cells (Touryan, 2002; Rust et al., 2005). We projected the subunit white noise stimuli onto individual subunits, and binned the projection values using a two-dimensional histogram. We computed the ratio of the projections of the spike-triggered stimulus frames over all the subunit white noise frames to obtain the firing rate map (**Figure S3.1D**). The firing rate of the example DO cell increased as the stimulus projections increased, consistent with the idea that larger projections drive the neuron strongly. The neuron appeared to increase its response as a function of weighted linear combination of projections from the two subunits. This analysis is sufficient to identify the interactions between subunits but, the effective drive to the neuron is still constrained and a more incisive analysis of RF subunit interactions requires stimulating them with higher contrast, static lights over a wider range of intensities. A thorough investigation of signal integration over larger contrast range is important because an integration that appears to be linear over a lower contrast range could be non-linear over a larger contrast range.

One approach for investigating spatial integration would be to stimulate the RF subunits with different combinations of light intensities that span the entire gamut range, record the spiking responses to construct a firing rate map, and investigate the firing rate map to deduce the nature of spatial integration. However, this approach is time consuming and to a large extent not feasible because of the vast number of stimulus combinations that will be needed to estimate a firing rate map. A rather simple approach would be find the collection of stimuli that evoke the same response from a neuron. This approach is

known as an isoresponse method, and has been used previously for studying signal integration in the salamander retina, macaque V1 and locust auditory receptor cells. (Gollisch, 2002; Benda et al., 2007; Horwitz and Hass, 2012). We explain how we implemented isoresponse method for our study below.

Phase 3: Isoresponse measurement

We selected the subunit white noise STA frame that differed most from background. We used this stimulus frame to synthesize two images that selectively stimulated the two subunits with their preferred lights (represented along the 45° and 135° directions in **Figure 3.2C**). We created a battery of stimuli by linearly combining the two images in different proportions. This battery of stimuli can be visually represented using a two-dimensional stimulus contrast space (**Figure 3.2C**). The origin in this space represents the background gray of the CRT monitor. Any radial direction in this space represents a linear weighted combination of the two images and the radial distance represents the contrast of the image.

To examine the interactions between subunits, we collected edges in this stimulus space that evoked the same spiking response. We defined the locus of stimuli that elicited the same target response as an isoresponse contour. The shape of the isoresponse contour revealed how stimulation of the two RF subunits drive the target response (**Figure 3.2C–D**) (Schumer, 1984; Gollisch and Herz, 2012; Horwitz and Hass, 2012). For a subset of neurons (9), we made isoresponse measurements at two different firing rates.

Each stimulus was presented for 300 ms and was separated from the preceding and subsequent stimuli by more than 1000 ms. The monkeys typically maintained their visual fixation for at least 150 ms after the stimulus offset, and were rewarded for successful fixation (data not shown).

3.3.6 Contrast staircase procedure

We used a staircase procedure to identify the contrast of each image that evoked the desired target response (Horwitz and Hass, 2012). First, we determined the spike counting window. The onset of the spike counting window was obtained by computing the latency of the subunit white noise STA frame that differed the most from background. The rationale for this choice is that this latency approximates the time delay between stimulus presentation and the spiking response of the recorded neuron. The spike counting window terminated at the stimulus offset time and, was therefore less than 300 ms for every neuron. Next, the staircase procedure compared the total number of spikes in the window to the target response (**Figure S3.2A**). If the firing rate was greater than target response, the staircase procedure increased the contrast of the image by a factor of 1.35. If the firing rate was lower than the target firing rate, the staircase procedure decreased the contrast of the image by a factor of 0.65. This process continued until a reversal occurred (**Figure S3.2B**). A reversal is a response that exceeded the target firing rate after having fallen below it on the previous stimulus presentation or a response that fell below after having exceeded it on the previous stimulus presentation. After each reversal, the magnitude of the contrast adjustment was reduced by a factor of 0.75. The staircase would halt either if the procedure

achieved seven reversals or if the upcoming contrast exceeded the gamut of the monitor. We used the staircase termination point as the contrast of the image that evoked the target response. Presentations of stimuli in two directions in the stimulus space were randomly interleaved to mitigate non-stationarity due to adaptation..

3.3.7 Cell Screening

We recorded from 232 well isolated V1 neurons and made isoresponse measurements for 116 of those. The recording sessions combining 3 phases of the experiment lasted 20–70 mins once a neuronal waveform was isolated.

3.3.8 Cone weights

For each cell, we identified the frame from the spike-triggered averaged subunit stimulus (subunit STA) that differed most from the background. We then took the weighted average of the peak and the two flanking frames (2 subunits x 3 color channels) and used a singular value decomposition (SVD) to separate this weighted STA into a color weighting function and a spatial weighting function, defined as the first row and column singular vectors, respectively (Horwitz and Albright, 2005; De, 2020). The color weighting function and the spatial weighting function together captured nearly 96.4±5.4% of the variance of the spatiochromatic information in the weighted subunit STA.

The color weighting function was converted to cone weights that are assumed to act on cone contrast signals (Weller, 2018). Cone weights were normalized such that the sum of their absolute values was 1 (Derrington et al., 1984; Johnson et al., 2004; Horwitz

and Albright, 2005). Most cells that were analyzed had cone weights with different signs in the two neighboring parts of the RF. There is no principled way of describing such a cell as having cone weights of one sign or the other. Therefore for convenience, we constrained the M-cone weights of all the cells to be positive, and we classified cells as cone-opponent or cone non-opponent by evaluating the signs of L- and S-cone weights relative to the M-cone weight.

3.3.9 Principal component analysis

The interpretation of cone weights as a reasonable description of a cell's color tuning is valid under the assumption of a linear model of cone signal combination (Wachtler, 2003; Conway et al., 2010; Weller, 2018)(Weller and Horwitz; unpublished). If the cell is linear, then STA shows its true chromatic sensitivity. If the cell is nonlinear, the STA only shows the average chromatic sensitivity and can no longer be considered to estimate a preferred color direction.

One way to verify whether the assumption of linearity is violated or not is by checking whether the responses to some stimuli differ substantially from that predicted by the STA. This information could be achieved by computing the principal components orthogonal to the STA using the spike-triggered covariance analysis (Touryan, 2002; Horwitz et al., 2005; Rust et al., 2005; Horwitz et al., 2007). The existence of a clear principal component confirms a real non-linear component of a cell's response even within the regime of low contrast modulations of the subunit white noise.

We used principal component analysis to compute the first principal component (PC1) of the spike-triggered subunit stimuli that was orthogonal to the STA (Horwitz et al., 2005). We assessed the significance of the PC1 with a nonparametric randomization test. To estimate the distribution of this statistic under the null hypothesis of no relationship between stimuli and spikes, we randomly shifted spike trains in time relative to the reconstructed subunit stimulus movie, recalculated the PC1, and obtained its eigenvalue. This procedure was repeated 1000 times. If the PC1 eigenvalue from the unrandomized data exceeded 95% of the largest eigenvalues from the randomized data sets, we concluded that the PC1 was significant at the 0.05 level.

3.3.10 Cell classification

We classified cells as simple, DO or others based on cone weights and the PC1 eigenvalue. As a result, only cells with non-significant PC1 were considered to be simple or DO.

Cells were classified as simple if their L- and M-cone weights had the same sign, accounted for 80% of the total cone weight and individually accounted for at least 10%, and had non-significant PC1. Twenty-seven cells were categorized as simple. DO cells were defined as those that had cone weights of different sign and, L-, M- and S-cone weights individually accounted for at least 30%, 30% and 20% of the total cone weights, respectively, and had non-significant PC1. Twenty-eight cells were categorized as DO. The cells that did not fit the DO or simple cell criteria were categorized as others. There were 61 other cells.

3.3.11 Model fits to staircase termination points

We fit a linear and quadratic model to the set of staircase termination points for each cell and compared the quality of model fits. Fitting was performed using a standard inbuilt MATLAB routine for function minimization (*fmincon*). We fit the model using a robust regression method with a tukey-bisquare objective function and determined the model parameters that best describes the collection of staircase termination points (Fox, 2002).

3.3.12 Linear model

We converted the data points (staircase termination points) from cartesian (x, y plane) to polar coordinates (r, θ plane). Since the data were obtained using a staircase procedure that titrated the contrast along a radial direction in the cartesian plane, the error associated with the termination point was along that radial direction. This means that the error had two components in cartesian plane; one along x direction and the other along y direction. The conversion from cartesian to polar coordinates transformed the error along just one direction i.e. along r. We fit the staircase termination points to a linear model as described below.

$$Ar\cos\theta + Br\sin\theta = 1$$

$$\text{where } r = \sqrt{x^2 + y^2}, \quad \theta = \tan^{-1}\frac{y}{x}$$

x and y each represent the contrast of light to the two the subunits, respectively. The contrast of each subunit was defined as the L2 norm of red, green and blue phosphor intensities with respect to the background.

3.3.13 Quadratic model

We fit the staircase termination points in polar plane to a quadratic model as described below.

$$A(r\cos\theta)^2 + B(r\sin\theta)^2 + Cr^2\cos\theta\sin\theta + D\cos\theta + E\sin\theta = 1$$

The model corresponds to a conic section in cartesian plane as described below.

$$Ax^2 + By^2 + Cxy + Dx + Ey = 1$$

3.3.14 Evaluating model fits to staircase termination points

We evaluated the quality of model fits by calculating the sum of tukey-bisquared errors between the data and the model predictions. To avoid overfitting, we used leave-one-out cross validation. We report the median cross-validated error from the linear and quadratic fits.

3.3.15 Spatial NLI

The spatial non-linearity index (spatial NLI) was defined as the median of ratio of cross-validated linear and quadratic errors in logarithmic units.

$$Spatial\ NLI = log_{10}\ (median\ (\frac{Cross-validated\ error_{Linear\ model}}{Cross-validated\ error_{Quadratic\ model}}))$$

3.3.16 Analysis of signal combination within subunits

We assessed signal integration across space by fixing the ratio of red, green and blue phosphor intensities and titrating the overall intensities together. Therefore, information

about signal integration within individual subunits cannot be achieved with the collection of stimuli presented during the isoresponse measurement because the proportion of the different phosphor intensities was not modulated. An insight into the signal integration within individual subunits can be gained from the analysis of subunit white noise stimuli in which the red, green and blue phosphor intensities were independently modulated.

We analyzed how the red, green and blue phosphor intensities (during the Phase 2 of the experiment) within each subunit were combined to evoke a spiking response. We classified each stimulus (triplet of red, green and blue gun intensity) that was presented onto a subunit as belonging to either spike-triggered or non-spike-triggered ensemble. We fit the spike-triggered and raw stimulus ensemble of phosphor gun intensities using a generalized linear model (GLM) and a generalized quadratic model (GQM) to predict the probability of spiking for every triplet of phosphor intensity (**Figure 3.6A**). The models were fit using a MATLAB routine (*fitglm*) that maximized likelihood assuming a binomial error.

The GLM is described as below.

$$P(spike) = logistic(w_1 R + w_2 G + w_3 B + C)$$

R, G and B are phosphor intensities relative to the background gray that serve as the input to the model. w_1, w_2 and w_3 are the fitted coefficients and, C is a fitted constant. The output of the model is the probability of spiking given any triplet of red, green and blue phosphor intensity.

The GQM is described as below.

$$P(spike) \quad = \quad logistic(w_1R^2 + w_2G^2 + w_3B^2 + w_4RG + w_5GB + w_6RB + w_7R + w_8G + w_9B + C)$$

3.3.17 Evaluating performance of generalized linear and quadratic models

To avoid overfitting, we used 10-fold cross validation, fitting the model with 90% of the data and testing the model on the remaining 10%. We computed the performance of the fitted models to predict whether a stimuli evoked a spike or not using a receiver operating characteristic (ROC; **Figure 3.6B**) (Green and Swets, 1966). The performance was quantified as the normalized area under the ROC curve. We then computed the median of the cross-validated performances, averaged across subunits. We report a single scalar value for each neuron.

3.3.18 Cone signal NLI

The cone signal non-linearity index (cone signal NLI) was defined as the median of differences between the cross-validated GLM and GQM performance for each subunit.

$$Cone\ signal\ NLI = \frac{\sum_{subunit=1}^{2} median(Cross-validated\ accuracy_{GQM} \ - \ Cross-validated\ accuracy_{GLM}))}{2}$$

3.3.19 Analysis of signal integration within LGN RFs

RFs of 85 well isolated LGN (parvo-, magno- and koniocellular) cells were characterized by spike triggered averaging of the white noise checkerboard stimuli. For 40 neurons, the stimulus consisted of 0.14˚ squares arranged in a 10 × 10 grid, and for the rest,

squares were 0.09˚ and arranged in a 12 × 12 grid. Data from a subset of these neurons have been published previously (Horwitz, 2020).

Analysis of cone signal combination was performed similar to the approach described above for V1 cells, except that the cone signal NLI was computed for a single pixel that differed most from the background.

3.3.20 Analysis of spatial RF structure

We assessed the spatial RF structure by fitting and comparing standard models (Gabor and Difference-of-Gaussians) in the field. The detailed procedure is described in the Chapter 2.

3.4 RESULTS

We analyzed the spiking responses of 116 V1 neurons from two awake fixating macaque monkeys (79 from Monkey 1, 37 from Monkey 2). RFs of neurons ranged in eccentricity from 1.4° to 5.9° (median = 3.6°). For each neuron, we first rigorously characterized their RFs (*Phase 1 & 2*), and then, measured signal integration across the spatial RFs (*Phase 3*).

3.4.1 Characterizing RF and classifying cells

We used spike-triggered averaging (STA) of white noise stimuli to reveal the average preferred light by a neuron (**see Experimental Protocol, Figure 3.2A–B**). We computed the cone weights from the STA to determine the average chromatic sensitivity (**see Cone weights**). The cone weights serve as an accurate description of a cell's chromatic tuning if the cell is linear. However, if a cell is non-linear, the STA only shows the average chromatic sensitivity and can no longer be considered to estimate a preferred chromaticity, thereby deeming cone weights uninterpretable (Wachtler, 2003; Horwitz et al., 2005, 2007). We therefore determined whether a cell is non-linear within the limited contrast regime of white noise subunit stimuli. We used spike-triggered covariance analysis to obtain the PC1 that was orthogonal to the STA and assessed its statistical significance (Horwitz et al., 2005, 2007) (**see Principal component analysis**). The existence of a significant PC1 confirms a real non-linear component of a cell's response.

We classified neurons as simple, DO or others based on cone weights and the significance of PC1 (**see Cell Classification**). Simple cells had non-significant PC1 and, large magnitude, non-opponent L- and M-cone weights that, together, accounted for 80% of the total cone weight (n=27). DO cells, by definition, had non-significant PC1 and cone weights of opposite signs (n=28). The rest of the neurons that were neither simple nor DO were classified as others (n=61).

Once the RFs were thoroughly characterized and the cell types were identified, we measured the interaction of signals across the non-overlapping regions of the RF that had different chromatic preferences. For each neuron, we used an automated, closed-loop system to find a collection of edges that evoked the same firing rate. We explain the rationale and utility of this approach for understanding spatial integration.

3.4.2 Isoresponse method: a tool for measuring spatial integration

Consider a V1 neuron that combines signals linearly across the two neighboring RF subregions (**Figure 3.2C**). The combined signal is transformed to a spiking response via a threshold spiking non-linearity. In most cases, the spiking non-linearity might dominate the stimulus-response relationship and may confound the nature of spatial integration. For example, the response to stimulus 1 (along the 45° direction in **Figure 3.2C**) plus the response to stimulus 2 (along the 135° direction in **Figure 3.2C**) may not equal the response to stimuli 1 and 2 presented together if neither stimulus is strong enough to drive a response by itself but together they can. However, the stimulus-response relationship could be analyzed in a way that is agnostic to this spiking non-linearity. The

information about spatial integration is embedded in the shape of the isoresponse contours—collection of different stimuli that evoke the same response (Schumer, 1984; Benda et al., 2007; Horwitz and Hass, 2012). For a linear cell, the isoresponse contours are lines. Note that the spiking non-linearity changes the spacing between the isoresponse contours but does not bend them. For a non-linear cell, the isoresponse contours are curves (**Figure 3.2D**). Therefore, the measurement of isoresponse contours is an effective method for bypassing the spiking non-linearity and investigating the true underlying spatial stimulus integration (Gollisch and Herz, 2012).

Determining stimuli that evoke the same response from a cell, a priori, is challenging because of the diversity of spatial and chromatic tuning of V1 neurons (Lennie et al., 1990; Johnson et al., 2004; Horwitz et al., 2007). Therefore, we first estimated the spatial and chromatic tuning using spike-triggered averaging, and then engineered a stimulus space using the STA to seek stimuli that stimulate two parts of the RF in different ways but nevertheless drive the same response (**see Experimental Protocol)**.

We measured isoresponse contours using a closed-loop staircase procedure that titrated the stimulus contrast to drive a neuron at a desired target response, similar to a previous application in V1 (**see Contrast staircase procedure**) (Horwitz and Hass, 2012). The staircase procedure for any particular stimuli fixed the ratio of the phosphor intensities within and across the two neighboring RF subregions but modulated the overall phosphor intensities. An example staircase is shown that titrated the stimulus contrast to evoke a target response of 20 ips from a DO cell (**Figure S3.2**).

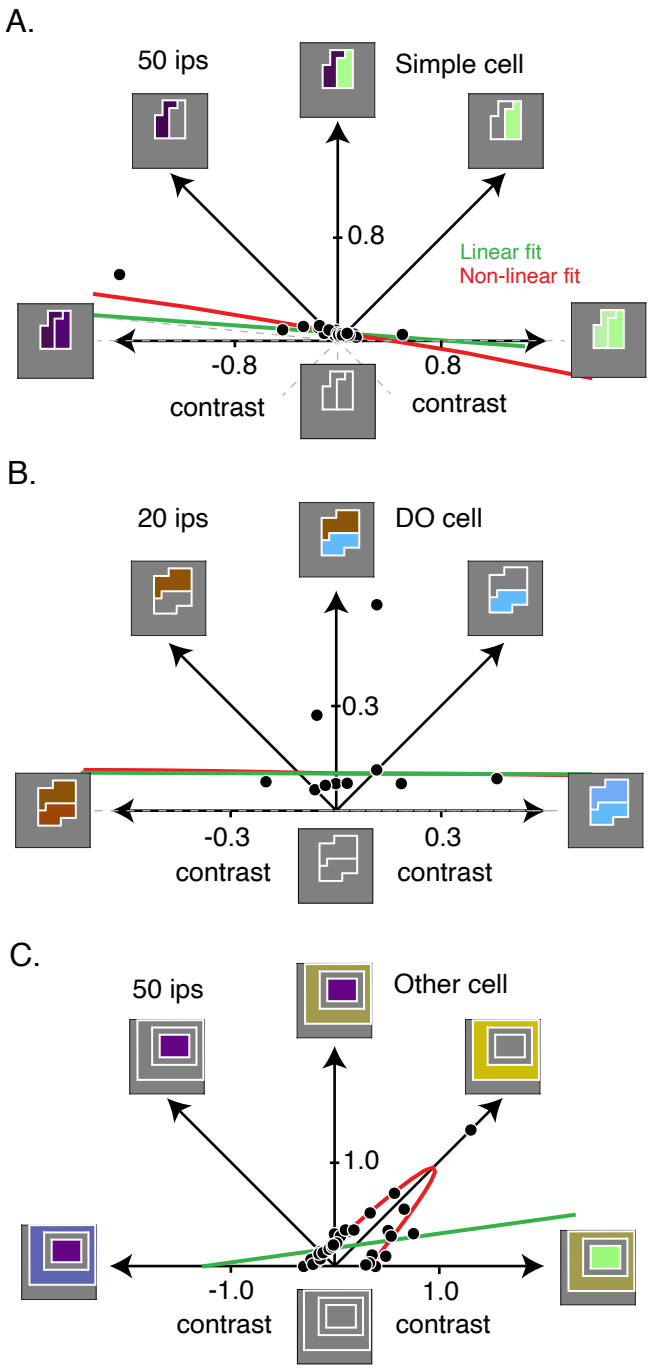

Figure 3.3. Isoresponse measurements of three example cells. **A.** Collection of stimuli that drove at 50 ips. Dots indicate the staircase terminations and gray dashed lines indicate staircases that exceeded the monitor gamut. The linear (green) and non-linear (red) fits to the data suggest that the spatial intergation is linear. **B.** Same as **A.** but for a DO cell. Contrast was titrated to drive the cell at 20 ips. **C.** Same as **A.** but for a cell that is neither simple nor DO. Isoresponse measurements were made for 50 ips. The spatial integration is non-linear.

3.4.3 Signal integration across spatial RF

We found V1 neurons consistent with linear and non-linear spatial integration of visual signals. Shown are the staircase termination points from one example each of simple, DO and other cell types (**Figure 3.3**). Consider the data from the simple cell that responds strongly to a ON-OFF luminance (green—ON, purple—OFF) edge (**Figure 3.3A**). There are two major observations to be made. First, the staircase terminations are well described by a line which is evident from the similarity of linear and non-linear model fits. Second, the cell responds to a bright-dark ON luminance edge and, a bright-dark OFF luminance edge throughout the range of the display. The contrast needed to drive these edges are higher than the ON-OFF luminance edge suggesting that the neuron is sensitive to luminance contrast across an edge. This result is consistent with a linear spatial integration. The example DO cell displayed a similar outcome by selectively responding to the differences in red and cyan chromaticities across the neighboring RF regions. This result suggests that this DO cell responds to the chromatic contrast of an edge (**Figure 3.3B**).

The other cell type displayed a clear non-linear spatial integration of visual signals (**Figure 3.3C**). This cell responded weakly to the surrounding stimulus and strongly to the center stimulus; the contrast sensitivity of the center alone is given by the distance of the point from the origin along the 135° direction, and the sensitivity of the surround is given by the distance of the point along the 45° direction. The cell responded strongly to the concurrent presentation of light in the center and surround and, similarly to lights of opposite chromaticity in the center. Such a trend of staircase termination points cannot be explained by a linear spatial integration of visual stimulus. Note that the surrounding

subunit is within the classical RF and not outside it; surround outside the RF does not evoke a spiking response by itself but modulates the signal in classical RF (Cavanaugh, 2002; Solomon et al., 2004; Hallum, 2014; Henry, 2020). Measurements from a different cell confirmed that non-linearity of the isoresponse contour was present at two different firing rates (**Figure S3.3**).

To quantitatively assess spatial integration, we compared the cross-validated errors from the linear and quadratic model fits (**see Evaluating model fits to staircase termination points**). We chose the cross-validated analysis because it is not biased by the number of parameters in the model. Separate portions of the data are used to fit the model and to calculate the prediction error, thereby penalizing overfitting. We chose quadratic model because it is the simplest of all the non-linear models that can be parametrically defined. If the quadratic model is a reasonable description of the spatial integration, then the fits to the isoresponse contours would be expected to have larger errors from linear model than quadratic model. Most cells (79/116) had larger linear errors than quadratic errors suggesting that the spatial integration is largely non-linear (**Figure 3.4A**).

The degree of non-linearity was quantified as the spatial non-linearity index (spatial NLI; **see Evaluating model fits to staircase termination points**). A spatial NLI of 0 corresponds to equivalent predictions by the linear and quadratic models, a value < 0 corresponds to the linear model providing more accurate predictions than the quadratic model and value > 0 corresponds to the quadratic model providing more accurate

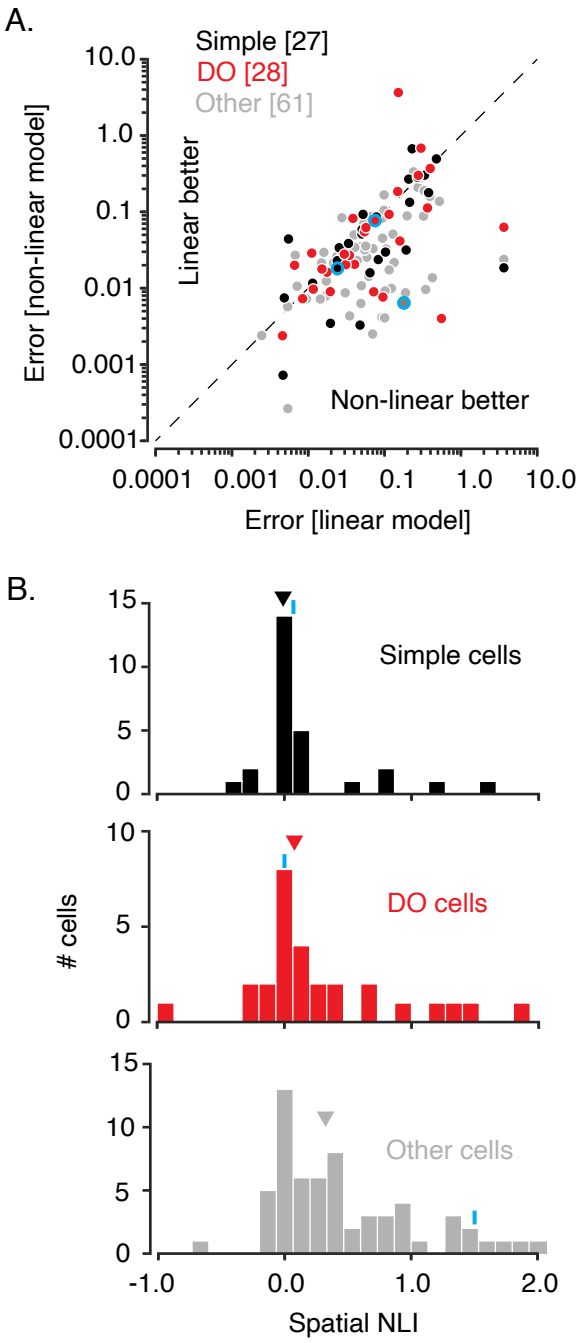

Figure 3.4. Population results from closed-loop isoresponse experiments **A.** Cross validated error from non-linear fits are plotted against the errors from linear fits for simple, DO and ambiguous cells. Example neurons are encircled in blue. **B.** Histogram of NLI. NLI of example neurons are maked with blue ticks, and the median is marked with triangles.

predictions than the linear model. As expected, simple cells were largely linear (median spatial NLI = -0.0095; p=0.30, Wilcoxon sign-rank test) (Movshon et al., 1978a). DO cells were biased towards integrating spatial signals non-linearly (median spatial NLI =

0.0794, p=0.02, Wilcoxon sign-rank test) but they integrated signals about as linearly as simple cells (p=0.33, Mann-Whitney U test). Spatial NLIs were greater for other cells than for simple and DO cells (median spatial NLI = 0.3232; p=0.008, Kruskal-Wallis test, **Figure 3.4B**).

Some neurons have oriented side-by-side RF subunits whereas other neurons have RFs consisting of a center and a diffuse surround. Differences in the geometry of RF subunits could be related to the differences in neural circuitry, and might manifest as differences in the mechanisms of spatial integration. We considered whether the geometry of the RF subunits might be predictive of how neurons integrate visual signals across their RFs. The non-linearity could be a specific feature of RF subunits with a center-surround geometry (**Figure 3.3**). The spatial NLIs of neurons with center-surround RF geometry did not differ from the spatial NLIs of neurons with oriented RF geometry (p=0.78, Mann Whitney U test).

We also considered whether the above result could be due to incorrect selection of subunits from the white noise STA, for example, selection of center-surround subunit geometry for cells with truly oriented RFs and vice versa. An incorrect selection of subunits would stimulate parts of RFs that do not have homogenous chromatic sensitivities, and therefore, may lead to unintended non-linear responses as a consequence of the threshold spiking non-linearity. To determine the spatial structure of the RFs, we fitted them with two standard models in the field, the Gabor model and the Difference-of-Gaussians (DoG) model, and compared their fits—similar to our previous

study (De, 2020). The Gabor model assumes that a RF is orientation-tuned whereas the DoG model assumes a radially symmetric center-surround RF structure. The spatial RF structure was tightly linked to the selected subunit geometry ($p = 0.005$, Fisher's exact test); oriented subunits were selected for Gabor-like RFs and center-surround subunits were selected for DoG-like RFs (**see Analysis of spatial RF structure**). Together, these analyses suggest that the non-linear integration of visual signals is not an artifact of how subunits were selected.

3.4.4 Signal integration within individual subunits

The spatial integration measured by the isoresponse method summarizes the visual processing by the entire V1 circuitry—from photoreceptors to V1 cells. We therefore asked where in the neural circuit could this non-linearity arise. We hypothesized that the non-linear cells combine signals across their linear RF subunits non-linearly. We illustrate the logic of this hypothesis by considering two simple models of non-linear stimulus integration (**Figure 3.5A–B**). In both models, the signals within individual subunits are transformed via a threshold spiking non-linearity prior to being combined spatially, similar to the non-linear spatial filter described previously (**Figure 3.1C**). The isoresponse measurements will yield nearly similar results for both these models. However, the models differ in how signals are combined within individual subunits; for this example, we considered the combination of cone signals. Cone signal combination is linear in the first model and non-linear in the second model (**Figure 3.5A–B**).

A systematic isoresponse measurement could be useful for revealing the nature of signal integration within individual subunits. However, this would significantly increase

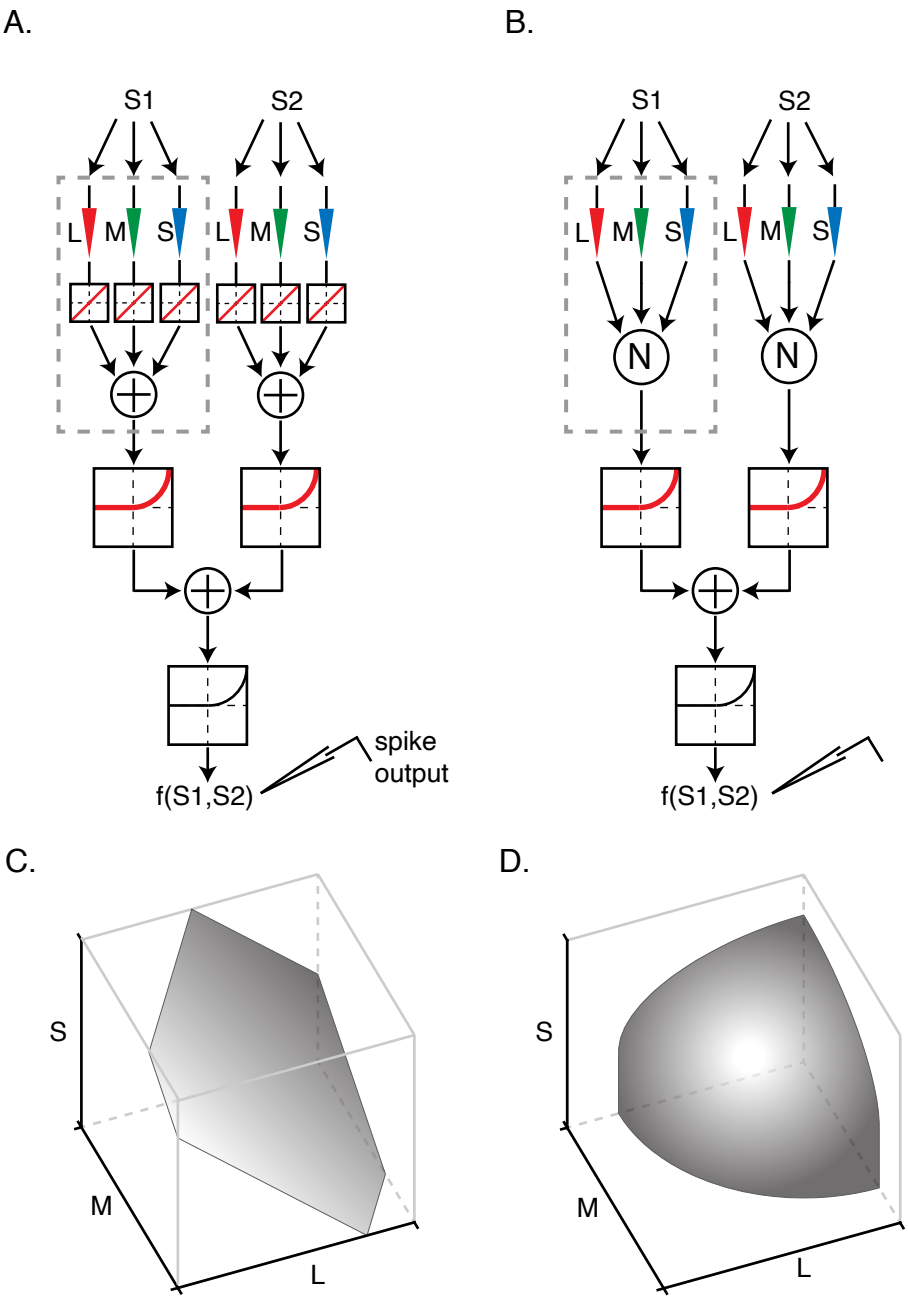

Figure 3.5. Underlying cone signal combination in non-linear stimulus integration models **A.** A non-linear spatial filter that combines cone signals linearly. The combined cone signals within each of the subunits are transformed under a threshold quadratic non-linearity. The trandormed signals from both the subunits are summed to generate a response f(S1,S2) via a rectified spiking non-linearity. **B.** A non-linear spatial filter that tranforms each of the cone signals non-linearly prior to combining them. Note that the signals within each of the subnits are non-linearly transformed before being combined spatially. **C.** Isoresponse surface of cone signal combination within one subunit (highlighted in gray in **A**) is plotted. The isoresponse surface is a plane as the cone signals are summed within the subunit. The spiking non-linearity does bend the planar surface **D.** Same as **(C)** but for non-linear intergation model in **(B)**. The isoresponse surface is a curved manifold and not a plane.

the duration of the experiment, compromise the stationarity of the single-unit recordings due to adaptation, and complicate the interpretation of the data. A simple approach would be to extract the information about how red, green and blue phosphor intensities are combined within individual RF subunits from the *Phase 2* of the experiment. Next, we outline how this approach could be used for studying signal integration within individual RF subunits, in detail.

Each stimulus frame in *Phase 2* can be described with 6 numbers: a set of red, green and blue phosphor intensities for each of the RF subunits (**see Experimental Protocol**). We can therefore think of the *Phase 2* experiment as sampling a 6-dimensional space of stimuli. If phosphor intensities combine linearly within each RF subunit, then the influence of that subunit on the spiking response is summarized by a weighted sum of red, green and blue phosphor intensities. Of course, we cannot probe the drive from one subunit directly in this experiment, and whether the neuron evokes a spike or not depends on the visual processing by both subunits. However, because the stimulus distribution is radially symmetric, we can test for the linearity of signal integration within each subunit regardless of the visual processing in the neighboring subunit. The stimulus is independent on the two subunits of the RF, so the influence of one subunit is independent of the influence of the other and will just manifest as noise. We can therefore safely determine a collection of red, green and blue phosphor intensities for each subunit that would be equally likely to evoke a response. If the neuron combines the phosphor intensities linearly within each subunit, the isoresponse surfaces will be planes, and if the neuron combines phosphor intensities non-linearly

within each subunit, the isoresponse surfaces would be curved manifolds (**Figure 3.5C–D**).

We used a novel model based approach to investigate the underlying signal integration (**see Analysis of signal combination within subunits**). During *Phase 2* of the experiment, some phosphor triplets evoked a spike and the rest did not. Using the red, green and blue phosphor intensities as inputs to a GLM and a GQM, we obtained the probability of a phosphor triplet to evoke a spike for each subunit (**Figure 3.6A**). The phosphor intensities were combined linearly by the GLM and non-linearly by the GQM (**see Analysis of signal combination within subunits**). Similar to the isoresponse method, this model based approach is agnostic to the non-linearities post phosphor signal combination. The combination of phosphor intensities is analogous to cone signal combination because there exists a linear transformation between the phosphor intensities and the cone-contrast (Weller, 2018). As a result, the conclusion from the GLM/GQM analysis is invariant to the choice of the color space; a linear transformation does not change a plane into a curved surface or a curved surface into a plane.

We computed the model performances using ROC analysis and combined the results from both the subunits for each cell (**Figure 3.6B**)(Green and Swets, 1966). We quantified the difference in performance of GLM and GQM as cone signal non-linearity index (cone signal NLI) (**see Evaluating performance of generalized linear and quadratic models**). A cone signal NLI < 0 corresponds to the GLM providing more accurate predictions than the GOM, and a cone signal NLI > 0 corresponds to the GQM providing more accurate predictions than the GLM model (**Figure 3.6C**).

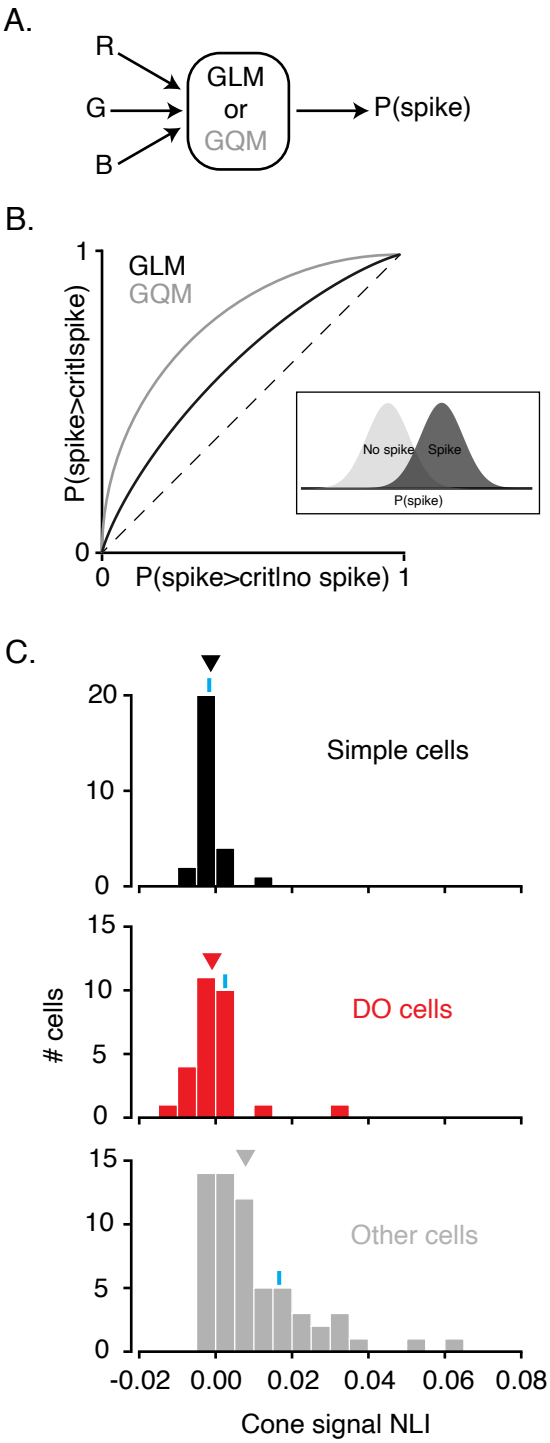

Figure 3.6. Analysis of underlying cone signal combination **A.** Probability of spiking is predicted for combination a red, green and blue gun phosphor intensity presented within a subunit using a GLM and a GQM. **B.** A ROC analysis is used to assess the performance of GLM and GQM. Performance evaluates the ability to detect stimuli that evoked spikes vs. no spikes (inset). **D.** Histogram of cone signal NLI. NLI of example neurons are maked with blue ticks, and the median is marked with triangles.

Most V1 cells had cone signal NLI > 0 indicating non-linear cone signal combination (64/116). Finer interrogation revealed that cone signal NLI was different across the three

cell types ($p<0.0001$, Kruskal-Wallis test). Simple and DO cells had lower cone signal NLIs than other cells (median cone signal NLI for simple cells = -0.0013, $p = 0.002$, Wilcoxon sign-rank test; median cone signal NLI for DO cells = -0.0009, $p = 0.34$, Wilcoxon sign-rank test; median cone signal NLI for other cells = 0.0078, $p < 0.0001$, Wilcoxon sign-rank test) (**Figure 3.6D**).

We considered the possibility that the non-linearity observed within RF subunits could be due to non-linear cone signal integration by individual LGN neurons and V1 neurons might be simply inheriting this signal. Therefore, we used the same model based analysis to investigate the cone signal combination within LGN RFs that were characterized using white noise checkerboard stimulus (**see Analysis of signal integration within LGN RFs**). Cone signal NLI of LGN cells were similar to that of simple and DO cells (median = -0.0004, $p = 0.002$, Wilcoxon sign-rank test; **Figure S3.2**). This result suggests that the non-linearity observed within the RF subunits of some V1 cells is most likely to arise after LGN signals are processed.

3.4.5 Link between spatial integration across and within RF subunits

We previously hypothesized that the non-linear cells combined signals nonlinearly across their linear RF subunits. Having thoroughly characterized the signal integration within subunits, we asked whether the non-linear cells are more likely to have linear RF subunits. Therefore, we investigated the relationship between spatial NLI and cone signal NLI. We emphasize that these two metrics are based on measurements that

were made using different stimuli at different phases of the experiment, and therefore there was no a priori reason for the cone signal NLI to be related to spatial NLI.

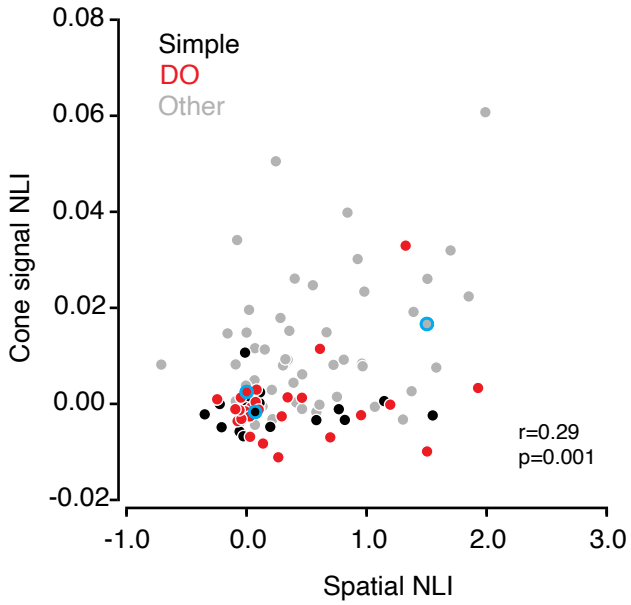

Figure 3.7. Relationship between spatial NLI and cone signal NLI. Data from example neurons are encircled in blue.

We found that cone signal NLI is strongly correlated to spatial NLI suggesting that the non-linearity within individual subunits could be the basis of non-linearity observed in the isoresponse measurements (Spearman's r = 0.29, p=0.001; **Figure 3.7**). This result thus rejects the class of non-linear stimulus integration models that combine signals non-linearly across their linear RF subunits (**Figure 3.5A**).

3.4.6 Relationship between S-cone input and signal integration

V1 cells with strong S-cone input are particularly non-linear (Cottaris and De Valois, 1998; Horwitz et al., 2005; Conway and Livingstone, 2006). We, therefore, investigated whether S-cone input was related to non-linear signal integration within and across

individual subunits. We used the magnitude of S-cone weight as a measure of S-cone input to a cell (**see Cone weights**). Spatial NLI (r = 0.28, p=0.002, Spearman's correlation between spatial NLI and S-cone weight magnitude; **Figure 3.8A**) and cone signal NLI (Spearman's r = 0.18, p=0.055, Spearman's correlation between cone signal NLI and S-cone weight magnitude; **Figure 3.8B**) were strongly correlated with S-cone input. A finer interrogation of the data revealed that the positive correlation was preserved for other cells (Spearman's r = 0.33, p=0.01, Spatial NLI; Spearman's r =

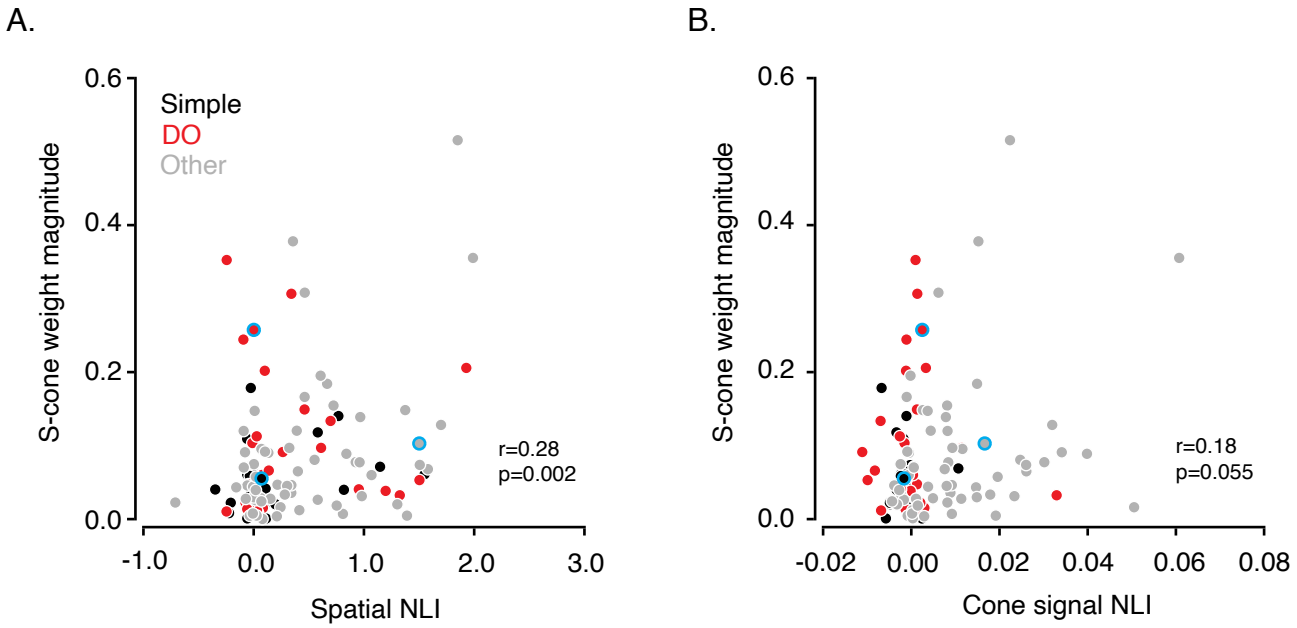

Figure 3.8. Relationship between S-cone input and signal integration. Data from example neurons are encircled in blue across both the panels. **A.** Scatterplot of S-cone weight magnitude and spatial NLI. **B.** Scatterplot of S-cone weight magnitude and cone-signal NLI.

0.27, p=0.03, cone signal NLI) but not for simple (Spearman's r = 0.11, p=0.59, Spatial NLI; Spearman's r = -0.13, p=0.51, cone signal NLI) and DO cells (Spearman's r = 0.19, p=0.33, Spatial NLI; Spearman's r = 0.13, p=0.52, cone signal NLI). This trend cannot be explained by differences in S-cone inputs across cell types (p=0.22, Kruskal-Wallis

test). These results altogether suggest that the S-cone signals are combined non-linearly within the RF subunits of most other cells, and the mechanisms by which S-cone signals are combined within RF subunits is different in DO and simple cells than other cells.

3.5 DISCUSSION

We investigated the spatial integration of visual signals by V1 cells with white noise RF mapping, closed-loop isoresponse measurements, and statistical model comparisons. To the best of our knowledge, this is the first study that compares spatial integration performed by simple and DO cell types. We report three major results. First, we found that many DO cells integrated color signals across their spatial RFs as linearly as simple cells combined luminance signals across their RFs. This result suggests that DO cells respond to the chromatic contrast of edges. Second, we found that V1 cells that are neither simple nor DO integrated signals across space more non-linearly than DO and simple cells, and this non-linearity is most likely due to non-linear signal integration within individual RF subregions—a novel finding of this study. Third, we found that S-cone signals among some other cell types might be processed non-linearly. Together, our results suggest that the spatial integration of DO and simple cells are largely linear and, the spatial non-linearity in some other V1 cells could be a reflection of the non-linear integration of S-cone related signal within RF subunits.

Below, we compare our results to those of previous studies. We then discuss the implications of our results on understanding the circuitry that underlies DO and simple cells. Finally, we discuss their role in image processing.

3.5.1 Comparison with previous studies

The spatial linearity of V1 simple cells is well documented (Movshon et al., 1978a; Schumer, 1984; Ferster, 1988; Tolhurst, 1990; DeAngelis, 1993; Hirsch, 1998; Ferster, 2000). In-vivo intracellular measurements in cats have shown that the linearity is due to

a push-pull (excitation-inhibition) mechanism—stimuli of the reverse contrast evoke responses of the opposite sign within each subregion. Push (excitation) is thought to be mediated by a thalamic drive whereas pull (inhibition) is thought to be mediated by intracortical inhibition (Hirsch, 1998). Compared to simple cells, there have been fewer investigations about how V1 DO cells process light, and the results about the spatial integration of visual signals are inconclusive (Livingstone and Hubel, 1984; Conway, 2001; Conway and Livingstone, 2006; Johnson et al., 2008).

We combined white noise analysis and closed loop measurements to measure the interaction of signals across spatial DO cell RFs. By comparing linear and non-linear model fits to the data, we found that most DO cells, like simple cells, combined signals across their spatial RF linearly—consistent with a push-pull mechanism. Further analysis using a model based approach revealed that the underlying signal integration within individual subunits is more likely to be linear.

Some other V1 cells combined signals across their spatial RFs non-linearly. Analysis of cone signal combination within individual RF subunits revealed that the signal integration is also mostly non-linear. This result rejects the class of models in which other V1 cells combine signals across their RF subunits non-linearly.

Nonlinear signal integration by V1 cells is strongly related to the magnitude of S-cone input (De Valois et al., 2000; Horwitz et al., 2005; Conway and Livingstone, 2006). Most studies have either stimulated the whole RF together (e.g. with a grating or a uniform

light) or stimulated the RF in ways such that the subregions were only discovered after

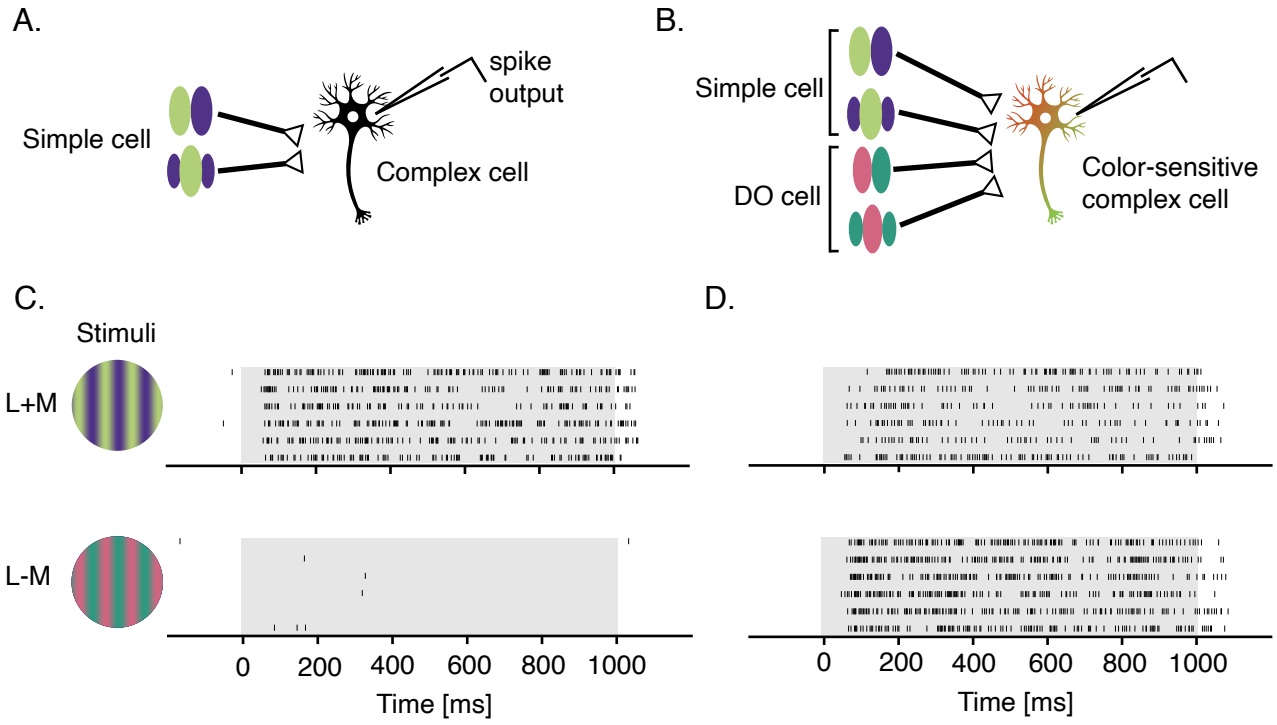

Figure 3.9. Proposed downstream circuitry for DO cells **A.** A hypothetical complex cell receiving input from odd- and even-symmetric simple cells. **B.** A hypothetical color-sensitive complex cell receiving input from odd- and even-symmetric simple and DO cells. **C.** Response of an example complex cell to 3Hz drifting sinusoidal grating. The top stimulus moduluates L- and M-cone contrasts in phase whereas the bottom stimulus modulates L- and M- cone constrasts in opposite phase. **D.** Same as **C** but for a color-sensitive complex cell.

the experiment was over. Our results advance previous studies by targeting the identified RF subregions to probe their contributions to spiking, and dissecting the neural circuit that underlies the non-linear signal integration. The results from the current study suggest that some non-linear V1 neurons appear to pool presynaptic (perhaps LGN recipients in V1) signals, particularly those from S-cone dominated pathways, non-linearly. The non-linear synaptic pooling could presumably be important for high selectivity or invariance to certain hues (Hanazawa et al., 2000; Wachtler, 2003; Horwitz and Hass, 2012).

3.5.2 DO and simple cells: Neural circuitry

Previously, we showed that DO cells, like simple cells, have Gabor-like RFs (**Chapter 2**). Here we show that DO cells, like simple cells integrate signals across their spatial RFs linearly. Just as how a push-pull mechanism appears to be the basis of spatial linearity of simple cells, the same mechanism could be the basis of spatial linearity of DO cells (Conway and Livingstone, 2006). The similarity in spatial RF structure and spatial integration properties suggests that DO cells are cone-opponent homologues of simple cells and argues for a canonical neural circuity for both these cells types. Such a canonical circuitry would imply the existence of a similar but separate system for processing luminance and chromatic edges (Cavanagh, 1991; Leventhal, 1995; Friedman, 2003; Rentzeperis, 2014). Indeed, V1 cells in cytochrome oxidase inter blobs have been found to be orientation-selective and are strongly tuned to either achromatic or equiluminant stimuli suggesting that DO cells are enriched outside the blobs (Garg, 2019).

Simple cells are thought to provide input to complex cells (Hubel and Wiesel, 1962; Alonso, 1998). Like simple cells, complex cells are orientation-selective and respond to luminance edges but are invariant to changes in the spatial phase of a stimuli within their RFs. The spatial phase invariance could be explained by a model where complex cells pool signals from odd- and even-symmetric simple cells with overlapping RFs (**Figure 3.9A,B**).

A homologue of complex cells in monkey V1 that only responds to chromatic but not luminance edges has not being reported. However, the existence of complex cells that respond to both chromatic and luminance edges is well known. These cells have been suggested to be the neural correlates of cue-invariant edge detection, in the sense that they can respond to an oriented edge of any chromaticity (Gouras, 1979; Johnson et al., 2004; Horwitz et al., 2007). The color-sensitive complex cells could pool signals from a pair of odd- and even-symmetric simple and DO cells, and thus achieve invariance to spatial phase across a variety of chromaticities (**Figure 3.9C,D**). The results from the current study suggest that DO cells could be the basis of chromatic sensitivity of color-sensitive complex cells, thus advancing the canonical circuitry framework.

3.5.3 DO and simple cells: Role in image processing

The spatial linearity of DO cells is well suited to maintain a constant representation of a chromatic edge under changing illumination. Therefore, DO cells may contribute to color constancy the same way as simple cells may contribute to lightness constancy.

As previously stated, our results imply that the processing of edges in V1 happens independently for color and luminance. Such a parallel processing is advantageous for two reasons. First, illumination boundaries are associated with luminance variations whereas material boundaries are associated with both luminance and chromatic variations. Thus, chromatic variations are a reliable indicator of material boundaries. A parallel analyses of edges based on color and luminance should provide redundant sources of information for material boundaries and help localize them in natural scenes (Cavanagh, 1991). Assuming that the downstream targets of DO and simple cells are color-sensitive complex and complex cells, a simple subtraction of the complex cell responses would be well suited for signaling material boundaries. Second, orientation of chromatic variations relative to luminance variations impacts 3-D percept (Kingdom, 2003; Kunsberg, 2018). Alignment of chromatic and luminance edges suppresses the percept of 3-D form whereas misalignment enhances the 3-D percept (Kingdom, 2003). A parallel analyses of edges based on color and luminance should provide independent sources of orientation information that could be compared by a downstream circuitry. A sufficiently complex downstream decoder could compare the orientation information between DO and simple cell responses, and aid in shape-from-shading.

3.6 SUPPLEMENTARY FIGURES

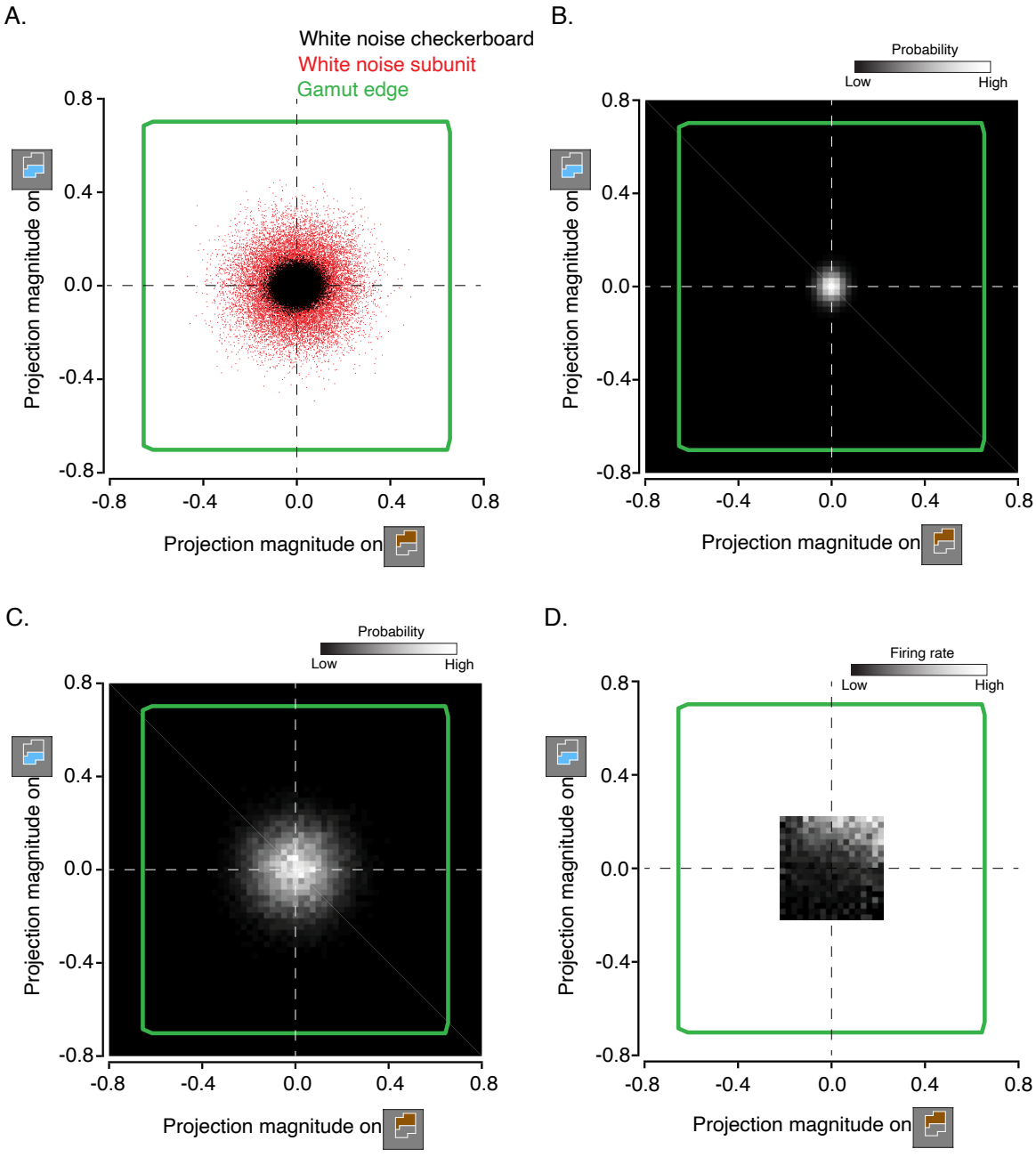

Figure S3.1. Comparison of the effective stimulus drive between three phases of the experiment. The effective drive for each subunit was quantified by projecting stimulus frames onto the spatial–temporal–chromatic subunit kernels of the example DO cell shown in Figure 2. **A.** Scatterplot of the projected white noise checkerboard (black) and white noise subunit (red) stimuli onto each subunit. The effective drive of the white noise checkerboard is smaller than the white noise subunit stimuli, and the projection magnitudes of both stimuli are well within the gamut edge (green) of the display. The whitenoise checkerboard stimuli has a slightly higher variance along x– than y–axis because of two additional pixels in one subunit than the other. **B.** 2-dimensional distribution of the whitenoise checkerboard projections shown in **(A)**. The probability of the projection magnitudes is indicated by the pixel intensity. **C.** Same as **B.** but for whitenoise subunit stimuli. **D.** Firing rate is plotted as a function of projected whitenoise subunit stimuli. The range of the x– and y–axes for which the firing rate is displayed extends from 5 to 95 percentile of stimulus projections. Within this range, the firing rate appears to increase as a function of a weighted linear combination of the stimulus projections.

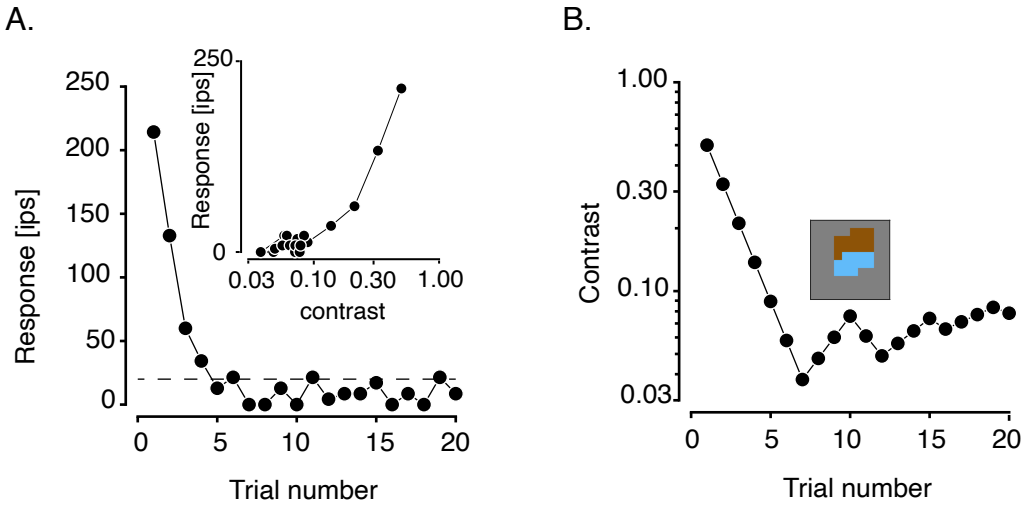

Figure S3.2. An example staircase from the closed-loop procedure of a DO cell in Figure 3.2 **A.** Plotted are the neuronal response as a function of trial number from the example staircase. The staircase titrated the contrast to evoke a response of 20 ips (dashed line). The response droped steeply with decrement in contrast (inset). **B.** Contrast is plotted as a function of the trial number for the same staircase.

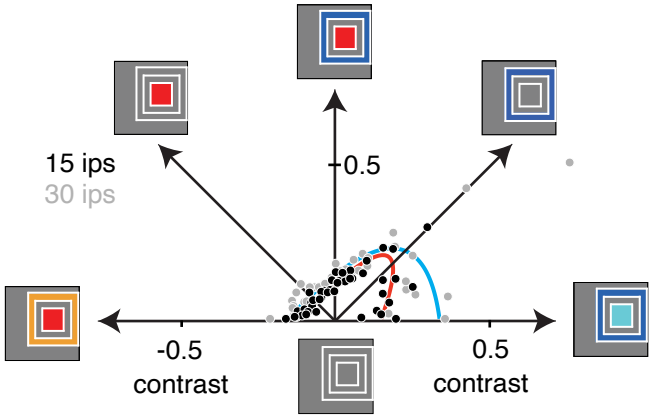

Figure S3.3. Isoresponse measurements at two different target firing rates of an example other cell. The non-linearity of the spatial intergation is consistent across 15 ips and 30 ips. Note that the contrast needed to evoke 30 ips is higher than 15 ips to varying degrees.

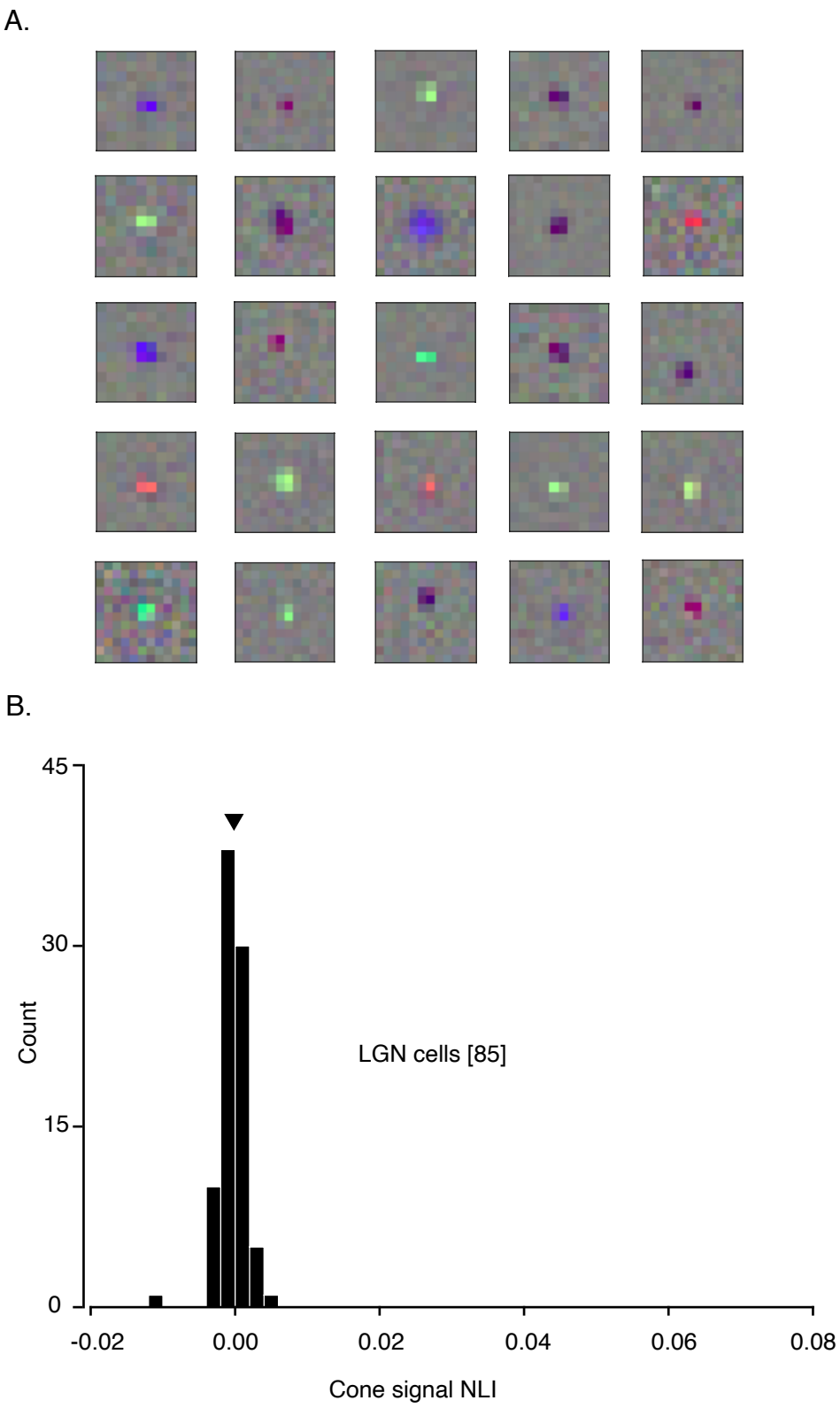

Figure S3.4. Data from LGN cells. RFs were obtained using spike-triggered avergaing. For 40 neurons, the whitenoise stimulus consisted of 0.14˚ squares arranged in a 10×10 grid; for 45 neurons, squares were 0.09˚ and arranged in a 12×12 grid. **A.** Example STAs of 25 LGN cells. **B.** Histogram of cone signal NLI for LGN cells. The median is marked with a triangle. NLI was computed for the pixel that differed the background, based on the sum of the squared red, green, and blue pixel intensities.

4. FAST AND REVERSIBLE NEURAL INACTIVATION IN MACAQUE CORTEX BY OPTOGENETIC STIMULATION OF GABAergic NEURONS

4.1 ABSTRACT

Reversible optogenetic neural inactivation techniques are valuable for linking neural activity and behavior but they have serious limitations in macaques. To achieve powerful and temporally precise neural inactivation, we used an adeno-associated viral (AAV) vector carrying the channelrhodopsin-2 gene under the control of a Dlx5/6 enhancer, which restricts expression to GABAergic neurons. We tested this approach in the primary visual cortex, an area where neural inactivation leads to interpretable behavioral deficits. Optical stimulation modulated spiking activity and reduced visual sensitivity profoundly in the region of space represented by the stimulated neurons. Rebound firing, which can have unwanted effects on neural circuits following inactivation, was not observed, and the efficacy of the optogenetic manipulation on behavior was maintained across >1000 trials. We conclude that this inhibitory cell-type specific optogenetic approach is a powerful and spatiotemporally precise neural inactivation tool with broad utility for probing the functional contributions of different cortical areas in macaques.

4.2 INTRODUCTION

A major goal of systems neuroscience is to understand how neural activity mediates behavior. Neural inactivation techniques are central to this endeavor (Wurtz, 2015). However, these techniques can have unintended consequences that complicate data interpretation (Turrigiano, 1998; Stemmler, 1999; Abraham, 2008; Sokolova, 2008; Goold, 2010; Goshen, 2011). For example, by impairing task performance, neural inactivation can cause animals to explore new task strategies for acquiring reward. This change in strategy may change the information flow through neural circuits. To avoid these complications, inactivation methods are needed that can be reversed more quickly than these circuit-level changes can occur.

Optogenetics provides the fastest method for reversible neural inactivation currently available. In rodents, optogenetic inactivation has revealed links between neural activity and behavior that would have been difficult to discover with traditional, slower inactivation methods based on injection of pharmacological agents, cortical cooling or lesioning (Goshen, 2011; Hanks, 2015; Yartsev, 2018). Optogenetic inactivation has already been used in a few pioneering studies to perturb the behavior of macaque monkeys (Cavanaugh et al., 2012; Afraz et al., 2015; Acker et al., 2016; Fetsch et al., 2018). The approach taken in these studies was to reduce neuronal spiking by activating hyperpolarizing opsins (eNpHR, ArchT or Jaws). The directness of this approach facilitates the interpretation of behavioral effects. However, the behavioral effects produced this way have been small, perhaps because most promoters used in viral vectors drive expression in many neuronal types, and suppression of inhibitory neurons may counteract suppression of excitatory neurons.

An alternative approach, which has been successful in rodents, is to selectively activate inhibitory neurons with channelrhodopsin-2 (ChR2) (Glickfeld et al., 2013; Guo, 2014; Khan, 2018; Cone, 2019; McBride, 2019). This approach has two advantages. First, it is based on the opening of ion channels, which conduct more ions per photon absorbed than ion pumps. Second, it leverages the dense local connectivity and low synaptic failure rates of GABAergic neurons to suppress long-range excitatory signaling locally and robustly (Isaacson, 2011; Packer, 2011; Kubota, 2015; Wiegert et al., 2017).

To test the efficacy of this approach for cortical inactivation in macaques, we injected a viral vector with a cell-type-specific promoter (AAV–mDlx5/6–ChR2) into area V1 of three rhesus monkeys. This vector drives expression of ChR2 in GABAergic neurons in several animal models (Dimidschstein et al., 2016). In this study, we confirm the specificity of GABAergic neuronal transduction in macaque cortex and demonstrate that illumination of the injection site modulates spiking activity. We also show that illumination impairs visual sensitivity profoundly, reversibly and reliably at the receptive fields of the illuminated neurons but not outside. We conclude that optogenetic stimulation of inhibitory neurons is a powerful method for inactivating regions of the macaque monkey brain with high spatial and temporal precision.

4.3 METHODS

4.3.1 Experimental model and subject details

Three rhesus monkeys (*Macaca mulatta*) participated in this study (males; 7–14 kg). Two monkeys were surgically implanted with a head-holding device and a recording chamber that provided access to the primary visual cortex (V1). Surgical procedures, experimental protocols and animal care conformed to the NIH *Guide for the Care and Use of Laboratory Animals* and were approved by the Institutional Animal Care and Use Committee at the University of Washington.

Animal husbandry and housing were overseen by the Washington National Primate Research Center. All monkeys had ad-libitum access to biscuits (Fiber Plus Monkey Diet 5049, Lab Diet). Monkeys 2 and 3 had controlled daily access to fresh produce and water. When possible, animals were pair-housed and allowed grooming contact. Cages were washed every other week, bedding was changed every day, and animals were examined by a veterinarian at least twice per year.

During each experiment, monkeys viewed a CRT monitor binocularly with their heads fixed. The viewing distance was 100 cm for monkey 2 and 50 cm for monkey 3. Eye position signals were measured with an optical eye tracker for monkey 2 and a scleral search coil in monkey 3. Behavioral and stimulation timing events and eye position signals were digitized and stored for offline analysis (Horwitz and Hass, 2012).

4.3.2 AAV vector production

Recombinant AAV vectors were produced using a conventional three-plasmid transient transfection of human embryonic kidney cells (HEK293T, female, unauthenticated) with polyethylenimine (25 kDa, Polysciences). The transfer plasmid was pAAV-mDlx-ChR2-mCherry-Fishell-3 (Addgene #83898). Vectors were harvested and purified by ultracentrifugation through an iodixanol gradient column, exchanged into phosphate buffered saline (PBS), and titered using qPCR.

4.3.3 AAV vector injections

After mapping a track through V1 gray matter using standard extracellular recording techniques in awake fixating monkeys, we advanced an electrode and cannula to the deepest point of the track and began a series of injections. Using a Hamilton syringe attached to a manual pump, we injected 1.0–1.5 μl of AAV vector at each of several locations spaced 500 μm apart along a track (normal to the the opercular surface). Each injection was followed by a 2 min wait period after which the electrode and the cannula were slowly retracted to the next site. This process was repeated at 9–14 sites, and a total of 14–17 μl was injected along each track. In monkey 2, we injected 14 µL of AAV9–mDlx5/6–ChR2–mCherry (1.5×10^{13} genomes/ml) at each of the two opercular sites that were ~2 mm apart. The AAV vector was injected along 4 mm tracks throughout the thickness of the cortex for both the sites, in the left hemisphere. In monkey 3, we injected ~17 µL of AAV1–mDlx5/6–ChR2–mCherry (1.0×10^{13} genomes/ml) along a 5 mm track in the first site and 14 µL along a 6.5 mm track in the second site, in the right hemisphere, to target both opercular and calcarine regions of area V1. The two injection sites were ~1.5 mm apart.

4.3.4 Histology

We injected area V1 of a monkey 1 with AAV1–mDlx5/6–ChR2-mCherry to examine the specificity of vector transduction. These injections were performed during a surgical procedure while the monkey was anesthetized, and electrophysiological recordings were not made. The monkey recovered from the surgery and was euthanized 45 days later with an overdose of pentobarbital and perfused transcardially with 4% paraformaldehyde (wt/vol). The brain was removed, cryoprotected in 30% sucrose (wt/vol) and 50 µm-thick sections were cut on a sliding microtome. Fluorescence signals for mCherry (primary antibody: 1:250, Clontech 632543, mouse anti-mCherry; secondary antibody: 1:200, Invitrogen Molecular Probe) and parvalbumin (primary antibody: 1:5000, rabbit anti-PV, Swant 27; secondary antibody: 1:200, Invitrogen Molecular Probes) were detected immunocytochemically. Sections were counter-stained with DAPI (1:5000, Molecular Probes D-21490) and cover-slipped using a DABCO-based mounting medium.

4.3.5 Neurophysiology

Three to four weeks after AAV injections in monkeys 2 and 3, we searched for neuronal responses to blue light (450 nm; 33–161 mW) delivered to area V1 via an optical fiber (300 µm outer diameter; Thor Labs) with a beveled tip that eased entry through the dura. A fiber and a glass-coated tungsten electrode (1-3 MΩ FHC) were placed in a common guide tube and lowered independently into the brain by microdrive (Narashige or Alpha-Omega). Extracellular spiking activity was amplified (1x head-stage), high-pass

filtered (250Hz cutoff), digitized (sampling rate of 40 kHz) and sorted (Plexon MAP system or Cambridge Electronics Design Power 1401 system).

4.3.6 Site selection criteria

Stimulation sites were selected by inserting an electrode into V1 and finding a region with vigorous visual activity and a clearly defined receptive field (RF). The optical fiber was then lowered while repeatedly delivering brief laser pulses. The optical fiber typically lagged the electrode by 100–500 μm. Only sites at which optical stimulation produced an audible change in firing rate were tested.

4.3.7 Laser Setup

The laser was developed in-house by the Bioengineering Core at the Washington National Primate Research Center. Light was generated by a laser diode (part # PL TB450B). Light delivery was modulated by modulating the current to the laser diode (digital to analog converter part # AD5683) not by shutter.

4.3.8 Visually guided saccade task

Monkeys were trained to make saccades to visual targets 4–17° from the fixation point. Each trial began when the monkey acquired a central fixation point (0.2–0.3° sided square) within a 1.6 × 1.6° electronic window. Then, 13 ms after the central target disappeared, a saccade target (square with sides 0.3–0.4°) was presented. Two to ten target locations, equiangularly spaced at fixed radius, were interleaved within each block of trials. Monkeys were rewarded for making a saccade to the target. On half of the target-present trials (at each location), a 300 ms laser pulse was delivered concomitantly with the target presentation (**Figure 4.4B**). We interleaved 10–30 catch

trials in which no target was presented, and the monkey was rewarded unconditionally. Optical stimulation was delivered on half of the catch trials, immediately after the fixation point disappeared.

4.3.9 Two-alternative forced choice (2AFC) Gabor contrast detection task

Monkeys were trained to detect a Gabor stimulus positioned at 4–17° from the fixation point. Each trial began when the monkey acquired the central fixation point. Then, after a 520 ms delay, a drifting Gabor stimulus appeared on half of the trials (spatial frequency = 1 cycle/°, temporal frequency = 8 Hz, standard deviation = 0.2°, duration = 200 ms). Immediately after the Gabor stimulus disappeared, a pair of targets appeared along the horizontal meridian, 2° from the fixation point. A saccade to the target on the same side of the screen as the Gabor stimulus was rewarded on Gabor-present trials, and a saccade to the target on the opposite side was rewarded on Gabor-absent trials.

The Gabor stimulus appeared inside the RF of neurons at the recording site in all trials except a few to test the retinotopic specificity of the optogenetic effect (**Figure 3.6**). Optical stimulation began at the stimulus onset, lasted 300 ms (**Figure 3.5B**), and was delivered on half of the Gabor-present and half of the Gabor-absent trials. The monkey typically performed several blocks of trials per session, each consisting of 120 trials. Stimulus strength was adjusted by independent contrast staircase procedures on laser and control trials. Contrast, defined as the difference between the highest and the lowest luminance intensities, divided by the sum of the two, increased by a factor of 1.18–1.33 following an incorrect response and decreased by a factor of 0.75–0.85 following three consecutive correct responses.

4.3.10 Sensitivity index (d')

Sensitivity (*d')* was measured using a standard formula from signal detection theory (Green and Swets, 1966; Macmillan, 2004).

$$d' = \Phi^{-1}(\text{proportion of hits}) - \Phi^{-1}(\text{proportion of false alarms})$$

In this equation, Φ^{-1} is the inverse normal cumulative distribution function. Proportions of 0 were replaced with $0.5/n$, and proportions of 1 were replaced by $1-(0.5/n)$, where n is the number of Gabor-present (for hits) or Gabor-absent trials (for false alarms) (Stanislaw, 1999).

4.3.11 Fit to behavioral data

Psychometric functions were fit with a cumulative Weibull distribution function by maximizing likelihood assuming binomial error. Fitting was performed using the inbuilt MATLAB *fmincon* function. Detection threshold was defined as the luminance contrast corresponding to 82% correct task performance.

4.4 RESULTS

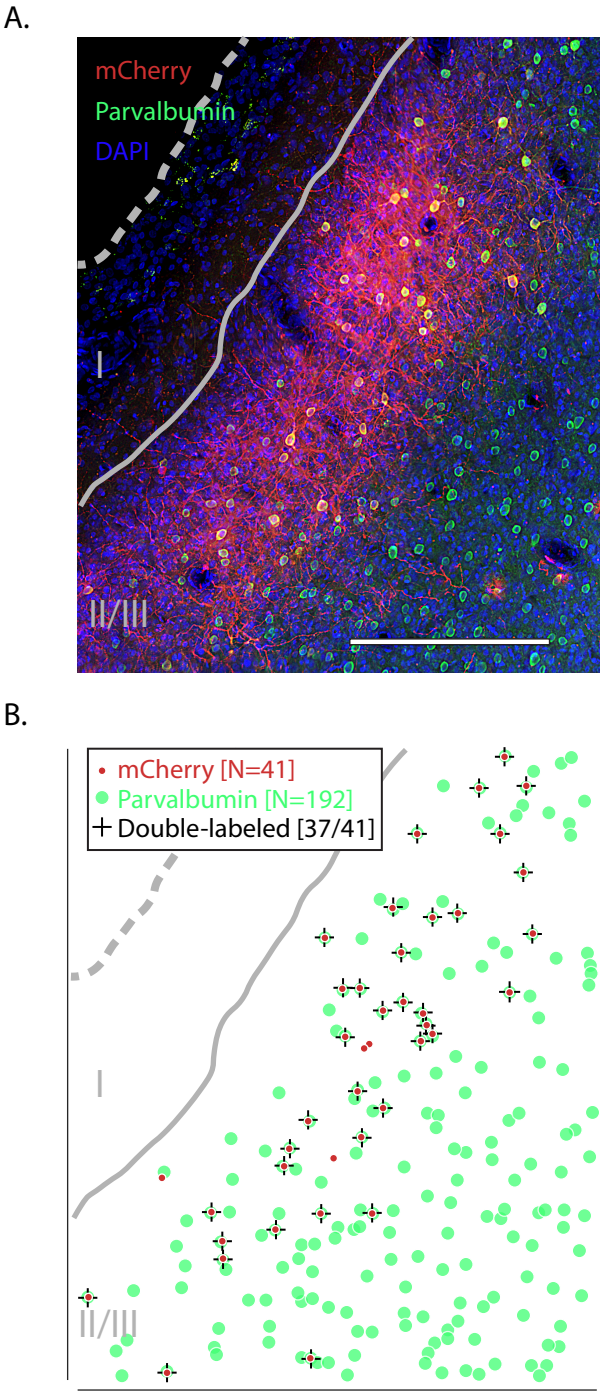

Figure 4.1. Immunohistochemical analysis of transduction by AAV1-mDlx5/6-ChR2-mCherry. **(A)** A histological section of V1 from monkey 1 stained with DAPI (blue) and antibodies against parvalbumin (green) and mCherry (red). Scale bar is 250 µm. The pial surface is indicated by the dashed gray curve and the border between layer 1 and 2/3 is indicated by the solid gray curve. The laminar specificity is an idiosyncrasy of this particular injection; see **Figure S4.1** for a histological section of the V1/V2 border. **(B)** Locations of cell bodies in **(A)** expressing mCherry (red), parvalbumin (green) or both ("+").

4.4.1 Selectivity of opsin expression

A previous study showed that an AAV vector carrying the gene for the fluorescent reporter, GFP, under the control of the mDlx5/6 enhancer transduced V1 GABAergic neurons in a marmoset with 93% selectivity (Dimidschstein et al., 2016). To determine whether AAV–mDlx5/6–ChR2–mCherry has similar selectivity in macaque, we injected V1 of one animal (monkey 1) and examined the tissue histologically (**Figure 4.1 & Figure S4.1**). The visualized mCherry-positive cells had non-pyramidal morphologies, consistent with them being GABAergic. Similar histological results with this viral vector have been presented in macaques previously (V. E. Scerra, 2019).

Most mCherry-positive neurons co-expressed parvalbumin (468/543), a marker for 75% of GABAergic neurons in macaque V1 (Van Brederode, 1990). This high level of co-expression is consistent with selective transduction of GABAergic neurons and is sufficiently high to suggest that parvalbumin-positive neurons may be transduced with particularly high efficiency ($p<0.005$; binomial test).

4.4.2 Optogenetic control of neural activity

To test whether ChR2 expression was sufficiently strong to perturb neural activity, we recorded extracellular spiking responses from single- and multi-units near the injection sites in two other monkeys (monkeys 2 and 3) while they performed a contrast detection task. Most sites were visually driven (46/56, response to a low-contrast Gabor stimulus > baseline firing rate; 19/56, $p<0.05$; Mann-Whitney U test). Given our selection criteria, all sites were significantly modulated by optical stimulation ($p<0.06$; Mann-Whitney U test; see Methods). Some units were excited by optical stimulation (450 nm laser light)

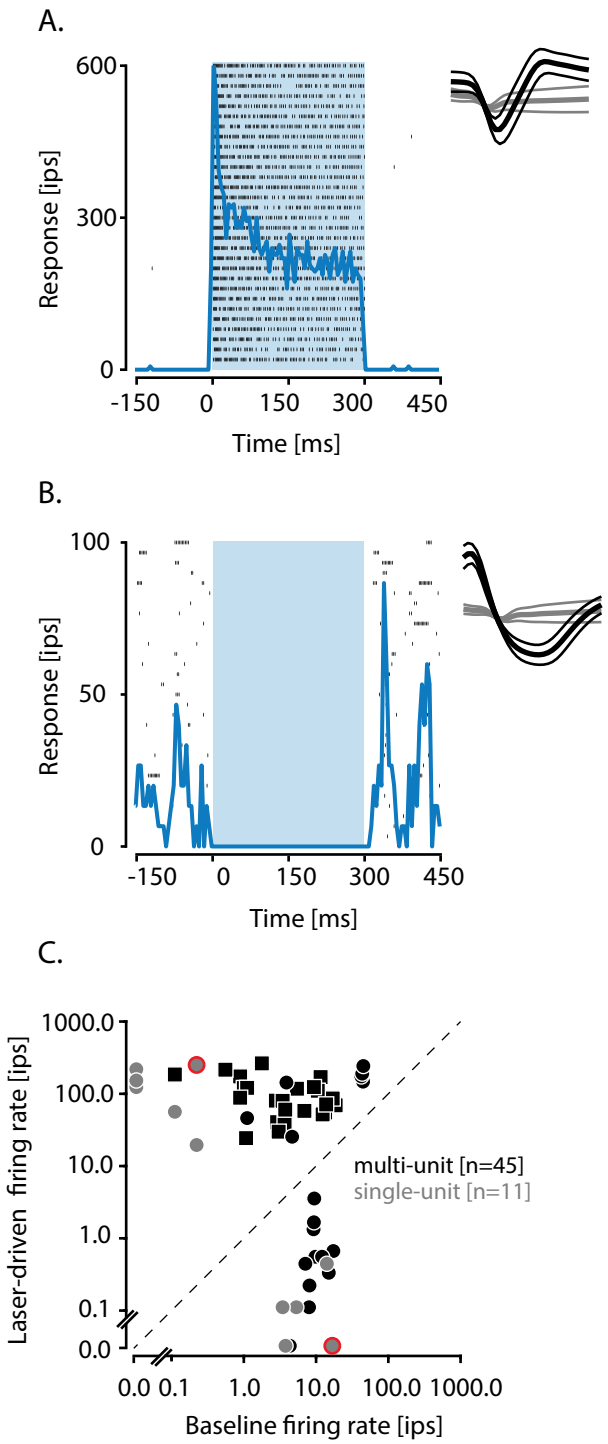

Figure 4.2. Optogenetic activation and suppression of single- and multi-units. **(A,B)** Responses (in impulses per second, ips) of two example single units, aligned to the onset of optical stimulation, which lasted 300 ms (blue rectangle). Rasters (tick marks) and peristimulus time histograms (blue traces) are shown for an activated single-unit **(A)** and a suppressed singleunit **(B)**. Insets: Mean spike waveform (thick black curve) and noise waveform (thick gray curve) ± 1 standard deviation (thin curves). **(C)** Scatter plot of firing rate on laser trials against baseline firing rate of units from monkey 2 (square) and monkey 3 (circle). Data from example activated and suppressed units are circled in red. Firing rates were computed during optical stimulation or the equivalent epoch on control trials.

(**Figure 4.2A**) whereas others were suppressed (**Figure 4.2B**). At 38 of the 56 sites studied, optical stimulation increased spiking. The prevalence of excitation in our dataset is likely because we searched for sites where optical stimulation produced an audible change in the baseline firing rate (**Figure 4.2C)**. The mean latency to response was 14±26 (SD) ms and was < 5 ms at 11 sites (**Figure S4.2**). Neurons excited at short latency (< 5 ms) presumably expressed ChR2 and suppressed other neurons via synaptic inhibition.

Neural activity suppression using halorhodopsins in monkeys is typically followed by a rebound of activity at the termination of optical stimulation (Acker et al., 2016; Fetsch et al., 2018). We did not observe such rebounds with AAV–mDlx5/6–ChR2. We compared average firing rates at 18 suppressed sites in a 50 ms window before and after optical stimulation. At one example site, the pre-laser firing rate exceeded the post-laser firing rate (22 vs 0 impulses/sec, $p<0.001$, Wilcoxon sign rank test, **Figure 4.3A**), consistent with sustained suppression. At a different example site, the pre-laser firing rate was lower than the post-laser firing rate, consistent with a small rebound (10 vs 25.33 impulses/sec, $p=0.02$, Wilcoxon sign rank test, **Figure 4.3B**). Such rebounds were rare; post-laser firing rates exceeded pre-laser firing rates at only 2 of 18 sites (**Figure 4.3C**).

Activity at most suppressed sites recovered to baseline levels gradually after laser termination. We measured this recovery time by computing the first time at which the average spike count in a 50 ms sliding window returned to 90% of the pre-laser firing rate. Recovery times ranged from 0 to 215 ms (**Figure 4.3D**) with roughly half of the sites recovering within 100 ms (median = 97.5 ms). These data demonstrate that

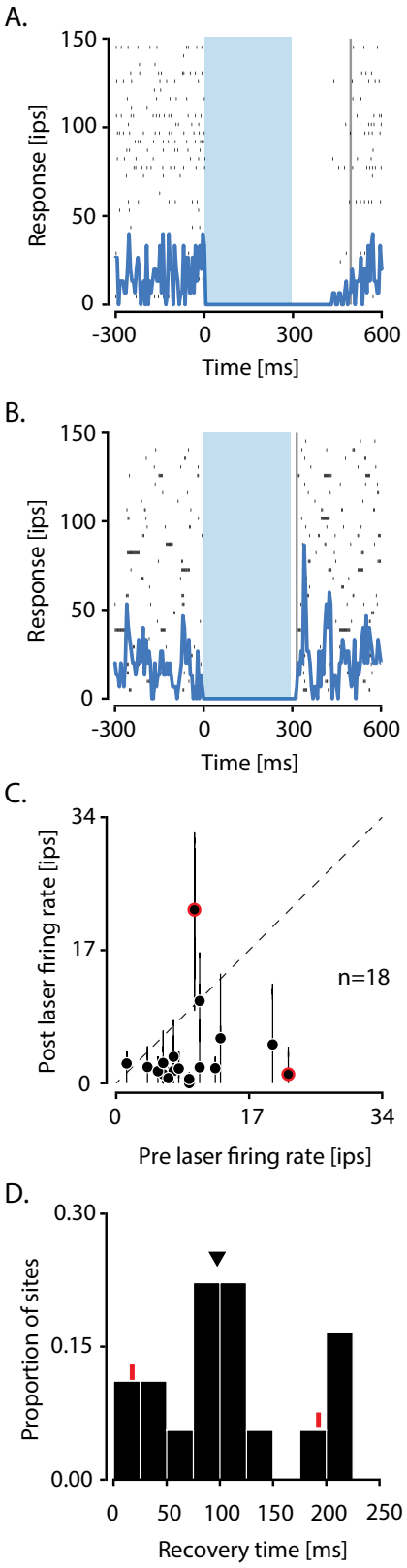

Figure 4.3. Analysis of activity rebound and recovery at suppressed sites. **(A)** Responses of a single-unit where the pre-laser firing rate exceeded the post-laser firing rate. Recovery time to the baseline firing rate was 195 ms (vertical gray line). **(B)** Responses of another single-unit where the post-laser firing rate exceeded the pre-laser firing rate. Recovery time was 15 ms. **(C)** Scatter plot of pre-laser firing rates against post-laser firing rates. For each site, post-laser firing rate was computed in a sliding 50 ms window from 0–200 ms after the laser was terminated. The ranges of post-laser firing rates are plotted as black lines and averages are plotted as black points. Data from neurons in **(A)** and **(B)** are circled in red. **(D)** Histogram of recovery times following optogenetic suppression. Recovery times of example units are marked with red tick marks, and the median is marked with a triangle.

suppression persists several tens of milliseconds after laser termination.

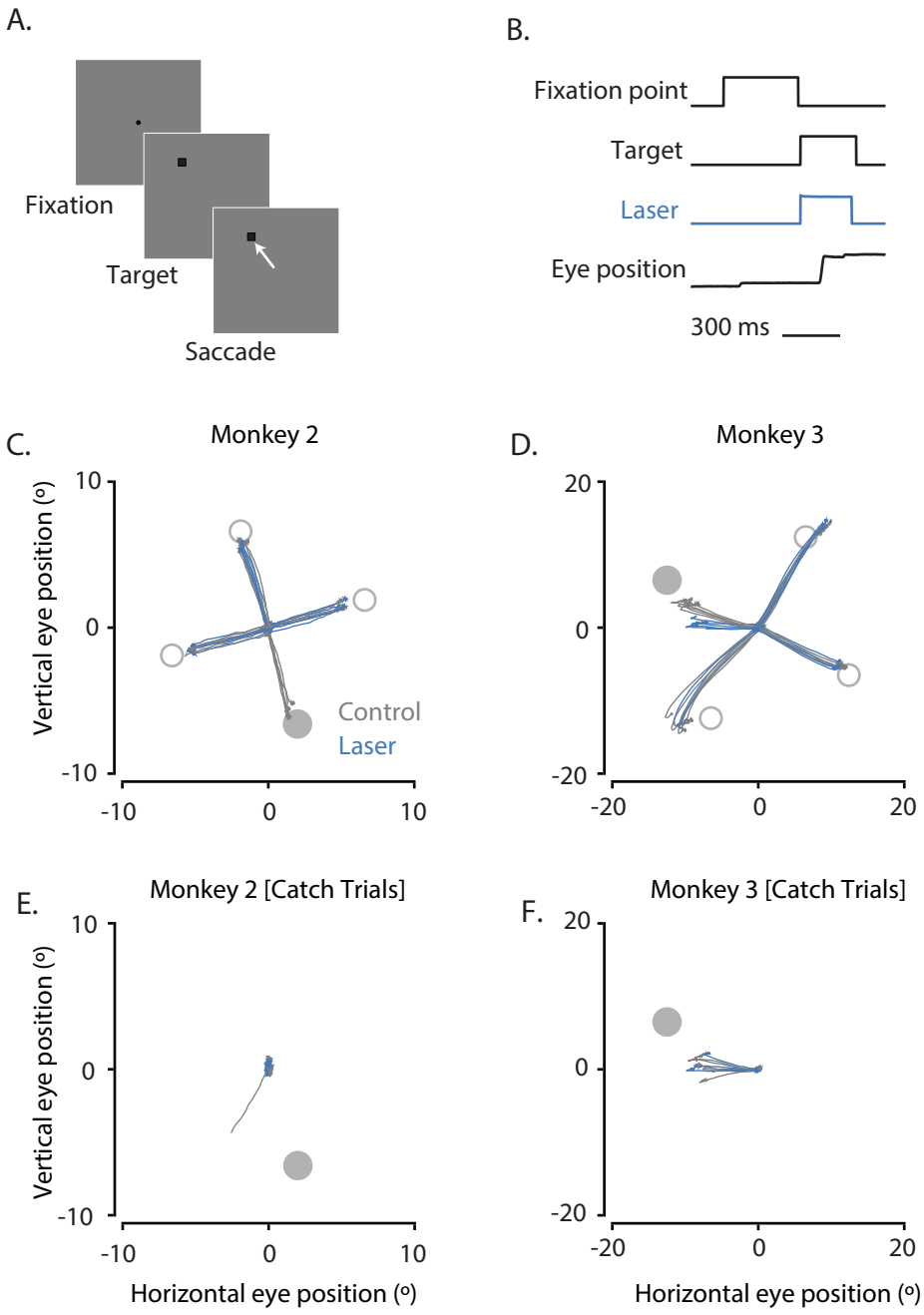

Figure 4.4. Effect of optogenetic inactivation of V1 on visually guided saccades. **(A)** Task design. **(B)** Timing of events. The small overshoot in the laser trace accurately reflects the temporal profile of the light. **(C,D)** Eye position traces on control (gray) and laser (blue) trials are shown from 0–300 ms after the fixation point was extinguished for one block of trials. The RF location of the illuminated neurons (gray filled circle) and the target locations outside the RF (gray open circle) are highlighted. **(E,F)** Eye positions on catch trials from the same blocks shown in **(C,D)**.

4.4.3 Optogenetic control of behavior

We trained monkeys 2 and 3 to perform two visually demanding behavioral tasks to evaluate the behavioral efficacy of optogenetic stimulation. Reward contingencies were independent of laser stimulation in both tasks.

In the visually guided saccade task, a target appeared inside the RFs of the stimulated V1 neurons on a random subset of trials and outside on other trials (**Figure 4.4A–B**). Data from an example block of trials from each monkey demonstrate the main results (**Figure 4.4C–D**). On control trials from this block, both monkeys made accurate saccades to most target locations. On laser trials, the monkeys failed to make saccades into the RFs of the optically stimulated neurons. Saccades were unaffected when the target appeared at other locations indicating that the optogenetic effect was retinotopically specific. On laser trials when the target appeared inside the RFs, monkey 2 typically maintained fixation, and monkey 3 typically made leftward ~10° saccades. Similar behaviors were observed on catch trials in which no target was shown (**Figure 4.4E–F, see Materials & Methods**).

We collected data in 10 sessions from monkey 2 (16 blocks of trials) and 7 sessions from monkey 3 (20 blocks of trials). Within each session, we calculated the distance between the saccade end points and target locations. When the target appeared inside the RFs of stimulated neurons, the saccade end points tended to be closer to the target on control trials than on laser trials ($p<0.002$ for monkey 2, $p=0.03$ for monkey 3; Wilcoxon signed rank tests). When the target appeared in other locations, the saccade endpoints were similarly close to the target on control and laser trials ($p=0.92$ for

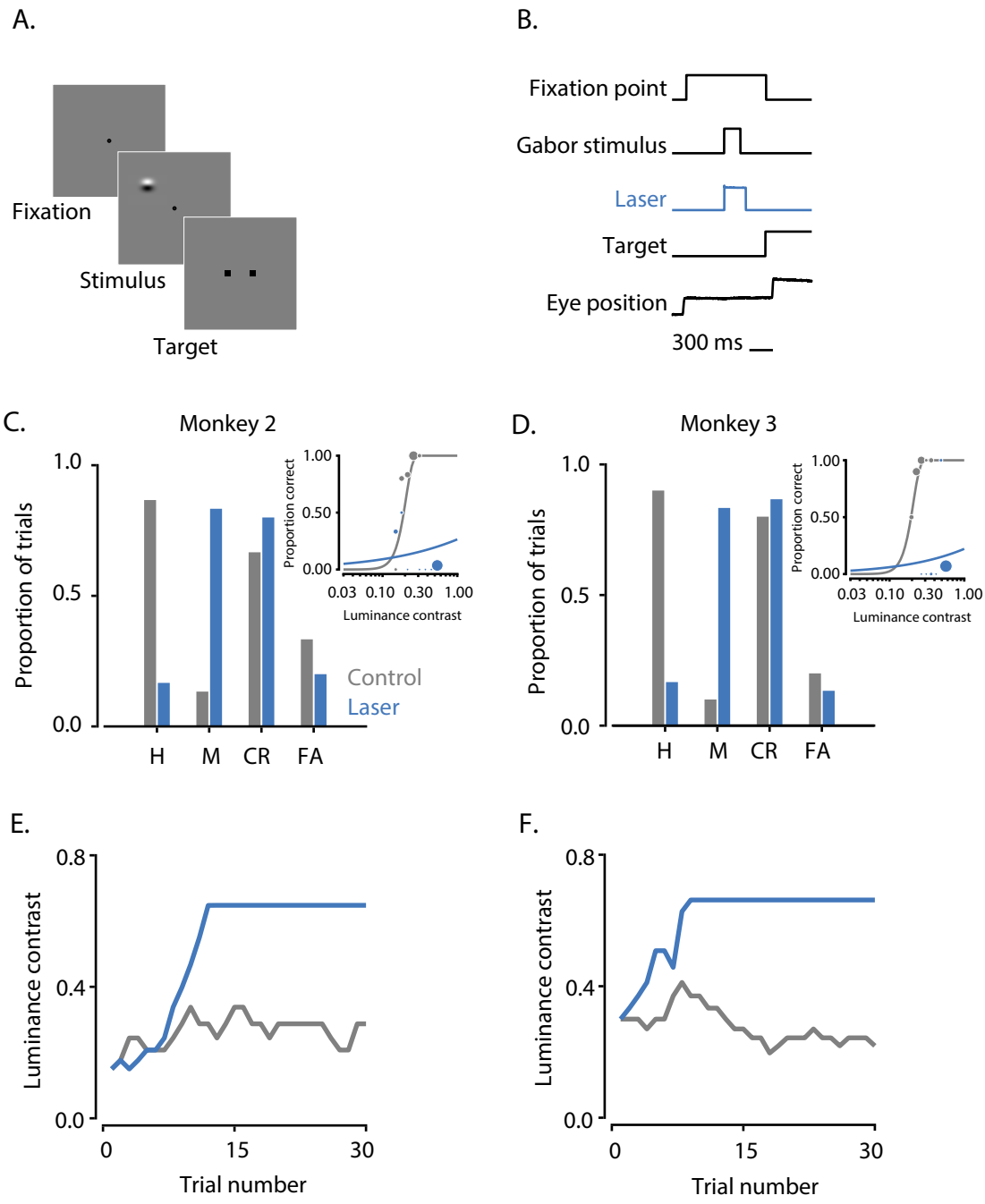

Figure 4.5. Effect of V1 inactivation on visual contrast detection. **(A)** Task design. **(B)** Timing of events. The small overshoot in the laser trace accurately reflects the temporal profile of the light. **(C)** Performance of monkey 2 over one block of trials. Hits (H) and misses (M) are proportions of Gabor-present trials that were answered correctly and incorrectly, respectively. Correct rejections (CR) and false alarms (FA) are proportions of Gabor-absent trials that were answered correctly and incorrectly, respectively. Insets show psychometric functions on control (gray) and laser (blue) trials. Symbol size in insets reflects the number of trials that contributed to each data point. **(E)** Contrasts selected by the staircase procedure on control (gray) and laser (blue) trials. **(D,F)** Performance of monkey 3 in the same format as **(C,E)**. Luminance contrast could not exceed 0.66 because the gray background was close to the upper limit of the display range.

monkey 2, p=0.38 for monkey 3; Wilcoxon signed rank tests; **Figure S4.3 A–B**). Saccade latencies were greater on laser trials than on control trials when targets were inside the RFs (p<0.0001 for monkey 2 & 3; Mann-Whitney U test; **Figure S4.3 C–D**) but not when targets were elsewhere (p=0.90 for monkey 2 & p=0.41 for monkey 3; Mann-Whitney U tests; **Figure S4.3 E–F**).

To confirm that the deficit in task performance was not purely oculomotor, we trained monkeys 2 and 3 to perform a contrast detection task that required saccades to targets outside the RFs of the stimulated neurons (**Figure 4.5A–B: see Materials & Methods**).

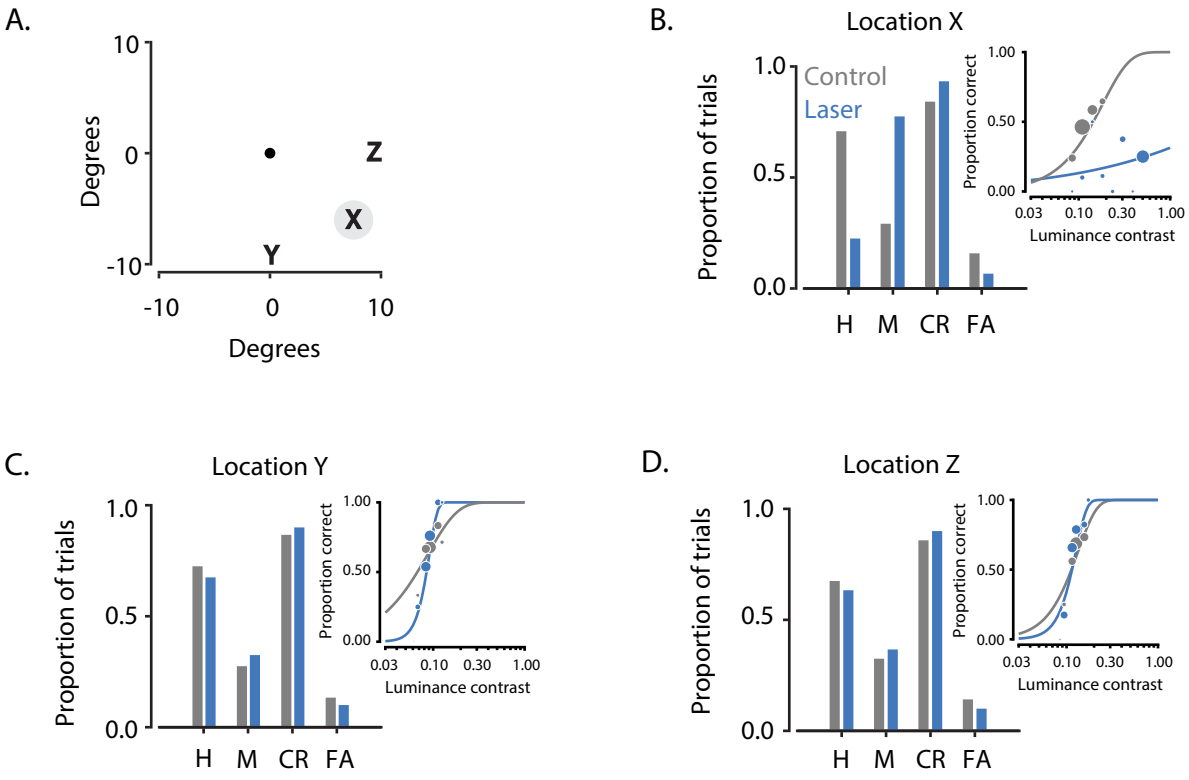

Figure 4.6. Retinotopic specificity of optogenetic effects on contrast detection. Data are from a single session consisting of 4 blocks of trials from monkey 2. **(A)** On each trial, the Gabor stimulus appeared at one of three randomly-interleaved locations (X, Y, or Z), all of which were 9.6° away from the fixation point (central black dot). Locations Y and Z were on the vertical and horizontal meridians, respectively. **(B)** The proportions of hits (H), misses (M), correct rejections (CR) and false alarms (FA) are plotted in the same format as in **Figure 4.5C**. The laser reduced the monkey's contrast sensitivity when the Gabor stimulus appeared at the receptive fields of the transduced neurons (X, gray circle). No significant effect was observed at locations Y and Z **(C,D)**.

An example block of trials from each monkey demonstrates the main results. Both monkeys detected the visual stimulus more frequently on control than on laser trials (proportion of hits on control vs. laser trials; $p<0.001$ for monkey 2 and monkey 3; binomial test for equality of proportions; **Figure 4.5C–D**). This performance deficit was also reflected in the psychometric functions (**Figure 4.5C–D inset**) and in the contrast values selected by the staircase procedure (**Figure 4.5E–F**). Neither monkey was able to detect the visual stimulus with above-chance accuracy on laser trials even at the maximum stimulus contrast achievable. Saccades to the stimulus location were never required, and thus the behavioral effects produced by optical stimulation in this task cannot be explained by an oculomotor deficit.

In one session, the Gabor stimulus location was randomized across trials, confirming the retinotopic specificity of the effect (**Figure 4.6**). Additional control experiments confirmed that the monkeys were able to make saccades to both target locations irrespective of optical stimulation (data not shown) and showed that performance on control trials was unaffected by the interleaved laser trials (**Figure S4.4**).

We collected data in 11 sessions from monkey 2 (69 blocks of trials) and 12 sessions from monkey 3 (81 blocks of trials). In almost every session (10/11 in monkey 2, 11/12 in monkey 3), the proportion of hits on control trials was significantly greater than on laser trials (binomial tests for equality of proportions, $p<0.05$, **Figure 4.7A–B**). An analysis of sensitivity indices (d') confirmed that this change in performance was consistent with a reduction in sensitivity and inconsistent with a pure change in criterion (**Figure 4.7C–D**). In most blocks of trials (52/69 in monkey 2 and 63/81 in monkey 3),

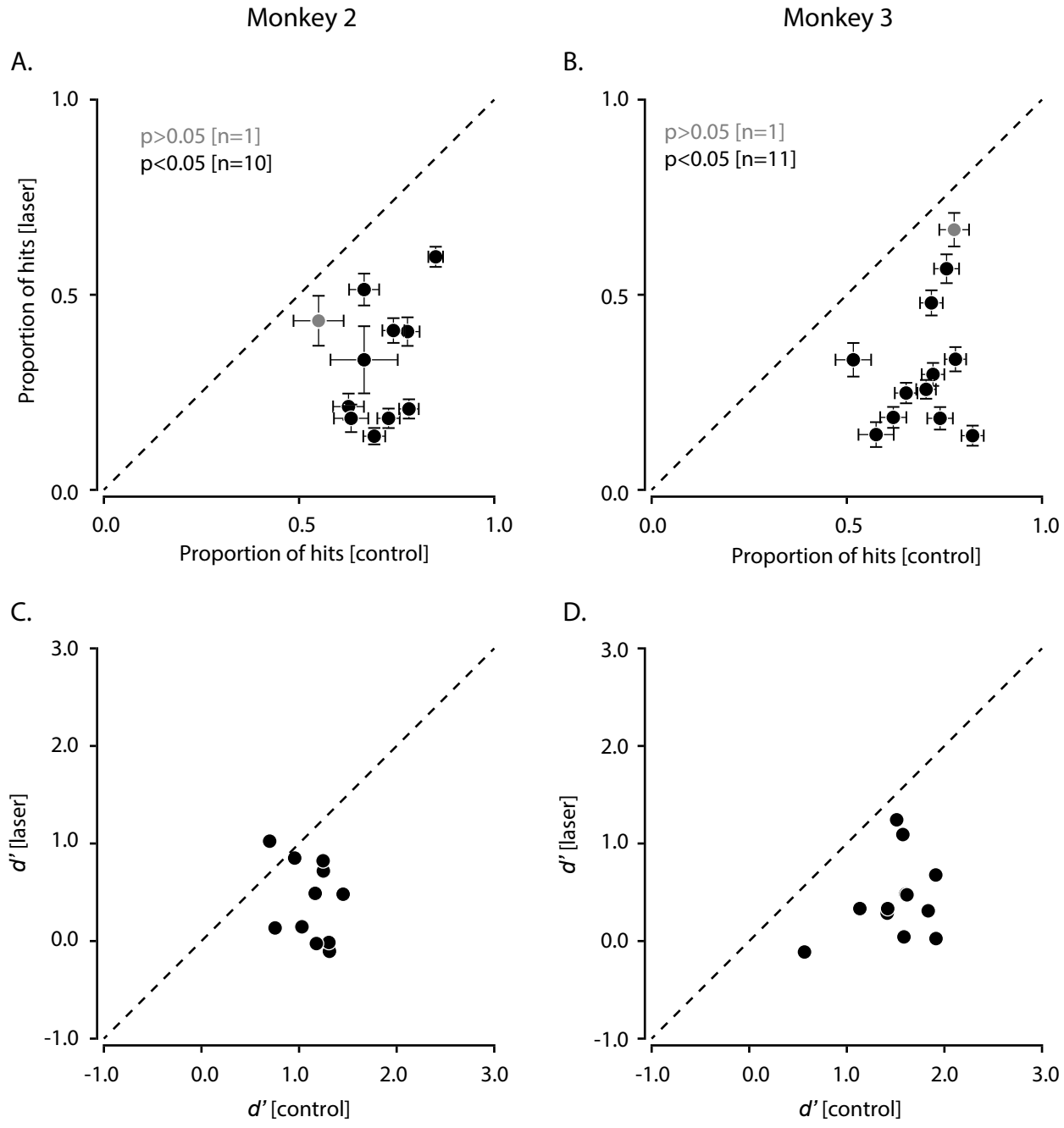

Figure 4.7. Effect of V1 inactivation on visual contrast detection across multiple sessions. **(A)** Scatter plot showing proportion of hits on control trials against laser trials from each session in monkey 2. Sessions with significantly fewer hits on laser trials than control trials are shown in black ($p < 0.05$, binomial test for equal proportions). Error bars represent the standard error of mean. **(B)** Data from monkey 3 in the same format as in **(A)**. **(C)** Scatterplot of *d'* from control trials plotted against *d'* from laser trials from each session performed by monkey 2. **(D)** Data from monkey 3 in the same format as **(C)**.

optical stimulation increased detection thresholds beyond the limits of the display, an event that occurred rarely on control trials (0/63 blocks in monkey 2, 8/81 blocks in monkey 3).

As laser power increased, errors became more common which caused the staircase procedure to increase the stimulus contrast rapidly (**Figure 4.8A**). The magnitude of the behavioral effect increased steeply with laser intensity between 12.8 and 22.3 mW and saturated by 30.0 mW (**Figure 4.8B**). Behavior on control trials was not affected by changes in laser power (r=-0.37, p=0.41; Pearson's correlation between *d'* on control trials from each block and laser power).

Optogenetic modulations of neural activity were tightly coupled to effects on behavior across these trials (r=0.61, p=0.17; Spearman's correlation between neural laser modulation index and difference in *d'* between control and laser trials; **Figure S4.5**). Pooling data across all blocks of trials reduced the correlation (r=0.16, p=0.23). Pooling the data reduced statistical power due to covariates across blocks of trials that exerted different effects on neurophysiological and behavioral outcomes (e.g. fiber position, stimulus location in the visual field, and quality of neural recordings). These covariates were held fixed in the data shown in **Figure 4.8A–B**.

In a previous study, the behavioral effects produced by optogenetic silencing of neurons in area MT using the suppressive opsin, Jaws (red shifted cruxhalorhospsin), decreased over tens of minutes (Fetsch et al., 2018). To determine whether a similar phenomenon occurred with ChR2-mediated inactivation, we analyzed 4 experimental sessions (28

blocks of trials) from monkey 2 and 5 sessions (33 blocks of trials) from monkey 3. From these sessions, we analyzed the subset of blocks with identical laser power.

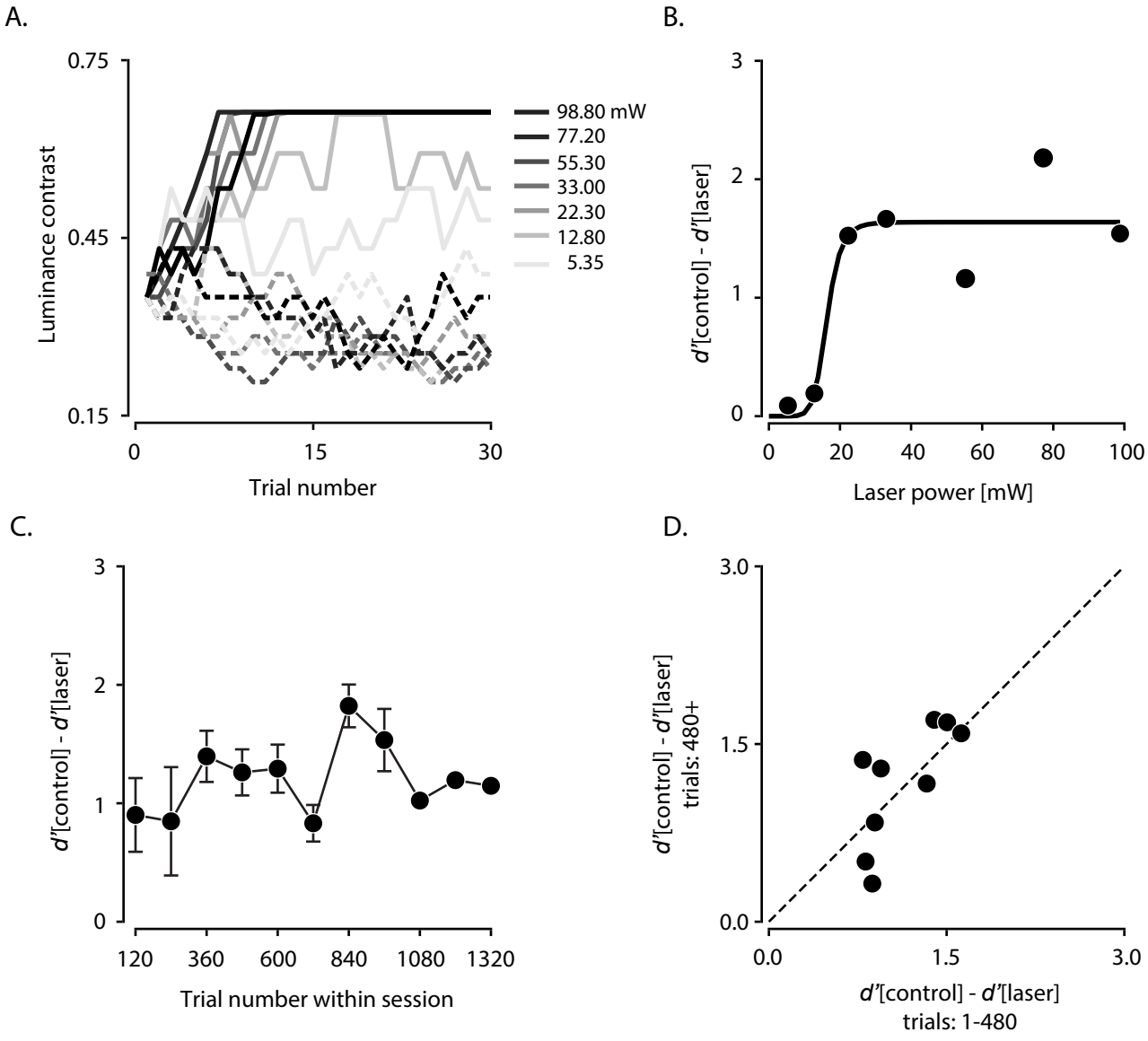

Figure 4.8. Effect of laser power and repeated optical stimulation on contrast detection. **(A)** Contrast values selected by the staircase procedure on laser trials (solid lines) and interleaved control trials (dashed lines) across seven blocks. **(B)** The difference in *d'* between control and laser trials as a function of laser power calculated from the data in **(A)**. A Naka-Rushton fit to the data is shown in black. **(C)** Differences in *d'* between control and laser trials as a function of trial number in each session. Each session consisted of at least five blocks of 120 trials. The duration of an individual trial was 2.80±0.51s (mean±SD), and the number of trials per session was 813±253. Points are means and error bars are standard error of the mean (SEM). SEM was not plotted for the final two points, each of which represent data from a single session. **(D)** Scatter plot of the differences in *d'* for early trials (1–480) vs. late trials (480–beyond) within each session.

The behavioral effects we observed were consistently large over the course of ~1000 trials (or ~50 mins). We quantified the behavioral effect as the difference in *d'* between laser and control trials within each block. The behavioral effect varied little as a function of block number, (r=0.25, p=0.45; Pearson's correlation between block number and *d'* averaged across sessions; **Figure 4.8C**). It was also consistent within individual sessions; linear regression slopes of the behavioral effect as a function of block number in each session did not differ significantly from zero (p=0.57, Student's t-test). For comparison with previous work (Fetsch et al., 2018), we calculated the behavioral effect in early and late trials within each session. Unlike the previous work, the behavioral effect did not differ between the first 480 trials (4 blocks) and the subsequent trials suggesting the absence of compensatory changes under the conditions of the current study (p=0.79, Student's t-test, **Figure 4.8D).**

4.5 DISCUSSION

The fast activation and inactivation of neurons afforded by optogenetics has revolutionized our understanding of the nervous systems of rodents and invertebrates. Understanding the primate brain at a similar level of detail is facilitated by optogenetics in the macaque monkey—a model organism with a brain structure similar to humans that can be trained to perform complex behavioral tasks. Rapid activation was already feasible in primates using microsimulation, and now rapid inactivation is too.

We achieved inactivation by stimulating GABAergic neurons in macaque V1 and measured electrophysiological and behavioral consequences. We first showed that the AAV–mDlx5/6–ChR2 vector targeted ChR2 expression to GABAergic neurons in area V1. Second, we showed that optical stimulation modulated the activity of neurons near the injection site. Third, we showed that optical stimulation impaired visual sensitivity in two behavioral tasks. The reduction in behavioral sensitivity was specific to trials in which optical stimulation was delivered and to the RF location of the stimulated neurons, demonstrating the temporal and spatial precision of the inactivation. Laser-induced modulations of neural responses were rapid, rebound activity following light pulses was negligible, and behavioral effects were consistent across ~1000 trials.

Below, we compare the results of our study with those of previous studies that used optogenetic neural inactivation to perturb macaque behavior. We then discuss the optogenetic stimulation of V1 on eye movements and ways in which the method could be improved. Finally, we discuss potential applications of AAV–mDlx5/6–ChR2 for understanding primate brain function.

4.5.1 Comparison with optogenetic inactivation studies

Four previous studies used optogenetic inactivation to perturb monkey behavior (Cavanaugh et al., 2012; Afraz et al., 2015; Acker et al., 2016; Fetsch et al., 2018). The two studies most similar to ours quantified the effect of neural inactivation on behavior as changes in visual discrimination thresholds on 2AFC tasks (Afraz et al., 2015; Fetsch et al., 2018). In one study, inactivation of inferotemporal cortical neurons raised thresholds for classifying face stimuli on the basis of gender (Afraz et al., 2015). In the other, inactivation of MT cortical neurons biased judgements of visual motion direction (Fetsch et al., 2018). In both cases, threshold changes were smaller than those we observed (~5% vs >100%, **Figure 4.7**).

The threshold changes we observed were large potentially for several reasons. First, we excited ChR2-expressing inhibitory neurons to reduce the spiking of excitatory neurons. Stimulation of a small number of inhibitory neurons can suppress activity of a large number of excitatory neurons (Wiegert et al., 2017). Second, we used ChR2, which conducts more ions per absorbed photon than ion pumps (Jaws & ArchT) and hence is more efficient. Third, we used higher laser power (4–160 mW vs. ~2 mW & ~12 mW; **Figure 4.4–4.8**). Fourth, we inactivated area V1, an area that is indispensable for the behaviors we studied (Koerner, 1973; Merigan, 1993; Radoeva, 2008). Higher-order visual cortical areas may be sufficiently interconnected to allow one or more areas to compensate for others with regard to the behaviors tested. An intriguing, and now-testable, hypothesis is that the spared visual sensitivity following visual cortical lesions

is due to the engagement of slow compensatory mechanisms, not the unmasking of normally functioning pathways (Leopold, 2012).

We interpreted the laser-induced change in the monkeys' performance as a change in sensitivity, and it is inconsistent with a change in criterion alone. Additionally, the brevity and unpredictability of the optical stimulation makes large, consistent, selective changes in criterion on laser trials unlikely. Nevertheless, we cannot rule out the possibility that the optical stimulation affected sensitivity and criterion concomitantly.

4.5.2 Comparison with non-selective optogenetic stimulation of V1

Illumination of ChR2-expressing neurons in area V1 causes monkeys to make saccades into the RFs of the stimulated neurons under some conditions (Jazayeri et al., 2012). This behavior is consistent with the perception of a phosphene (Tehovnik et al., 2003). In our study, however, monkeys rarely made saccades into the RFs of the stimulated neurons, suggesting that they did not experience a phosphene. This result held on trials requiring a saccade to a visual target inside the RFs of the stimulated neurons and on trials in which no target was shown, a condition similar to the key condition in the study of Jazayeri et al. (2012). In principle, detection of the optical stimulation could have provided a cue for acquiring reward in the visually guided saccade task. Having sensed the optical stimulation, and seen no target, the monkey could have increased its reward rate by making a saccade into the RFs of the stimulated neurons. The fact that the monkeys did not behave this way suggests that they were unable to detect the stimulation, or at least were unable to use it to direct saccades. Sensing the optical

stimulation would not have been not useful for increasing reward rate in the contrast detection task.

We attribute the difference between studies to the population of V1 neurons stimulated. We used a Dlx5/6 enhancer to express ChR2 selectively in inhibitory neurons whereas Jazayeri et al. (2012) used the human synapsin I promoter, which drives expression in both excitatory and inhibitory neurons (Nathanson et al., 2009). One hypothesis is that phosphenes are caused by spikes in a subset of excitatory projection neurons. In this case, pan-GABAergic stimulation would not be expected to produce phosphenes, but stimulation of specific GABAergic subtypes might. For example, stimulation of VIP-expressing neurons might produce a phosphene through disinhibition of excitatory neurons (Cone, 2019).

4.5.3 Effect of laser power and optical fiber insertion on brain

Over the course of this study, both monkeys 2 and 3 developed scotomas in areas of the visual field corresponding to the regions of V1 inactivated. The brains of these animals have not yet been analyzed histologically, but it is likely that areas of V1 in both monkeys were damaged. This damage could be due to thermal trauma caused by light and/or mechanical trauma caused by repeated penetrations by optical fibers.

The laser power used in the current study spanned a broad range (4–160 mW for 200–300 ms) and, on an average, was higher than many behavioral studies (Cavanaugh et al., 2012; Gerits et al., 2012; Ohayon et al., 2013; Dai et al., 2014; Afraz et al., 2015; Inoue et al., 2015; Stauffer, 2016; El-Shamayleh et al., 2017; Tamura, 2017; Fetsch et

al., 2018). Given the stimulation parameters we used, (450 nm light conducted through 300 μm-diameter optical fibers), we likely heated tissue near the fiber tip by several °C in many of our experiments (Arias-Gil, 2016). Heating can lead to unwanted increments or decrements of activity in specific kinds of neurons and aberrant behavior (Moser, 1993; Long, 2008). However, the consistency of the behavioral effect within individual sessions after repeated optical stimulation argues against acute damage (**Figure 4.8C–D**). Nevertheless, heating can cause permanent tissue damage and might have contributed to the development of scotomas over the course of this study (Thomsen, 1991).

The tissue damage produced by optogenetic manipulations can be mitigated by using artificial dura (Nandy, 2019; Ruiz et al., 2013) and red-shifted or step-function opsins (Berndt et al., 2009). Artificial dura allows non-invasive optical stimulation of the superficial cortical layers, reducing mechanical damage. Red-shifted opsins are activated by long-wavelength light, which heat neural tissue less and thus cause less thermal damage than short-wavelength light do. The neural activity produced by step-function opsins outlast the light pulses required to trigger them, allowing brief, safe light pulses to produce longer lasting stimulation events.

4.5.4 Potential applications of AAV–mDlx5/6–ChR2

Optogenetic stimulation of inhibitory neurons using AAV–mDlx5/6–ChR2 facilitates at least three broad categories of experiments. The first category includes experiments in which slow neural inactivation precludes data collection, for example, experiments probing the neural substrate of life-sustaining processes (e.g. breathing)(Simonyan, 2014; Baertsch, 2018). Less extreme examples include the inactivation of oculomotor

structures that are necessary for stable visual fixation, a simple oculomotor behavior without which those more complicated are difficult to study (Goffart, 2012; Krauzlis, 2017). Experiments in which inactivation induces compensatory changes in task strategy (Paolini, 1997) or the routing of neural signals also fall in this category (Mori, 2006; Cowey, 2010; Leopold, 2012; Kinoshita, 2019).

The second class of experiments are those that address questions about the functional significance of spike timing. Monkeys can learn to use signals present in sensory cortices at particular times relative to external and internal events to mediate their behavior (Roelfsema, 1998; Seidemann, 1998; Poort, 2012). Just as electrical microstimulation can be used to reveal the contribution of spikes added to sensory representations at specific times, optogenetic inactivation can be used, complementarily, to eliminate spikes. Indeed, optogenetic inactivation was recently used to show that spiking activity in the frontal eye fields of macaques contributes to memory guided saccades before, during, and after target presentation (Acker et al., 2016). Future studies may reveal differences between the transient vs. sustained phases of sensory-, decision- and movement-related signals for guiding behavior (Freedman, 2001; Roelfsema, 2007; Hegdé, 2008; Ibos, 2017; Shushruth, 2018).

A third class of experiments probes the electrophysiological response properties of inhibitory neurons in vivo (Cardin et al., 2009; Sohal et al., 2009; Adesnik, 2012; Atallah, 2012; Wilson, 2012; Scholl, 2015; Wilson et al., 2017). Excitatory and inhibitory neurons within a cortical area have different response properties in mice, cats and ferrets, a fact that is presumably related to differences in their respective functional contributions

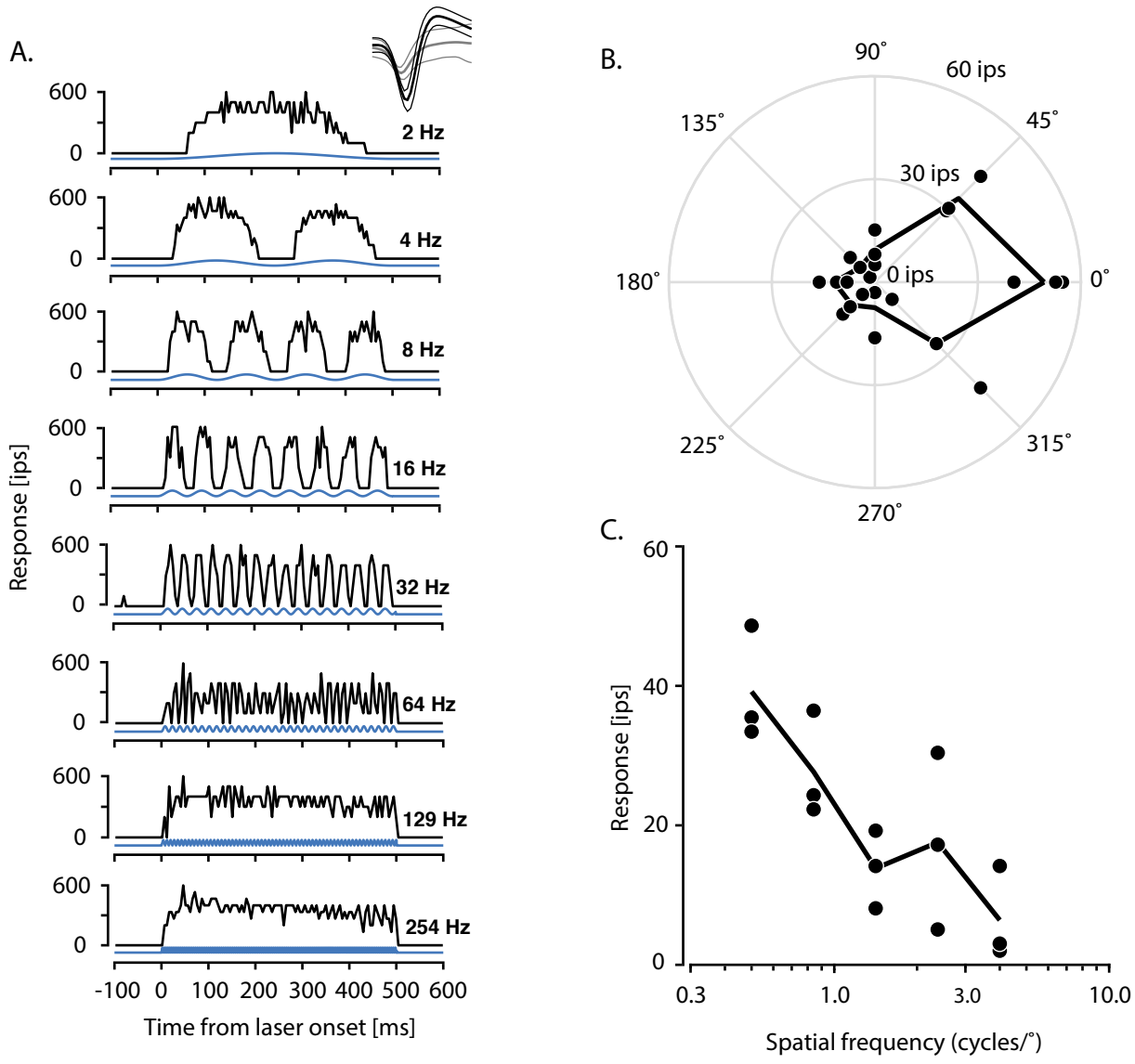

Figure 4.9. Responses of a putative GABAergic, direction-selective single-unit to optical (450 nm laser) and visual (drifting achromatic 3 Hz sinusoidal grating) stimulation **(A)**. Rasters (tick marks) and peristimulus time histograms (gray) in response to sinusoidal laser modulation from 2 Hz to 254 Hz (blue). Inset: Mean spike waveforms (thick black curve) and noise waveforms (thick gray curve) ± 1 standard deviation (thin curves). **(B)** Direction tuning curve showing individual (black points) and mean responses (black line) across repeated presentations of a drifting sinusoidal grating. **(C)** Spatial frequency tuning curve with symbols identical to **(B)**.

(Huang, 2018). Identification of inhibitory and excitatory neurons in vivo has been

challenging in monkeys. The discovery of fast spiking excitatory neurons in primates undermines the use of extracellularly recorded spike waveforms (Kelly, 2018). Optogenetic phototagging of inhibitory neurons, using AAV–mDlx5/6–ChR2 permits electrophysiological identification of neuronal subtypes more decisively (**Figure 4.9**).

In summary, the optogenetic approach used in this study holds promise for a finer level of neural circuit interrogation than previously achievable in monkeys. This union of neural inactivation technique and animal model has broad utility for addressing many outstanding questions in systems neuroscience that span the domains of sensation, action and cognition.

4.6 SUPPLEMENTARY FIGURES

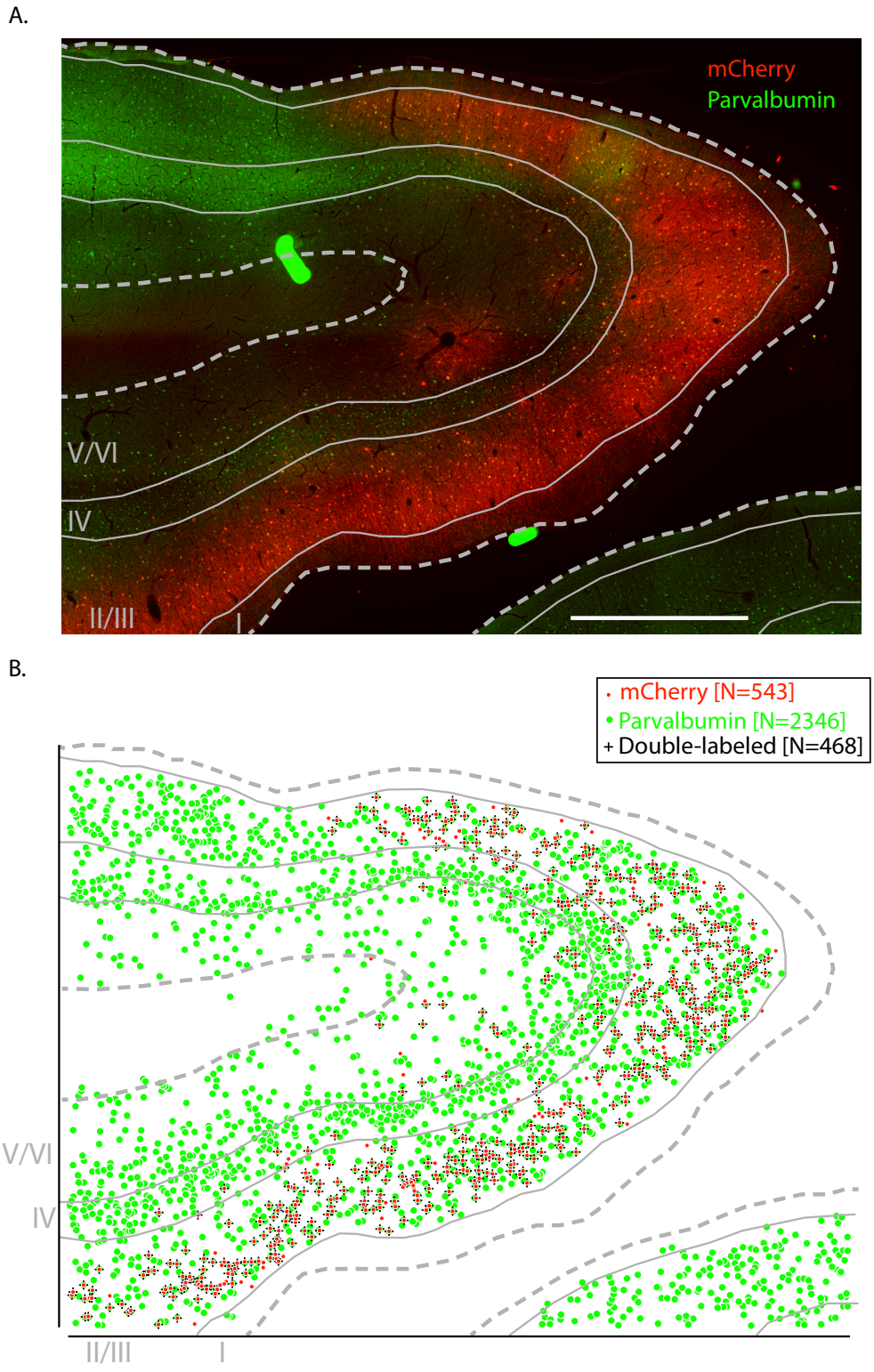

Figure S4.1. Immunohistochemical analysis of transduction by AAV1-mDlx5/6-ChR2-mCherry. **(A)** A histological section of V1/V2 from monkey 1 processed with antibodies against parvalbumin (green) and mCherry (red), imaged at 10X. Scale bar is 1 mm. **(B)** Locations of cell bodies in **(A)** expressing mCherry (red), parvalbumin (green) or both ("+").

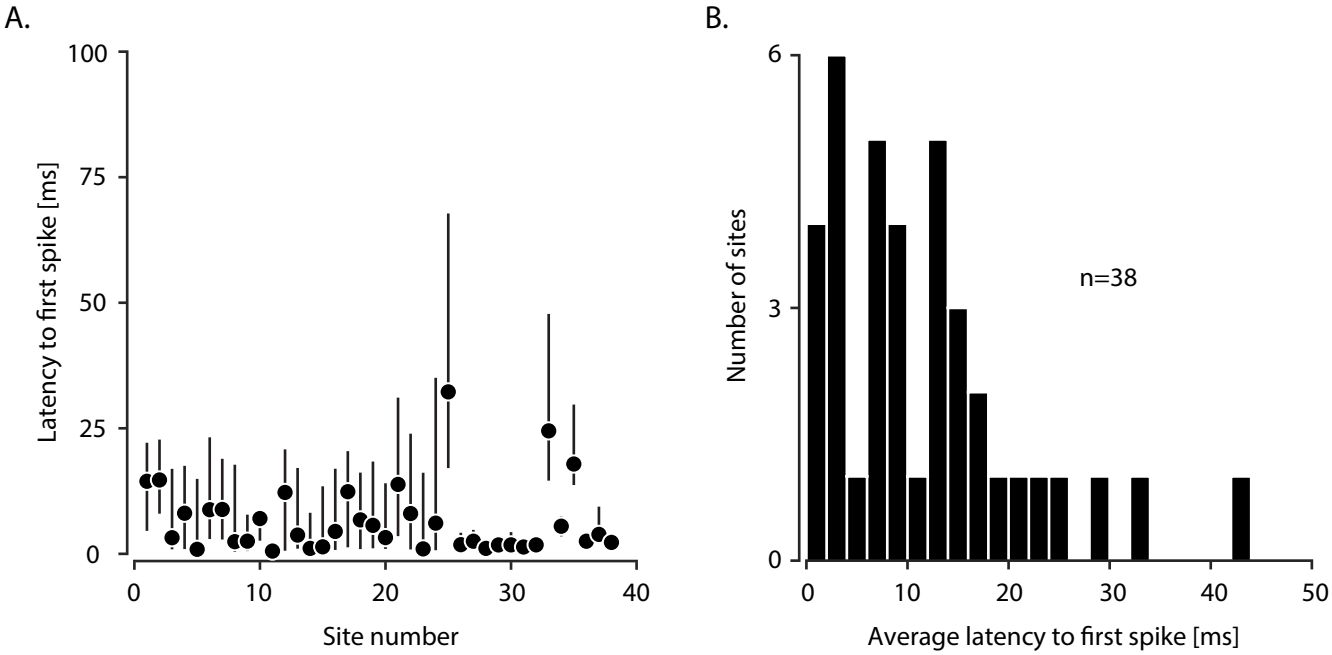

Figure S4.2. Analysis of latency to first spike at excited sites (n=38). **(A)** Latency was defined as the time to first spike following optical stimulation on each trial. Black points represent medians across trials within a site, and the lower and the upper end of vertical black lines represent the 25th and 75th percentiles. **(B)** Histogram of average latencies following optogenetic activation.

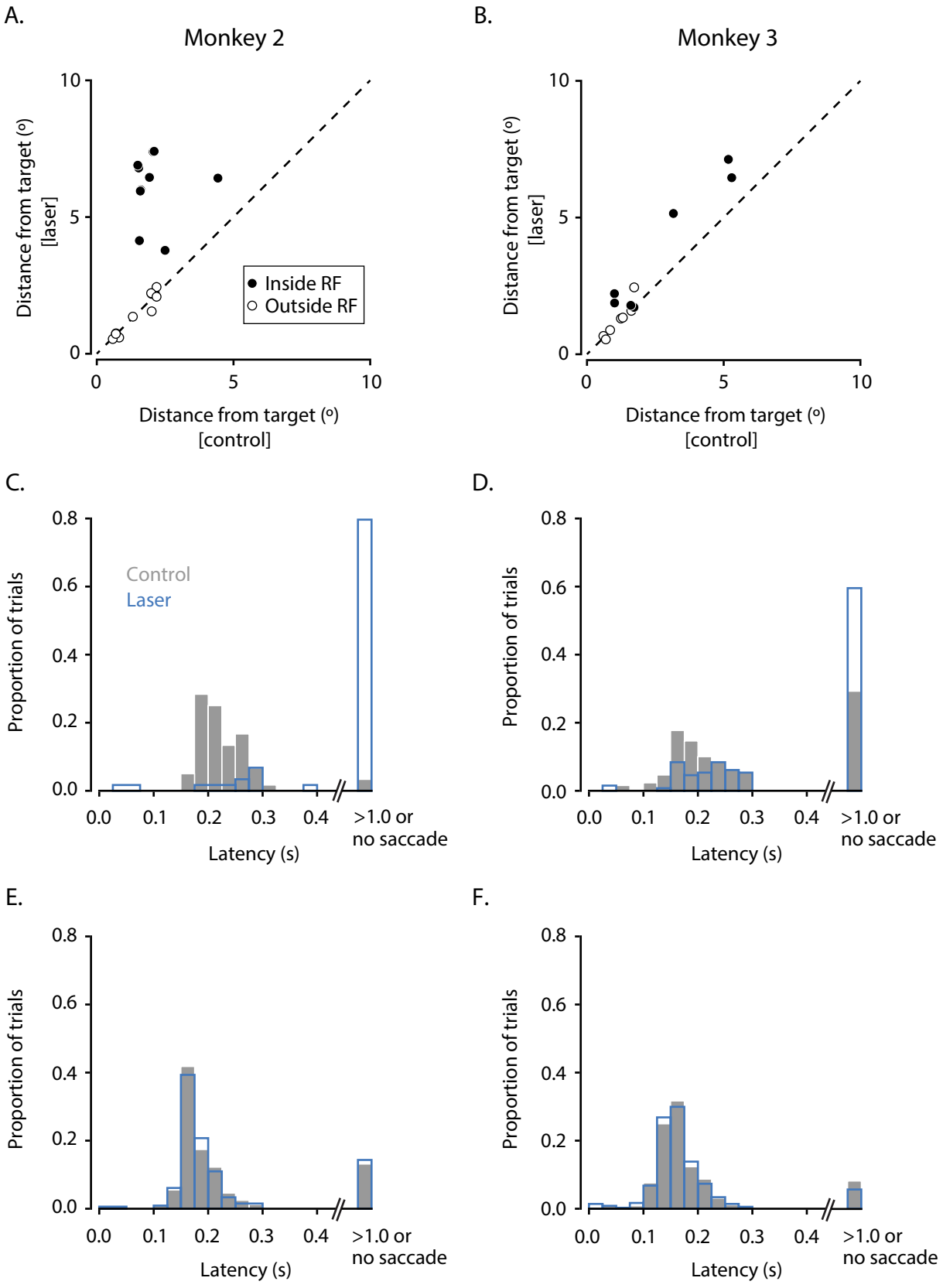

Figure S4.3. Effects of optogenetic inactivation of V1 on visually guided saccade accuracy and latency. **(A,B)** Saccade accuracy (the average distance between saccade end points and target location) on control and laser trials. Data from trials in which the target appeared inside the RFs of the stimulated neurons (filled symbols) were analyzed separately from interleaved trials in which the target appeared in other locations (open symbols). **(C)** Histograms of saccade latency on control (gray) and laser (blue) trials when the target was presented inside the RF. **(E)** Histograms of saccade latency on control (gray) and laser (blue) trials when the target was presented outside the RF. **(B,D,F)** Data from monkey 3 in the same format as **(A,C,E)**.

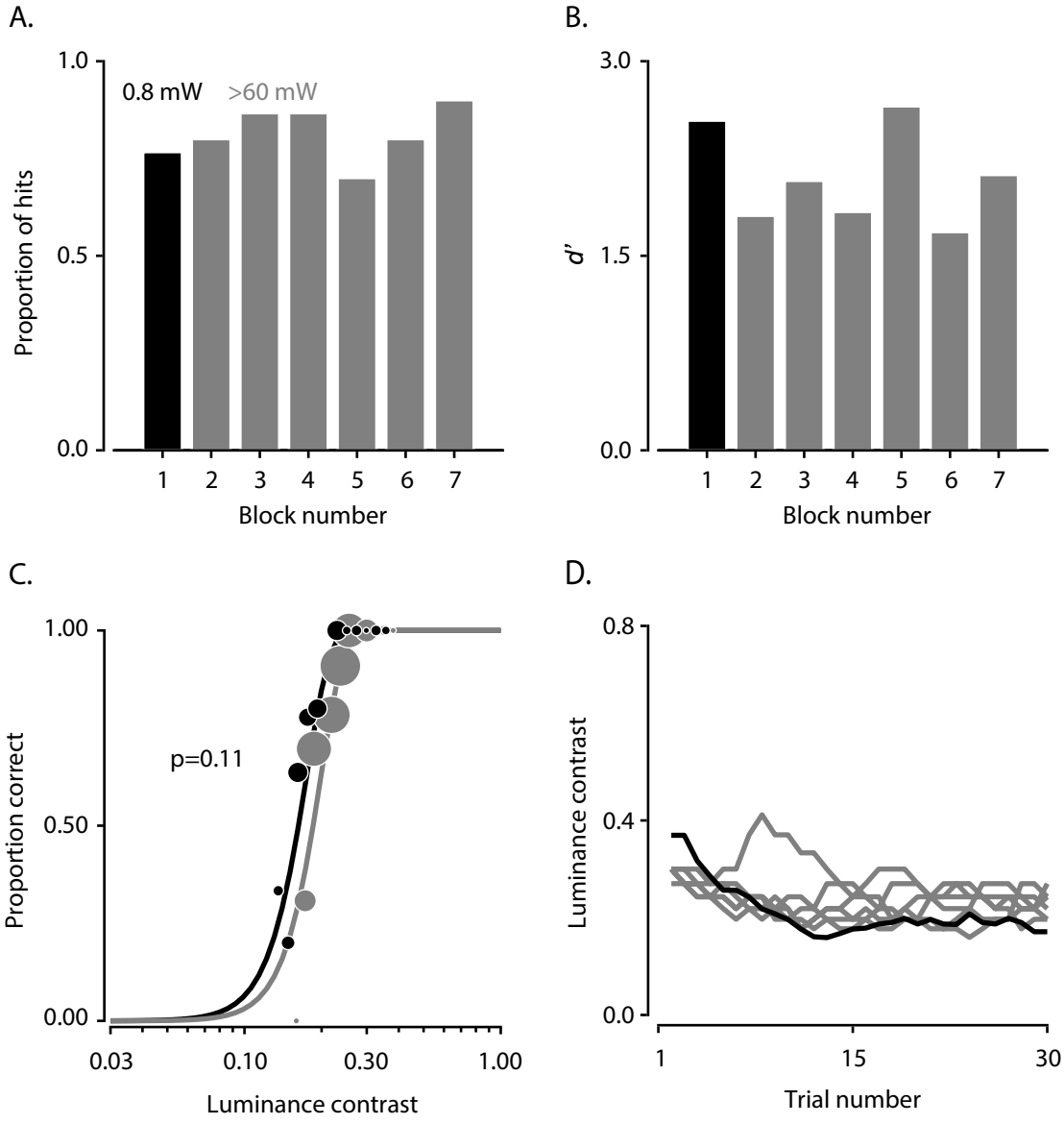

Figure S4.4. Contrast detection threshold was stable across seven blocks collected during a single session from monkey 3. In the first block, the laser power was low (0.8 mW) and performance was statistically indistinguishable on laser and control trials. For this block only, data from laser and control trials were pooled. In the subsequent blocks, the laser power was > 60 mW, and performance was significantly impaired on laser trials ($p<0.05$ in all cases, binomial test of proportions). For these blocks, data from control trials are only presented. **(A)** Proportion of hits in each block is plotted in chronological order. **(B)** *d'* in each block is plotted in chronological order. **(C)** Psychometric functions in the first and the pooled subsequent blocks did not differ significantly ($p=0.11$, Likelihood ratio test of separate Weibull fits to the first and the subsequent blocks data versus the best single fit to the pooled data). **(D)** Luminance contrast values selected by the staircase procedure as a function of trial number in each block.

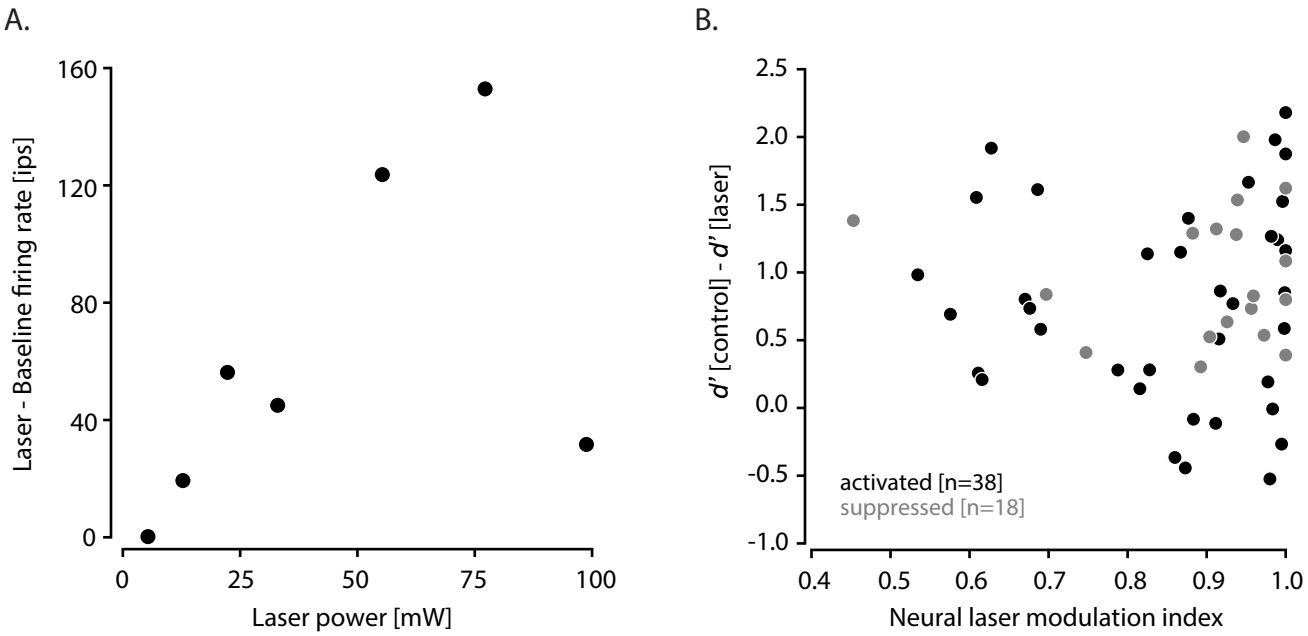

Figure S4.5. Correlation between optogenetic effects on neural activity and behavior. **(A)** Effect of laser power on firing rate across seven blocks from a single session. The difference in laser-evoked firing rate and baseline firing rate is plotted as a function of laser power. Behavioral effects for these blocks of trials are shown in **Figure 4.8B**. **(B)** Relationship between neurophysiological and behavioral effects at the activated (black) and suppressed (gray) sites during the Gabor contrast detection task. Neurophysiological effects were computed as the absolute value of the difference between laser-evoked and baseline firing rate, divided by the sum of two.

5. CONCLUSIONS AND FUTURE DIRECTIONS

In this thesis, I combined neurophysiological, behavioral, and computational techniques to study the function of macaque V1 neurons. Chapter 1 provided an introduction to the current understanding of V1 neurophysiology, and the link between V1 neural activity and behavior. Chapter 2 described the spatial RF structures of simple and DO cells. Chapter 3 described the mechanisms of spatial integration by individual simple and DO cells. Chapter 4 described the utility of cell-type specific manipulation to achieve fast, powerful and reversible neural inactivation. Next, I summarize the main findings and significance of this thesis, and discuss ideas about future experiments geared towards advancing visual neuroscience.

5.1 DO AND SIMPLE CELLS

In Chapter 2, I analyzed the spatial RF structure of DO and simple cells. Using white noise analysis and statistical model comparisons, I found that DO cell RFs are similar to simple cell RFs and can be modeled using Gabor functions—a result that is incompatible with a center-surround RF organization. In chapter 3, I analyzed the spatial integration of V1 cells. Using white noise analysis, closed loop technique and model comparisons, I found that DO cells, like simple cells, combine signals across their spatial RFs linearly. Together, a conclusion from the results of Chapters 2 and 3 is that DO cells are cone-opponent homologues of simple cells.

The functional similarity between DO and simple cells proposes a similar neural circuitry. The linearity of spatial integration is explained by an excitation-inhibition (or a push-pull) model which suggests that the RFs of simple cells and DO cells can be

constructed from the same set of LGN afferents with a minor change to the wiring. Moreover, just as simple cells are thought to converge onto complex cells to eliminate information about luminance polarity, DO cells may converge onto some complex cells to eliminate information about chromatic polarity. Such a role is consistent with the color and orientation tuning of one class of complex cells (Gouras, 1979; Johnson et al., 2001; Horwitz and Hass, 2012).

The functional similarity between DO and simple cells proposes a similar system of edge processing for color and luminance. Both cell types appear to carry independent information about spatial variations in natural scenes: DO cells carry information about orientation and phase of chromatic variations whereas simple cells carry information about orientation and phase of luminance variations. An advantage of having independent systems for analysis of edges is that the information could be shared and compared. For example, a comparison of overlap between a chromatic and a luminance edge can disambiguate material border from an illumination border, or a comparison of chromatic and luminance orientation flows could aid in shape-from-shading (Cavanagh, 1991; Kunsberg, 2018).

Taking a step back, the idea of a common framework for DO and simple cells is enticing but perhaps our conclusions are limited to the techniques and approaches we have used in our studies. We have treated each neuron as an isolated entity of the neural circuit and studied its visual computations. We have ignored many important factors such as individual contributions of lateral and feedback connections, neuronal correlations, layer-specific computations, inhibitory vs. excitatory cell types, molecular

profiles of cells and etc. Further studies will be important for understanding the contribution of such factors and linking them to the results of our studies.

Nevertheless, the simple framework of DO cells being cone-opponent simple cells puts forward new research directions that will require rigorous investigations. First direction would be to systematically investigate how cortical RFs of DO cells are built up and compare that to simple cells (Alonso, 2005; Jin, 2011). Experiments at that end will be important for verifying whether DO and simple cells are constructed from the same set of LGN afferents. Along those lines, testing the anatomical connectivity between DO and color-sensitive complex cells will be important. Second direction would be to investigate which layers do DO and simple cells reside, and do these cells segregate into separate groups based on morphological and molecular profiles. Third direction would be to investigate the link between DO cell neural activity and behavior. This would require training a monkey on behavioral task to report changes in chromatic contrast across an edge. Comparison of neural activity and behavioral report would shed light on how DO cell activity is read out.

5.2 CELLS THAT ARE NEITHER SIMPLE NOR DOUBLE-OPPONENT

In chapter 3, I analyzed the spatial integration of a subpopulation of V1 cells that are neither simple nor DO based on our classification criteria (**see section 3.3.10 Cell classification**). The spatial integration of these cell types was largely non-linear. We investigated whether the spatial non-linearity is due to a non-linear combination of signals between two linear subunits. On the contrary, the non-linearity was present within individual subunits suggesting that spatial non-linearity observed in isoresponse

measurements was in fact a reflection of non-linear signal integration within individual subunits. Further interrogation revealed that the magnitude of this non-linearity was positively correlated with the magnitude of S-cone input (not for DO and simple cells) suggesting that S-cone signal might be combined non-linearly with L- and M-cone signals in these cells. Our results are consistent with previous reports about the presence of strong S-cone signals in some non-linear V1 cells (Cottaris and De Valois, 1998; Horwitz et al., 2005; Conway and Livingstone, 2006).

It is unclear at this point what is the functional identify of the other (neither simple nor DO) cells. There is a possibility that these cells could be complex cells. It is also unclear what are the anatomical locations of these cells in V1. One hypothesis is that these cells lie in layer 2/3 where they combine inputs from parvocellular (layer 4Cβ) and koniocellular (layer 3B, 4A) recipients non-linearly. This hypothesis could perhaps be tested by identifying the inputs to other cells based on cross-correlation analysis and selectivity stimulating the parvocellular and koniocellular recipients to study their interactions.

5.3 POTENTIAL APPLICATIONS OF CLOSED-LOOP TECHNIQUE

A major technical innovation of Chapter 3 is the combination of white noise analysis and closed-loop technique for understanding signal integration. Such a combination of techniques facilities at least three investigations in area V1 for advancing color neurophysiology.

First, it facilities the investigation of interaction between classical RF center and non-classical RF surround. Non-classical surround of simple cells does not evoke neuronal response by itself but modulates the signal in the RF center non-linearly (Cavanaugh, 2002). An equivalent understanding for DO cells is absent. Previous studies that have investigated V1 color cells reached at opposing conclusions about how non-classical RF surround modulates signal in the RF center. One study suggests that a colored stimuli in the surround does not affect selectivity in the RF center whereas another study suggests that a colored stimuli in the surround changes selectivity in a manner that is consistent with the perceptual phenomena of simultaneous color contrast in humans (Wachtler, 2003; Solomon et al., 2004). The differences in the results maybe due to different stimuli, different color cell population, etc. Future experiments using closed-loop technique could shed light into the neural mechanisms of signal interaction between center and surround for V1 color cells. This class of experiments will especially be important for understanding the contextual influences in the neural activity that support color perception, and connecting the dots between neurophysiology and color psychophysics.

Second, it facilitates the investigation of color-luminance interactions in individual V1 cells. Some V1 cells respond to both color and luminance but their interaction is poorly understood (Gouras, 1979; Thorell et al., 1984; Johnson et al., 2001; Horwitz et al., 2005; Horwitz and Hass, 2012). One study reported that V1 cells that receive S-cone dominated input tend to increase their responses with either increment or decrement of luminance contrast (Horwitz et al., 2005). Such a non-linear interaction could enhance color processing. Future experiments could quantify the nature of color-luminance

interactions. Color-sensitive complex cells would serve as good candidates for such experiments.

Third, it facilitates the investigation of cone signal integration within individual parts of the RF. Previous studies have investigated cone-signal integration by stimulating the classical RF center, and the current study investigated the predicted cone-signal integration using white-noise analysis (Hanazawa et al., 2000; Horwitz and Hass, 2012). Measuring the cone-signal interaction within individual subunits will be important for dissecting neural circuits functionally and advancing models of color processing.

5.4 COLOR PROCESSING WITHIN LOCAL V1 CIRCUIT

Cortical computation depends on the interaction of signals between different cell types. The two major cortical cell types are glutamatergic pyramidal neurons (excitatory) and GABAergic interneurons (inhibitory). In primate cortex, a direct identification of these cortical cell types using molecular markers is still limited. Most studies have relied on the use of waveform shapes along with some other physiological parameters to identify cell types (Gur, 1999; Mitchell, 2007; Hussar, 2009; Woloszyn, 2012; Onorato, 2020). This indirect identification is strongly supported by intracellular investigations that have made possible to distinguish fast-spiking inhibitory interneurons from pyramidal neurons in extracellular recordings. Previous intracellular and extracellular investigations of putative excitatory and putative inhibitory V1 neurons have focused primarily on stimulus attributes other than color (Contreras, 2003; Cardin, 2005; Onorato, 2020).

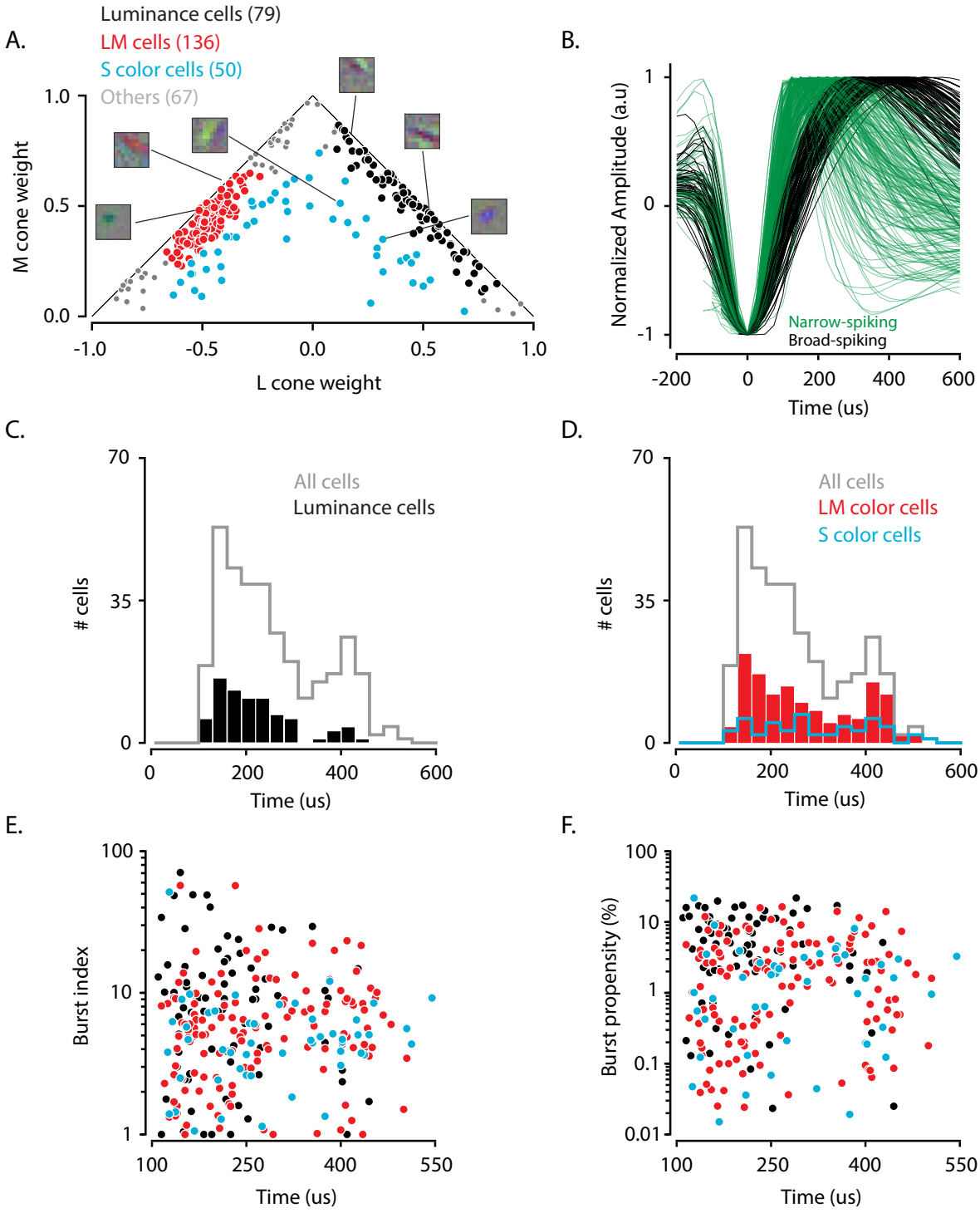

Figure 5.1 Waveform analyses of V1 single-units. **A.** Cells were classified as luminance (black), LM color (red), S color and unclassified (gray) based on cone weights. Shown are the spike-triggered averages of example luminance and color cells. **B.** Normalized waveform amplitudes of narrow (<290 μs, blue) and broad spiking (>290 μs, black) neurons. **C.** Histogram of waveform widths of luminance cells are plotted against all cells. Waveform width is defined as the time difference between the peak time and the trough time. **D.** Same as **C.** but for LM color and S color cells. **E.** Scatter plot of the burst index is plotted against the waveform duration. The burst index was determined by fitting two parametric models to the ISI distribution and, defined as the ratio of the height of the peak burst model fit relative to that of a single model fit. Luminance cells had higher burst index than color cells (p=0.003; Kruskal Wallis test) **F.** Scatter plot of burst propensity is plotted against the waveform duration. The burst propensity was defined as the percentage of bursts over all the spiking events. A "burst" was operationally defined to be a group (>=2) of action potentials each of which is <4 ms apart, with the first spike in a burst preceded by a period of >100 ms devoid of spiking activity. Luminance cells had higher burst propensity than color cells (p<0.0001; Kruskal Wallis test)

Parsing the chromatic representation by different classes of neurons is crucial for understanding their role in color vision. Therefore, we analyzed the waveforms of well-isolated single-units that were stimulated with whitenoise stimuli (data from Chapters 2 and 3). Based on spike-triggered averaging, we classified the cells as luminance (cone non-opponent), color (cone opponent), or neither (**Figure 5.1A**). We found evidence for differential chromatic tuning among the narrow-spiking (putative inhibitory or chattering cells) and broad-spiking (putative pyramidal) neurons (**Figure 5.1B**). We found that luminance-tuned neurons were mostly narrow spiking (**Figure 5.1C**), and color-tuned neurons (LM cone opponent and S-cone dominated) were both broad and narrow spiking (**Figure 5.1D**).

Consistent with previous studies in macaque V1, we found more narrow spiking neurons than broad spiking neurons (**Figure 5.1B–D**) (Gur, 1999; Onorato, 2020). A recent study found that narrow spiking neurons in V1 could be further segregated into high- and low-bursting neurons based on their firing statistics (Onorato, 2020). The high bursting neurons could be involved in generating γ (20–70Hz) oscillations and participating in long range communications (Onorato, 2020). Using two independent quantitative methods of calculating bursting, we studied the relationship between the propensity of bursting and waveform widths (Reinagel, 1999; Mitchell, 2007). We found that, among the narrow-spiking neurons, those tuned for luminance had higher propensity for bursting than color cells suggesting that luminance-tuned neurons could perhaps be analogous to the chattering cells found in cat V1 (Gray, 1996) (**Figure 5.1E–F**). These findings, at least to some extent, suggest that the inhibitory and excitatory neurons within V1 are specialized for representing color differently.

The prevalence of narrow spiking neurons than broad spiking neurons complicates the mapping between cell types and waveforms to certain extent. Given that only ~20% of cortical cells are inhibitory, only a fraction of narrow spiking neurons in V1 can be inhibitory. In fact, the existence of fast spiking excitatory neurons were reported recently (Kelly, 2018). Future investigations need to be more rigorous and direct for a clearer interpretation. One solution would be to use cell-type specific targeting using viral vectors and probing neuronal functions using photo-tagging (**see Figure 4.9**) (Cardin et al., 2009; Sohal et al., 2009; Adesnik, 2012; Atallah, 2012; Wilson, 2012; Scholl, 2015; Wilson et al., 2017).

5.5 IMPACT OF V1 NEURAL VARIABILITY AND BEHAVIOR

In Chapter 4, I describe a fast and powerful technique for reversibly inactivating macaque cortex. Using an adeno-associated viral (AAV) vector carrying the channelrhodopsin-2 gene under the control of a Dlx5/6 enhancer, we targeted and manipulated the spiking activity of GABAergic neurons in V1. Our optogenetic manipulation excited inhibitory neurons and therefore suppressed signal transmission from V1, which is exclusively excitatory (Girard and Bullier, 1989; Callaway, 1998). We predicted that the illumination of ChR2-expressing neurons would suppress the output of V1 and prevent the monkey from detecting the stimulus in well-controlled behavioral tasks. This prediction was confirmed; the monkey's sensitivity was lower on laser trials than on control trials. Additional experiments confirmed the spatial and temporal specificity of this behavioral manipulation. Given the fast and reversible nature of the

manipulation, this neural inactivation technique is well suited for studying the link between neural variability (noise) in V1 and behavior.

Information about stimuli becomes noisy over the cascade of visual processing (Horwitz, 2020). As a result, noise at every stage accumulates and affects behavioral performance. Therefore, understanding the contribution of noise is important. A visual contrast detection task serves as an ideal platform for studying the impact of neurophysiological noise (spontaneous neural activity) on behavior (Ress and Heeger, 2003; Palmer, 2007; Horwitz, 2020). Behavioral responses in this task are grouped into usual signal detection categories: hits, misses, false alarms and correct rejects.

The evidence about how neural fluctuations in V1 are linked to behavioral judgement is conflicted. fMRI studies in humans have shown that the activity in early visual cortex corresponds to subjects' percepts, i.e., trial-to-trial variability in the neural activity is strongly linked to trial-to-trial variability in perception (Rees, 2000; Ress and Heeger, 2003; Choe et al., 2014; Pajani et al., 2015). Neural responses in monkey V1 measured as spikes and sub-threshold voltage fluctuations display similar results (Palmer et al., 2007; Michelson, 2017). However, other electrophysiological investigations in monkey V1 have reported otherwise (Nienborg and Cumming, 2006; van Vugt et al., 2018). One possibility is that choice-related activity in V1 emerges later in time and could reflect post-decisional signal rather than pre-decisional signal (Nienborg and Cumming, 2009).

To investigate the role of noise in V1 on perceptual decisions, we analyzed stimulus-absent trials of the visual contrast detection task. On these trials, the monkey occasionally made erroneous behavioral reports (false alarms). We hypothesized that

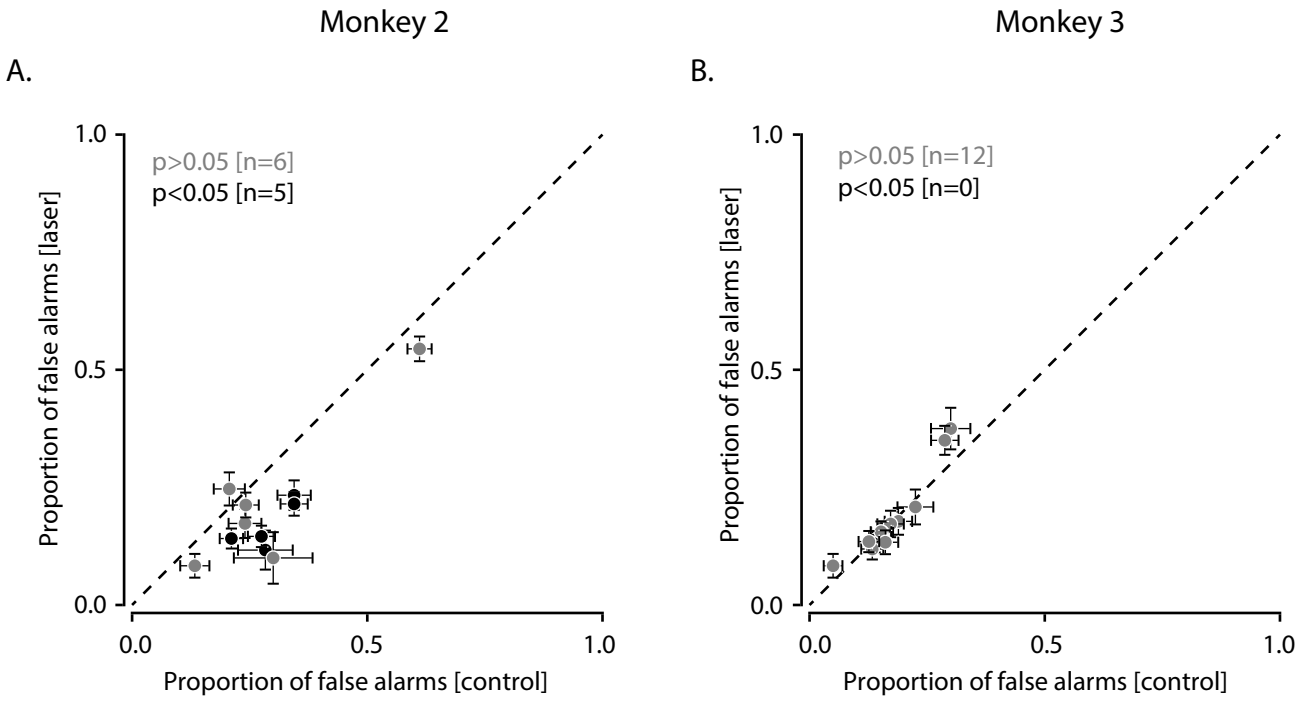

Figure 5.2. Effect of V1 inactivation on stimulus-absent trials across multiple sessions. **(A)** Scatter plot showing proportion of false alarms on control trials against laser trials from each session in monkey 2. Sessions with significantly fewer hits on laser trials than control trials are shown in black ($p < 0.05$, binomial test for equal proportions). Error bars represent the standard error of mean. **(B)** Data from monkey 3 in the same format as in **(A)**.

some false alarms are due to spontaneous fluctuations in the baseline activity of V1 neurons that resembled responses to a near-detection threshold low contrast stimulus. We therefore reasoned that optogenetic stimulation of V1 of stimulus-absent trials would improve performance by preventing these spontaneous spiking activity from triggering detection. Consistent with this idea, one monkey made fewer false alarms on laser trials than on control trials ($p=0.004$, Wilcoxon sign rank test) (**Figure 5.2A**). On the contrary, the other monkey made a similar number of false alarms on control and laser trials ($p=0.82$, Wilcoxon signed rank test) (**Figure 5.B**). Given the opposing results from the monkeys, we cannot decisively conclude how noise inherited from V1 impacts decision. The differences in the results from could perhaps be due to different ways of integrating

spatiotemporal information by the monkeys, ages of the monkeys, state of the arousal, etc. Experiment from another monkey will be important for a conclusive answer.

Bibliography

1. Abraham WC (2008) Metaplasticity: Tuning synapses and networks for plasticity. Nature Reviews Neuroscience 9.
2. Acker L, Pino EN, Boyden ES, Desimone R (2016) FEF inactivation with improved optogenetic methods. Proc Natl Acad Sci U S A 113:E7297-E7306.
3. Adesnik H, Bruns, W., Taniguchi, H., Huang, Z. J., & Scanziani, M. (2012) A neural circuit for spatial summation in visual cortex. Nature 490.
4. Afraz A, Boyden ES, DiCarlo JJ (2015) Optogenetic and pharmacological suppression of spatial clusters of face neurons reveal their causal role in face gender discrimination. Proc Natl Acad Sci U S A 112:6730-6735.
5. Afraz SR, Kiani R, Esteky H (2006) Microstimulation of inferotemporal cortex influences face categorization. Nature 442:692-695.
6. Agmon A, & Connors, B. W. (1992) Correlation between intrinsic firing patterns and thalamocortical synaptic responses of neurons in mouse barrel cortex. Journal of Neuroscience 12:319-329.
7. Alonso JM, & Martinez, L. M. (1998) Functional connectivity between simple cells and complex cells in cat striate cortex. Nature neuroscience 1.
8. Alonso JM, & Swadlow, H. A. (2005) Thalamocortical specificity and the synthesis of sensory cortical receptive fields. Journal of neurophysiology 94:26-32.
9. Arias-Gil G, Ohl, F. W., Takagaki, K., & Lippert, M. T. (2016) Measurement, modeling, and prediction of temperature rise due to optogenetic brain stimulation. Neurophotonics 3.
10. Atallah BV, Bruns, W., Carandini, M., & Scanziani, M. (2012) Parvalbumin-expressing interneurons linearly transform cortical responses to visual stimuli. Neuron 73:159-170.
11. Baertsch NA, Baertsch, H. C., & Ramirez, J. M. (2018) The interdependence of excitation and inhibition for the control of dynamic breathing rhythms. Nature communications 9.
12. Benda J, Gollisch T, Machens CK, Herz AV (2007) From response to stimulus: adaptive sampling in sensory physiology. Curr Opin Neurobiol 17:430-436.

13. Berndt A, Yizhar O, Gunaydin LA, Hegemann P, Deisseroth K (2009) Bi-stable neural state switches. Nat Neurosci 12:229-234.
14. Boyden ES, Zhang F, Bamberg E, Nagel G, Deisseroth K (2005) Millisecond-timescale, genetically targeted optical control of neural activity. Nat Neurosci 8:1263-1268.
15. Bradley A, Switkes, E., & De Valois, K. (1988) Orientation and spatial frequency selectivity of adaptation to color and luminance gratings. Vision research 28:841-856.
16. Brainard DH (1997) The Psychophysics Toolbox. Spat Vis 10:433-436.
17. Britten KH, Shadlen, M. N., Newsome, W. T., & Movshon, J. A. (1992) The analysis of visual motion: a comparison of neuronal and psychophysical performance. Journal of Neuroscience 12:4745-4765.
18. Callaway EM (1998) Local circuits in primary visual cortex of the macaque monkey. Annual review of neuroscience 21:47-74.
19. Callaway EM (2004) Feedforward, feedback and inhibitory connections in primate visual cortex. Neural Networks 17:625-632.
20. Callaway EM, & Wiser, A. K. (1996) Contributions of individual layer 2–5 spiny neurons to local circuits in macaque primary visual cortex. Visual neuroscience 13:907-922.
21. Carandini M (2006) What simple and complex cells compute. The Journal of physiology 577.
22. Carandini M, Heeger DJ, Movshon JA (1997) Linearity and normalization in simple cells of the macaque primary visual cortex. J Neurosci 17:8621-8644.
23. Cardin JA, Carlen M, Meletis K, Knoblich U, Zhang F, Deisseroth K, Tsai LH, Moore CI (2009) Driving fast-spiking cells induces gamma rhythm and controls sensory responses. Nature 459:663-667.
24. Cardin JA, Palmer, L. A., & Contreras, D. (2005) Stimulus-dependent γ (30-50 Hz) oscillations in simple and complex fast rhythmic bursting cells in primary visual cortex. Journal of neuroscience 25:5339-5350.
25. Casagrande VA (1994) A third parallel visual pathway to primate area V1. Trends in neurosciences 17:305-309.

26. Casagrande VA, & Xu, X. (2004) Parallel visual pathways: a comparative perspective. In: The Visual Neurosciences (Chalupa LM, Werner JS, eds):494-506.
27. Cavanagh P (1991) Vision at equiluminance. Vision and visual dysfunction: Limits of vision 5:234-250.
28. Cavanaugh J, Monosov IE, McAlonan K, Berman R, Smith MK, Cao V, Wang KH, Boyden ES, Wurtz RH (2012) Optogenetic inactivation modifies monkey visuomotor behavior. Neuron 76:901-907.
29. Cavanaugh JR, Bair, W., & Movshon, J. A. (2002) Nature and interaction of signals from the receptive field center and surround in macaque V1 neurons. Journal of neurophysiology 88:2530-2546.
30. Chatterjee S, Callaway EM (2003) Parallel colour-opponent pathways to primary visual cortex. Nature 426:668-671.
31. Chichilnisky EJ (2001) A simple white noise analysis of neuronal light responses. Network 12:199-213.
32. Choe KW, Blake R, Lee SH (2014) Dissociation between neural signatures of stimulus and choice in population activity of human V1 during perceptual decision-making. J Neurosci 34:2725-2743.
33. Cohen MR, Newsome WT (2008) Context-dependent changes in functional circuitry in visual area MT. Neuron 60:162-173.
34. Cone JJ, Scantlen, M. D., Histed, M. H., & Maunsell, J. H. (2019) Different inhibitory interneuron cell classes make distinct contributions to visual contrast perception. eNeuro 6.
35. Contreras D, & Palmer, L. (2003) Response to contrast of electrophysiologically defined cell classes in primary visual cortex. Journal of Neuroscience 23:6936-6945.
36. Conway BR (2001) Spatial structure of cone inputs to color cells in alert macaque primary visual cortex (V-1). Journal of Neuroscience 21:2768-2783.
37. Conway BR, Livingstone MS (2006) Spatial and temporal properties of cone signals in alert macaque primary visual cortex. J Neurosci 26:10826-10846.
38. Conway BR, Chatterjee S, Field GD, Horwitz GD, Johnson EN, Koida K, Mancuso K (2010) Advances in Color Science: From Retina to Behavior. Journal of Neuroscience 30:14955-14963.

39. Cook EP, & Maunsell, J. H. (2002) Dynamics of neuronal responses in macaque MT and VIP during motion detection. Nature neuroscience 5:985-994.
40. Cottaris NP, De Valois RL (1998) Temporal dynamics of chromatic tuning in macaque primary visual cortex. Nature 395:896-900.
41. Cowey A (2010) The blindsight saga. Exp Brain Res 200:3-24.
42. Dacey DM (2000) Parallel pathways for spectral coding in primate retina. Annu Rev Neurosci 23:743-775.
43. Dacey DM, Lee BB (1994) The 'blue-on' opponent pathway in primate retina originates from a distinct bistratified ganglion cell type. Nature 367:731-735.
44. Dai J, Brooks DI, Sheinberg DL (2014) Optogenetic and electrical microstimulation systematically bias visuospatial choice in primates. Curr Biol 24:63-69.
45. Dantzker JL, & Callaway, E. M. (2000) Laminar sources of synaptic input to cortical inhibitory interneurons and pyramidal neurons. Nature neuroscience 3:701-707.
46. Daw NW (1968) Colour-coded ganglion cells in the goldfish retina: extension of their receptive fields by means of new stimuli. The Journal of physiology 197:567-592.
47. Dawis S, Shapley, R., Kaplan, E., & Tranchina, D. (1984) The receptive field organization of X-cells in the cat: spatiotemporal coupling and asymmetry. Vision research 24:549-564.
48. De A, & Horwitz, G. D. (2020) Spatial receptive field structure of double-opponent and simple cells in macaque primary visual cortex. bioRxiv.
49. De Valois RL, Cottaris NP, Elfar SD, Mahon LE, Wilson JA (2000) Some transformations of color information from lateral geniculate nucleus to striate cortex. Proc Natl Acad Sci U S A 97:4997-5002.
50. DeAngelis GC, Cumming BG, Newsome WT (1998) Cortical area MT and the perception oThe threshold for conscious report: Signal loss and responses bias in visual and frontal cortexf stereoscopic depth. Nature 394:677-680.
51. DeAngelis GC, & Anzai, A. (2004) A modern view of the classical receptive field: Linear and non-linear spatio-temporal processing by V1 neurons. The visual neurosciences 1:704-719.

52. DeAngelis GC, Ohzawa, I., & Freeman, R. D. (1993) Spatiotemporal organization of simple-cell receptive fields in the cat's striate cortex. II. Linearity of temporal and spatial summation. Journal of Neurophysiology 69:1118-1135.
53. Derrington AM, Lennie P (1984) Spatial and temporal contrast sensitivities of neurones in lateral geniculate nucleus of macaque. J Physiol 357:219-240.
54. Derrington AM, Krauskopf J, Lennie P (1984) Chromatic mechanisms in lateral geniculate nucleus of macaque. J Physiol 357:241-265.
55. DeValois RL, & DeValois, K. K. (1990) Spatial vision. Oxford university press 14.
56. Dimidschstein J et al. (2016) A viral strategy for targeting and manipulating interneurons across vertebrate species. Nat Neurosci 19:1743-1749.
57. Dow BM, Gouras P (1973) Color and spatial specificity of single units in Rhesus monkey foveal striate cortex. Journal of Neurophysiology 36:79-100.
58. Economides JR, Sincich, L. C., Adams, D. L., & Horton, J. C. (2011) Orientation tuning of cytochrome oxidase patches in macaque primary visual cortex. Nature neuroscience 14.
59. El-Shamayleh Y, Movshon JA (2011) Neuronal responses to texture-defined form in macaque visual area V2. J Neurosci 31:8543-8555.
60. El-Shamayleh Y, Kojima Y, Soetedjo R, Horwitz GD (2017) Selective optogenetic control of Purkinje cells in monkey cerebellum. Neuron 95:51-62 e54.
61. Ferster D (1988) Spatially opponent excitation and inhibition in simple cells of the cat visual cortex. Journal of Neuroscience 8:1172-1180.
62. Ferster D, & Miller, K. D. (2000) Neural mechanisms of orientation selectivity in the visual cortex. Annual review of neuroscience 23:441-471.
63. Fetsch CR, Odean NN, Jeurissen D, El-Shamayleh Y, Horwitz GD, Shadlen MN (2018) Focal optogenetic suppression in macaque area MT biases direction discrimination and decision confidence, but only transiently. Elife 7.
64. Field GD, Gauthier JL, Sher A, Greschner M, Machado TA, Jepson LH, Shlens J, Gunning DE, Mathieson K, Dabrowski W, Paninski L, Litke AM, Chichilnisky EJ (2010) Functional connectivity in the retina at the resolution of photoreceptors. Nature 467:673-677.

65. Fine I, MacLeod, D. I., & Boynton, G. M. (2003) Surface segmentation based on the luminance and color statistics of natural scenes. JOSA A 20:1283-1291.
66. Fox J, & Weisberg, S. (2002) Robust regression. An R and S-Plus companion to applied regression 91.
67. Freedman DJ, Riesenhuber, M., Poggio, T., & Miller, E. K. (2001) Categorical representation of visual stimuli in the primate prefrontal cortex. Science 291:312-316.
68. Freund TF, Martin, K. A. C., Soltesz, I., Somogyi, P., & Whitteridge, D. (1989) Arborisation pattern and postsynaptic targets of physiologically identified thalamocortical afferents in striate cortex of the macaque monkey. Journal of Comparative Neurology 289:315-336.
69. Friedman HS, Zhou, H., & von der Heydt, R. (2003) The coding of uniform colour figures in monkey visual cortex. The Journal of physiology 548:593-613.
70. Gao S, Yang K, Li C, Li Y (2013) A color constancy model with double-opponency mechanisms. In: ICCV, pp 929-936.
71. Garg AK, Li, P., Rashid, M. S., & Callaway, E. M. (2019) Color and orientation are jointly coded and spatially organized in primate primary visual cortex. Science 364:1275-1279.
72. Gegenfurtner KR (2003) Cortical mechanisms of colour vision. Nat Rev Neurosci 4:563-572.
73. Gerits A, Farivar R, Rosen BR, Wald LL, Boyden ES, Vanduffel W (2012) Optogenetically induced behavioral and functional network changes in primates. Curr Biol 22:1722-1726.
74. Gibson JR, Beierlein, M., & Connors, B. W. (1999) Two networks of electrically coupled inhibitory neurons in neocortex. Nature 402:75-79.
75. Girard P, Bullier J (1989) Visual activity in area V2 during reversible inactivation of area 17 in the macaque monkey. J Neurophysiol 62:1287-1302.
76. Girard P, & Morrone, M. C. (1995) Spatial structure of chromatically opponent receptive fields in the human visual system. Visual neuroscience 12:103-116.
77. Glickfeld LL, Histed MH, Maunsell JH (2013) Mouse primary visual cortex is used to detect both orientation and contrast changes. J Neurosci 33:19416-19422.

78. Goffart L, Hafed, Z. M., & Krauzlis, R. J. (2012) Visual fixation as equilibrium: evidence from superior colliculus inactivation. Journal of Neuroscience 32:10627-10636.
79. Gold JI, & Shadlen, M. N. (2000) Representation of a perceptual decision in developing oculomotor commands. Nature 404:390-394.
80. Gollisch T, Herz AV (2012) The iso-response method: measuring neuronal stimulus integration with closed-loop experiments. Front Neural Circuits 6:104.
81. Gollisch T, Schütze, H., Benda, J., & Herz, A. V. (2002) Energy integration describes sound-intensity coding in an insect auditory system. Journal of Neuroscience 22:10434-10448.
82. Goold CP, & Nicoll, R. A. (2010) Single-cell optogenetic excitation drives homeostatic synaptic depression. Neuron 68:512-528.
83. Goshen I, Brodsky, M., Prakash, R., Wallace, J., Gradinaru, V., Ramakrishnan, C., & Deisseroth, K. (2011) Dynamics of retrieval strategies for remote memories. Cell 147:678-689.
84. Gouras PETER, & Kruger, J. (1979) Responses of cells in foveal visual cortex of the monkey to pure color contrast. Journal of Neurophysiology 42:850-860.
85. Gray CM, & McCormick, D. A. (1996) Chattering cells: superficial pyramidal neurons contributing to the generation of synchronous oscillations in the visual cortex. Science 274:109-113.
86. Green DM, Swets JA (1966) Signal detection theory and psychophysics. New York: Wiley.
87. Gregory RL (1977) Vision with isoluminant colour contrast: 1. A projection technique and observations. Perception 6:113-119.
88. Gross CG (1999) Brain, vision, memory: Tales in the history of neuroscience. MIT Press.
89. Guillery RW, & Sherman, S. M. (2002) Thalamic relay functions and their role in corticocortical communication: generalizations from the visual system. Neuron 33:163-175.

90. Guo ZV, Li, N., Huber, D., Ophir, E., Gutnisky, D., Ting, J.T., Feng, G. and Svoboda, K. (2014) Flow of cortical activity underlying a tactile decision in mice. Neuron 81:179-194.
91. Gur M, Beylin, A., & Snodderly, D. M. (1999) Physiological properties of macaque V1 neurons are correlated with extracellular spike amplitude, duration, and polarity. Journal of neurophysiology 82:1451-1464.
92. Hallum LE, & Movshon, J. A. (2014) Surround suppression supports second-order feature encoding by macaque V1 and V2 neurons. Vision research 104:24-35.
93. Hanazawa A, Komatsu H, Murakami I (2000) Neural selectivity for hue and saturation of colour in the primary visual cortex of the monkey. Eur J Neurosci 12:1753-1763.
94. Hanks TD, Kopec, C. D., Brunton, B. W., Duan, C. A., Erlich, J. C., & Brody, C. D. (2015) Distinct relationships of parietal and prefrontal cortices to evidence accumulation. Nature 520.
95. Hass CA, Horwitz GD (2013) V1 mechanisms underlying chromatic contrast detection. Journal of Neurophysiology 109:2483-2494.
96. Hasse JM, & Briggs, F. (2017) Corticogeniculate feedback sharpens the temporal precision and spatial resolution of visual signals in the ferret. Proceedings of the National Academy of Sciences 114:E6222-E6230.
97. Hegdé J (2008) Time course of visual perception: coarse-to-fine processing and beyond. Progress in neurobiology 84:405-439.
98. Hendry SH, & Yoshioka, T. (1994) A neurochemically distinct third channel in the macaque dorsal lateral geniculate nucleus. Science 264:575-577.
99. Henry CA, Jazayeri, M., Shapley, R. M., & Hawken, M. J. (2020) Distinct spatiotemporal mechanisms underlie extra-classical receptive field modulation in macaque V1 microcircuits. Elife 9.
100. Hirsch JA, Alonso, J. M., Reid, R. C., & Martinez, L. M. (1998) Synaptic integration in striate cortical simple cells. Journal of neuroscience 18:9517-9528.
101. Hirsch JA, Martinez, L. M., Pillai, C., Alonso, J. M., Wang, Q., & Sommer, F. T. (2003) Functionally distinct inhibitory neurons at the first stage of visual cortical processing. Nature neuroscience 6.

102.Horwitz GD (2020) Temporal information loss in the macaque early visual system. PLoS Biology 18:e3000570.

103.Horwitz GD, Albright TD (2005) Paucity of chromatic linear motion detectors in macaque V1. J Vis 5:525-533.

104.Horwitz GD, Hass CA (2012) Nonlinear analysis of macaque V1 color tuning reveals cardinal directions for cortical color processing. Nat Neurosci 15:913-919.

105.Horwitz GD, Chichilnisky EJ, Albright TD (2005) Blue-yellow signals are enhanced by spatiotemporal luminance contrast in macaque V1. Journal of Neurophysiology 93:2263-2278.

106.Horwitz GD, Chichilnisky EJ, Albright TD (2007) Cone inputs to simple and complex cells in V1 of awake macaque. Journal of Neurophysiology 97:3070-3081.

107.Huang ZJ, & Paul, A. (2018) Diversity of GABAergic interneurons and diversification of communication modules in cortical networks. bioRxiv 490797.

108.Hubel DH, Wiesel TN (1962) Receptive fields, binocular interaction and functional architecture in the cat's visual cortex. J Physiol 160:106-154.

109.Hubel DH, Wiesel TN (1968) Receptive fields and functional architecture of monkey striate cortex. J Physiol 195:215-243.

110.Hubel DH, & Wiesel, T. N. (1959) Receptive fields of single neurones in the cat's striate cortex. The Journal of physiology 148:574-591.

111.Hubel DH, & Wiesel, T. N. (1969) Anatomical demonstration of columns in the monkey striate cortex. Nature 221:747-750.

112.Hubel DH, & Wiesel, T. N. (1972) Laminar and columnar distribution of geniculo-cortical fibers in the macaque monkey. Journal of Comparative Neurology 146:421-450.

113.Hubel DH, and Torsten N. Wiesel. (1962) Receptive fields, binocular interaction and functional architecture in the cat's visual cortex. The Journal of physiology 160:106-154.

114.Hussar CR, & Pasternak, T. (2009) Flexibility of sensory representations in prefrontal cortex depends on cell type. Neuron 64:730-743.

115.Ibos G, & Freedman, D. J. (2017) Sequential sensory and decision processing in posterior parietal cortex. Elife 6.

116.Inoue K, Takada M, Matsumoto M (2015) Neuronal and behavioural modulations by pathway-selective optogenetic stimulation of the primate oculomotor system. Nat Commun 6:8378.

117.Isaacson JS, & Scanziani, M. (2011) How inhibition shapes cortical activity. Neuron 72:231-243.

118.Jazayeri M, Lindbloom-Brown Z, Horwitz GD (2012) Saccadic eye movements evoked by optogenetic activation of primate V1. Nat Neurosci 15:1368-1370.

119.Jin J, Wang, Y., Swadlow, H. A., & Alonso, J. M. (2011) Population receptive fields of ON and OFF thalamic inputs to an orientation column in visual cortex. Nature neuroscience 14.

120.Johnson EN, Hawken MJ, Shapley R (2001) The spatial transformation of color in the primary visual cortex of the macaque monkey. Nat Neurosci 4:409-416.

121.Johnson EN, Hawken MJ, Shapley R (2004) Cone inputs in macaque primary visual cortex. Journal of Neurophysiology 91:2501-2514.

122.Johnson EN, Hawken MJ, Shapley R (2008) The orientation selectivity of color-responsive neurons in macaque V1. J Neurosci 28:8096-8106.

123.Johnson EN, & Mullen, K. T. (2016) Color in the Cortex. In Human color vision. Springer, Cham:pp. 189-217.

124.Jones JP, & Palmer, L. A. (1987) An evaluation of the two-dimensional Gabor filter model of simple receptive fields in cat striate cortex. Journal of neurophysiology 58:1233-1258.

125.Katz LN, Yates, J. L., Pillow, J. W., & Huk, A. C. (2016) Dissociated functional significance of decision-related activity in the primate dorsal stream. Nature 535.

126.Kelly JG, García-Marín, V., Rudy, B., & Hawken, M. J. (2018) Densities and Laminar Distributions of Kv3. 1b-, PV-, GABA-, and SMI-32-Immunoreactive Neurons in Macaque Area V1. Cerebral cortex (New York, NY: 1991).

127.Khan AG, Poort, J., Chadwick, A., Blot, A., Sahani, M., Mrsic-Flogel, T. D., & Hofer, S. B. (2018) Distinct learning-induced changes in stimulus selectivity and interactions of GABAergic interneuron classes in visual cortex. Nature neuroscience 21.

128.Kingdom FA (2003) Color brings relief to human vision. Nature neuroscience 6.

129.Kinoshita M, Kato, R., Isa, K., Kobayashi, K., Kobayashi, K., Onoe, H., & Isa, T. (2019) Dissecting the circuit for blindsight to reveal the critical role of pulvinar and superior colliculus. Nature communications 10.

130.Klein C, Evrard, H. C., Shapcott, K. A., Haverkamp, S., Logothetis, N. K., & Schmid, M. C. (2016) Cell-targeted optogenetics and electrical microstimulation reveal the primate koniocellular projection to supra-granular visual cortex. Neuron 90:143-151.

131.Koenderink JJ, van Doorn, A. J., Chalupa, L. M., & Werner, J. S. (2003) Shape and shading. The visual neurosciences 2:1090-1105.

132.Koerner F, & Teuber, H. L. (1973) Visual field defects after missile injuries to the geniculo-striate pathway in man. Experimental Brain Research 18:88-113.

133.Krauzlis RJ, Goffart, L., & Hafed, Z. M. (2017) Neuronal control of fixation and fixational eye movements. Philosophical Transactions of the Royal Society B: Biological Sciences 372.

134.Kubota Y, Kondo, S., Nomura, M., Hatada, S., Yamaguchi, N., Mohamed, A. A., ... & Kawaguchi, Y. (2015) Functional effects of distinct innervation styles of pyramidal cells by fast spiking cortical interneurons. eLife 4.

135.Kuffler SW (1953) Discharge patterns and functional organization of mammalian retina. Journal of neurophysiology 16:37-68.

136.Kunsberg B, Holtmann-Rice, D., Alexander, E., Cholewiak, S., Fleming, R., & Zucker, S. W. (2018) Colour, contours, shading and shape: flow interactions reveal anchor neighbourhoods. Interface focus 8.

137.Landy MS, & Graham, N. (2004) 73 Visual Perception of Texture. The visual neurosciences.

138.Law CT, & Gold, J. I. (2008) Neural correlates of perceptual learning in a sensory-motor, but not a sensory, cortical area. Nature neuroscience 11:505-513.

139.Lennie P, Krauskopf J, Sclar G (1990) Chromatic mechanisms in striate cortex of macaque. J Neurosci 10:649-669.

140.Leopold DA (2012) Primary visual cortex: awareness and blindsight. Annual review of neuroscience 35:91-109.

141.Leventhal AG, Thompson, K. G., Liu, D., Zhou, Y. I. F. E. N. G., & Ault, S. J. (1995) Concomitant sensitivity to orientation, direction, and color of cells in layers 2, 3, and 4 of monkey striate cortex. Journal of Neuroscience 15:1808-1818.

142.Livingstone MS, Hubel DH (1984) Anatomy and physiology of a color system in the primate visual cortex. J Neurosci 4:309-356.

143.Livingstone MS, & Hubel, D. H. (1987) Psychophysical evidence for separate channels for the perception of form, color, movement, and depth. Journal of Neuroscience 7:3416-3468.

144.Long MA, & Fee, M. S. (2008) Using temperature to analyse temporal dynamics in the songbird motor pathway. Nature 456:189-194.

145.Macmillan NA, & Creelman, C. D. (2004) Detection theory: A user's guide. Psychology press.

146.Marr D, & Poggio, T. (1976) From understanding computation to understanding neural circuitry.

147.Masland RH (2001) The fundamental plan of the retina. Nature neuroscience 4:877-886.

148.McBride EG, Lee, S. Y. J., & Callaway, E. M. (2019) Local and global influences of visual spatial selection and locomotion in mouse primary visual cortex. Current Biology 29:1592-1605.

149.McIlhagga W, & Mullen, K. T. (2018) Evidence for chromatic edge detectors in human vision using classification images. Journal of vision 18.

150.Merigan WH, Nealey, T. A., & Maunsell, J. H. (1993) Visual effects of lesions of cortical area V2 in macaques. Journal of Neuroscience 13:3180-3191.

151.Michael CR (1978) Color vision mechanisms in monkey striate cortex: dual-opponent cells with concentric receptive fields. Journal of Neurophysiology 41:572-588.

152.Michelson C, Pillow, J., & Seidemann, E. (2017) Majority of choice-related variability in perceptual decisions is present in early sensory cortex. bioRxiv.

153.Mitchell JF, Sundberg, K. A., & Reynolds, J. H. (2007) Differential attention-dependent response modulation across cell classes in macaque visual area V4. Neuron 55:131-141.

154.Moore CI, Carlen, M., Knoblich, U., & Cardin, J. A. (2010) Neocortical interneurons: from diversity, strength. Cell 142:184-188.

155.Moore IV BD, & Freeman, R. D. (2012) Development of orientation tuning in simple cells of primary visual cortex. Journal of neurophysiology 107:2506-2516.

156.Mooser F, Bosking, W. H., & Fitzpatrick, D. (2004) A morphological basis for orientation tuning in primary visual cortex. Nature neuroscience 7:872-879.

157.Mori F, Nakajima, K., Tachibana, A., & Mori, S. (2006) Obstacle clearance and prevention from falling in the bipedally walking Japanese monkey, Macaca fuscata. Age and ageing 35:ii19-ii23.

158.Moser E, Mathiesen, I., & Andersen, P. (1993) Association between brain temperature and dentate field potentials in exploring and swimming rats. Science 259:1324-1326.

159.Movshon JA, Thompson ID, Tolhurst DJ (1978a) Spatial summation in the receptive fields of simple cells in the cat's striate cortex. J Physiol 283:53-77.

160.Movshon JA, Thompson ID, Tolhurst DJ (1978b) Receptive field organization of complex cells in the cat's striate cortex. J Physiol 283:79-99.

161.Mullen KT, & Beaudot, W. H. (2002) Comparison of color and luminance vision on a global shape discrimination task. Vision Research 42:565-575.

162.Nathanson JL, Yanagawa Y, Obata K, Callaway EM (2009) Preferential labeling of inhibitory and excitatory cortical neurons by endogenous tropism of adeno-associated virus and lentivirus vectors. Neuroscience 161:441-450.

163.Newsome WT, Britten, K. H., & Movshon, J. A. (1989) Neuronal correlates of a perceptual decision. Nature 341:52-54.

164.Ni AM, & Maunsell, J. H. (2010) Microstimulation reveals limits in detecting different signals from a local cortical region. Current Biology 20:824-828.

165.Nienborg H, Cumming BG (2006) Macaque V2 neurons, but not V1 neurons, show choice-related activity. J Neurosci 26:9567-9578.

166.Nienborg H, Cumming BG (2009) Decision-related activity in sensory neurons reflects more than a neuron's causal effect. Nature 459:89-92.

167.Nienborg H, Cumming BG (2014) Decision-related activity in sensory neurons may depend on the columnar architecture of cerebral cortex. J Neurosci 34:3579-3585.

168.Ohayon S, Grimaldi P, Schweers N, Tsao DY (2013) Saccade modulation by optical and electrical stimulation in the macaque frontal eye field. J Neurosci 33:16684-16697.

169.Olmos A, & Kingdom, F. A. (2004) A biologically inspired algorithm for the recovery of shading and reflectance images. Perception 33:1463-1473.

170.Onorato I, Neuenschwander, S., Hoy, J., Lima, B., Rocha, K. S., Broggini, A. C., ... & Fries, P. (2020) A distinct class of bursting neurons with strong gamma synchronization and stimulus selectivity in monkey V1. Neuron 105:180-197.

171.Packer AM, & Yuste, R. (2011) Dense, unspecific connectivity of neocortical parvalbumin-positive interneurons: a canonical microcircuit for inhibition?. Journal of Neuroscience 31:13260-13271.

172.Pajani A, Kok P, Kouider S, de Lange FP (2015) Spontaneous Activity Patterns in Primary Visual Cortex Predispose to Visual Hallucinations. J Neurosci 35:12947-12953.

173.Palmer C, Cheng SY, Seidemann E (2007) Linking neuronal and behavioral performance in a reaction-time visual detection task. J Neurosci 27:8122-8137.

174.Palmer C, Cheng, S. Y., & Seidemann, E. (2007) Linking neuronal and behavioral performance in a reaction-time visual detection task. Journal of Neuroscience 27:8122-8137.

175.Paolini AG, & McKenzie, J. S. (1997) Effects of inactivation of the magnocellular preoptic nucleus of olfactory bulb processing. Neuroreport 8:929-935.

176.Parker AJ, Newsome WT (1998) Sense and the single neuron: probing the physiology of perception. Annu Rev Neurosci 21:227-277.

177.Pillow JW, & Simoncelli, E. P. (2006) Dimensionality reduction in neural models: an information-theoretic generalization of spike-triggered average and covariance analysis. Journal of vision 6.

178.Poggio GF, Baker, F. H., Mansfield, R. J. W., Sillito, A., & Grigg, P. (1975) Spatial and chromatic properties of neurons subserving foveal and parafoveal vision in rhesus monkey. Brain research 100:25-59.

179. Poort J, Raudies, F., Wannig, A., Lamme, V. A., Neumann, H., & Roelfsema, P. R. (2012) The role of attention in figure-ground segregation in areas V1 and V4 of the visual cortex. Neuron 75:143-156.
180. Purushothaman G, & Bradley, D. C. (2005) Neural population code for fine perceptual decisions in area MT. Nature neuroscience 8:99-106.
181. Radoeva PD, Prasad, S., Brainard, D. H., & Aguirre, G. K. (2008) Neural activity within area V1 reflects unconscious visual performance in a case of blindsight. Journal of cognitive neuroscience 20:1927-1939.
182. Rees G, Wojciulik, E., Clarke, K., Husain, M., Frith, C., & Driver, J. (2000) Unconscious activation of visual cortex in the damaged right hemisphere of a parietal patient with extinction. Brain 123:1624-1633.
183. Reid RC, Alonso JM (1995) Specificity of monosynaptic connections from thalamus to visual cortex. Nature 378:281-284.
184. Reid RC, & Shapley, R. M. (1992) Spatial structure of cone inputs to receptive fields in primate lateral geniculate nucleus. Nature 356:716-718.
185. Reinagel P, Godwin, D., Sherman, S. M., & Koch, C. (1999) Encoding of visual information by LGN bursts. Journal of neurophysiology 81:2558-2569.
186. Rentzeperis I, Nikolaev, A. R., Kiper, D. C., & van Leeuwen, C. (2014) Distributed processing of color and form in the visual cortex. Frontiers in psychology 5.
187. Ress D, Heeger DJ (2003) Neuronal correlates of perception in early visual cortex. Nat Neurosci 6:414-420.
188. Rhoades CE, Shah, N. P., Manookin, M. B., Brackbill, N., Kling, A., Goetz, G., ... & Chichilnisky, E. J. (2019) Unusual physiological properties of smooth monostratified ganglion cell types in primate retina. Neuron 103:658-672.
189. Ringach DL (2002a) Spatial structure and symmetry of simple-cell receptive fields in macaque primary visual cortex. Journal of neurophysiology 88:455-463.
190. Ringach DL, Shapley, R. M., & Hawken, M. J. (2002b) Orientation selectivity in macaque V1: diversity and laminar dependence. Journal of Neuroscience 22:5639-5651.
191. Rodieck RW (1965) Quantitative analysis of cat retinal ganglion cell response to visual stimuli. Vision research 5:583-601.

192.Roelfsema PR, Lamme, V. A., & Spekreijse, H. (1998) Object-based attention in the primary visual cortex of the macaque monkey. Nature 395.

193.Roelfsema PR, Tolboom, M., & Khayat, P. S. (2007) Different processing phases for features, figures, and selective attention in the primary visual cortex. Neuron 56:785-792.

194.Rust NC, Schwartz O, Movshon JA, Simoncelli EP (2005) Spatiotemporal elements of macaque v1 receptive fields. Neuron 46:945-956.

195.Salzman CD, Britten KH, Newsome WT (1990) Cortical microstimulation influences perceptual judgements of motion direction. Nature 346:174-177.

196.Sawatari A, & Callaway, E. M. (2000) Diversity and cell type specificity of local excitatory connections to neurons in layer 3B of monkey primary visual cortex. Neuron 25:459-471.

197.Schmid MC, Mrowka SW, Turchi J, Saunders RC, Wilke M, Peters AJ, Ye FQ, Leopold DA (2010) Blindsight depends on the lateral geniculate nucleus. Nature 466:373-377.

198.Scholl B, Pattadkal, J. J., Dilly, G. A., Priebe, N. J., & Zemelman, B. V. (2015) Local integration accounts for weak selectivity of mouse neocortical parvalbumin interneurons. Neuron 87:424-436.

199.Schumer RA, & Movshon, J. A. (1984) Length summation in simple cells of cat striate cortex. Vision Research 24:565-571.

200.Seidemann E, Zohary, E., & Newsome, W. T. (1998) Temporal gating of neural signals during performance of a visual discrimination task. Nature 394.

201.Shadlen MN, Britten KH, Newsome WT, Movshon JA (1996) A computational analysis of the relationship between neuronal and behavioral responses to visual motion. J Neurosci 16:1486-1510.

202.Shapley R (2009) Linear and nonlinear systems analysis of the visual system: Why does it seem so linear?: A review dedicated to the memory of Henk Spekreijse. Vision research 49:907-921.

203.Shapley R, & Hawken, M. J. (2011) Color in the cortex: single-and double-opponent cells. Vision research 51:701-717.

204.Shushruth S, Mazurek, M., & Shadlen, M. N. (2018) Comparison of decision-related signals in sensory and motor preparatory responses of neurons in Area LIP. Journal of Neuroscience 38:6350-6365.

205.Simonyan K (2014) The laryngeal motor cortex: its organization and connectivity. Current opinion in neurobiology 28:15-21.

206.Sincich LC, Park KF, Wohlgemuth MJ, Horton JC (2004) Bypassing V1: a direct geniculate input to area MT. Nat Neurosci 7:1123-1128.

207.Sohal VS, Zhang F, Yizhar O, Deisseroth K (2009) Parvalbumin neurons and gamma rhythms enhance cortical circuit performance. Nature 459:698-702.

208.Sokolova IV, & Mody, I. (2008) Silencing-induced metaplasticity in hippocampal cultured neurons. Journal of neurophysiology 100:690-697.

209.Solomon SG, Peirce JW, Lennie P (2004) The impact of suppressive surrounds on chromatic properties of cortical neurons. J Neurosci 24:148-160.

210.Stanislaw H, & Todorov, N. (1999) Calculation of signal detection theory measures. Behavior research methods, instruments, & computers 31:137-149.

211.Stauffer WR, Lak, A., Yang, A., Borel, M., Paulsen, O., Boyden, E. S., & Schultz, W. (2016) Dopamine neuron-specific optogenetic stimulation in rhesus macaques. Cell 166:1564-1571.

212.Stemmler M, & Koch, C. (1999) How voltage-dependent conductances can adapt to maximize the information encoded by neuronal firing rate. Nature Neuroscience 2.

213.Tailby C, Solomon SG, Lennie P (2008) Functional asymmetries in visual pathways carrying S-cone signals in macaque. J Neurosci 28:4078-4087.

214.Tamura K, Takeda, M., Setsuie, R., Tsubota, T., Hirabayashi, T., Miyamoto, K., & Miyashita, Y. (2017) Conversion of object identity to object-general semantic value in the primate temporal cortex. Science 357:687-692.

215.Tappen MF, Freeman, W. T., & Adelson, E. H. (2003) Recovering intrinsic images from a single image. In Advances in neural information processing systems:1367-1374.

216.Tehovnik EJ, Slocum WM, Schiller PH (2003) Saccadic eye movements evoked by microstimulation of striate cortex. Eur J Neurosci 17:870-878.

217.Tehovnik EJ, Slocum WM, Schiller PH (2004) Microstimulation of V1 delays the execution of visually guided saccades. Eur J Neurosci 20:264-272.

218.Thomsen S (1991) Pathologic analysis of photothermal and photomechanical effects of laser–tissue interactions. Photochemistry and photobiology 53:825-835.

219.Thorell LG, De Valois RL, Albrecht DG (1984) Spatial mapping of monkey V1 cells with pure color and luminance stimuli. Vision Res 24:751-769.

220.Tolhurst DJ, Movshon JA, Dean AF (1983) The statistical reliability of signals in single neurons in cat and monkey visual cortex. Vision Res 23:775-785.

221.Tolhurst DJ, & Dean, A. F. (1990) The effects of contrast on the linearity of spatial summation of simple cells in the cat's striate cortex. Experimental Brain Research 79:582-588.

222.Touryan J, Lau, B., & Dan, Y. (2002) Isolation of relevant visual features from random stimuli for cortical complex cells. Journal of Neuroscience 22:10811-10818.

223.Turrigiano GG, Leslie, K. R., Desai, N. S., Rutherford, L. C., & Nelson, S. B. (1998) Activity-dependent scaling of quantal amplitude in neocortical neurons. Nature 391.

224.Uka T, & DeAngelis, G. C. (2004) Contribution of area MT to stereoscopic depth perception: choice-related response modulations reflect task strategy. Neuron 42:297-310.

225.V. E. Scerra MA, J. DIimidschstein, G. J. Fishell, J. H. Reynolds (2019) Optogenetic activation of GABAergic neurons in primate V1 impairs detection performance through indirect effects on excitatory neurons. Program No 30710 2019 Neuroscience Meeting Planner Chicago, IL: Society for Neuroscience, 2019 Online.

226.Van Brederode JFM, Mulligan, K. A., & Hendrickson, A. E. (1990) Calcium-binding proteins as markers for subpopulations of GABAergic neurons in monkey striate cortex. Journal of Comparative Neurology 298:1-22.

227.van Vugt B, Dagnino B, Vartak D, Safaai H, Panzeri S, Dehaene S, Roelfsema PR (2018) The threshold for conscious report: Signal loss and response bias in visual and frontal cortex. Science 360:537-542.

228.Wachtler T, Sejnowski, T. J., & Albright, T. D. (2003) Representation of color stimuli in awake macaque primary visual cortex. Neuron 37:681-691.

229.Weller JP, & Horwitz, G. D. (2018) Measurements of neuronal color tuning: Procedures, pitfalls, and alternatives. Vision Research 151:53-60.

230.Wiegert JS, Mahn M, Prigge M, Printz Y, Yizhar O (2017) Silencing Neurons: Tools, Applications, and Experimental Constraints. Neuron 95:504-529.

231.Wilson DE, Smith GB, Jacob AL, Walker T, Dimidschstein J, Fishell G, Fitzpatrick D (2017) GABAergic Neurons in Ferret Visual Cortex Participate in Functionally Specific Networks. Neuron 93:1058-1065 e1054.

232.Wilson NR, Runyan, C. A., Wang, F. L., & Sur, M. (2012) Division and subtraction by distinct cortical inhibitory networks in vivo. Nature 488.

233.Woloszyn L, & Sheinberg, D. L. (2012) Effects of long-term visual experience on responses of distinct classes of single units in inferior temporal cortex. Neuron 74:193-205.

234.Wool LE, Packer, O. S., Zaidi, Q., & Dacey, D. M. (2019) Connectomic identification and three-dimensional color tuning of S-OFF midget ganglion cells in the primate retina. Journal of Neuroscience 39:7893-7909.

235.Wurtz RH (2015) Using perturbations to identify the brain circuits underlying active vision. Philosophical Transactions of the Royal Society B: Biological Sciences 370.

236.Yabuta NH, Sawatari, A., & Callaway, E. M. (2001) Two functional channels from primary visual cortex to dorsal visual cortical areas. Science 292:297-300.

237.Yarch J, Federer, F., & Angelucci, A. (2017) Local circuits of V1 layer 4B neurons projecting to V2 thick stripes define distinct cell classes and avoid cytochrome oxidase blobs. Journal of Neuroscience 37:422-436.

238.Yartsev MM, Hanks, T. D., Yoon, A. M., & Brody, C. D. (2018) Causal contribution and dynamical encoding in the striatum during evidence accumulation. eLife 7.

239.Zaidi Q, & Li, A. (2006) Three-dimensional shape perception from chromatic orientation flows. Visual Neuroscience 23:323-330.

240.Zhang L, Yan, Q., Liu, Z., Zou, H., & Xiao, C. (2017) Illumination decomposition for photograph with multiple light sources. IEEE Transactions on Image Processing 26:4114-4127.